



## 저작자표시-비영리 2.0 대한민국

이용자는 아래의 조건을 따르는 경우에 한하여 자유롭게

- 이 저작물을 복제, 배포, 전송, 전시, 공연 및 방송할 수 있습니다.
- 이차적 저작물을 작성할 수 있습니다.

다음과 같은 조건을 따라야 합니다:



저작자표시. 귀하는 원저작자를 표시하여야 합니다.



비영리. 귀하는 이 저작물을 영리 목적으로 이용할 수 없습니다.

- 귀하는, 이 저작물의 재이용이나 배포의 경우, 이 저작물에 적용된 이용허락조건을 명확하게 나타내어야 합니다.
- 저작권자로부터 별도의 허가를 받으면 이러한 조건들은 적용되지 않습니다.

저작권법에 따른 이용자의 권리는 위의 내용에 의하여 영향을 받지 않습니다.

이것은 [이용허락규약\(Legal Code\)](#)을 이해하기 쉽게 요약한 것입니다.

[Disclaimer](#)

**Ph.D. Dissertation of Engineering**

**Symmetry Engineering of  
Two-Dimensional Materials by  
van der Waals Epitaxially Grown  $\text{MoO}_3$**

**반데르발스 에피성장한  $\text{MoO}_3$ 를 통한  
2차원물질의 대칭성 엔지니어링**

**August 2023**

**Graduate School of Engineering  
Seoul National University  
Department of Materials Science and Engineering**

**Hangyel Kim**

# **Symmetry Engineering of Two-Dimensional Materials by van der Waals Epitaxially Grown MoO<sub>3</sub>**

**Prof. Gwan-Hyoung Lee**

**Submitting a Ph.D. Dissertation of  
Engineering**

**August 2023**

**Graduate School of Engineering  
Seoul National University  
Department of Materials Science and Engineering**

**Hangyel Kim**

**Confirming the Ph.D. Dissertation written by  
Hangyel Kim  
August 2023**

Chair	Hyejin Jang	(Seal)
-------	-------------	--------

Vice Chair	Gwan-Hyoung Lee	(Seal)
------------	-----------------	--------

Examiner	Jihyun Kim	(Seal)
----------	------------	--------

Examiner	Chul-Ho Lee	(Seal)
----------	-------------	--------

Examiner	Jangyup Son	(Seal)
----------	-------------	--------

# Abstract

Moiré superlattices composed of in-plane anisotropic two-dimensional (2D) materials are expected to exhibit novel physical properties which cannot be achieved in conventional moiré superlattices. However, the experimental investigation of moiré superlattice with in-plane anisotropic 2D materials has been limited due to the instability of these materials. Therefore, it is crucial to fabricate ultrathin, high-quality, and air-stable in-plane anisotropic 2D materials to enable the realization of moiré superlattice based on in-plane anisotropic 2D materials.

In this dissertation, orthorhombic molybdenum trioxide ( $\alpha$ -MoO<sub>3</sub>) is focused and utilized as an air-stable in-plane anisotropic building block for the moiré superlattice. The research has been divided and specified into three stages to achieve the moiré superlattice based on  $\alpha$ -MoO<sub>3</sub>.

In the first stage, a method is developed to epitaxially grow  $\alpha$ -MoO<sub>3</sub> nanosheets on various 2D materials. Mono- to multilayer  $\alpha$ -MoO<sub>3</sub> nanosheets are successfully synthesized by evaporating amorphous molybdenum oxide thin films in ambient conditions. Despite significant lattice and symmetry mismatches, single crystalline  $\alpha$ -MoO<sub>3</sub> nanosheets are synthesized without grain boundaries. Additionally, the electrical properties of  $\alpha$ -MoO<sub>3</sub> such as band gap, work function, and carrier type are investigated.

The second part systemically reveals the electrical and tribological properties of the epitaxially grown  $\alpha$ -MoO<sub>3</sub> nanosheets on graphite template. Using atomic force microscopy, the properties of  $\alpha$ -MoO<sub>3</sub> are investigated including friction, adhesive force, work function, tunnel current, and dielectric constant. The study demonstrates that the friction of atomically smooth  $\alpha$ -MoO<sub>3</sub> saturates rapidly within a few layers due to weak mechanical interlayer interaction. The work function and dielectric constant of  $\alpha$ -MoO<sub>3</sub> nanosheets also exhibit thickness-insensitivity attributed to weak interlayer coupling.

Lastly, vdW epitaxially grown  $\alpha$ -MoO<sub>3</sub> is employed as an in-plane anisotropic

building block. A heterostructure consisting of  $\alpha$ -MoO<sub>3</sub> and monolayer graphene is fabricated by forming a rectangular superlattice. It is revealed that deposition of  $\alpha$ -MoO<sub>3</sub> results in hole doping, compressive strain, and in-plane anisotropy to graphene. This research presents a novel method of symmetry engineering to induce in-plane anisotropy in symmetric 2D materials through the formation of asymmetric superlattices using epitaxially grown 2D layers.

**Keywords:** two-dimensional materials, in-plane anisotropy, graphene,  $\alpha$ -MoO<sub>3</sub>, van der Waals heterostructure, moiré superlattice

**Student Number:** 2019-27477

# Table of Contents

<b>Chapter 1.</b>	<b>Introduction.....</b>	<b>1</b>
	1.1. Study Background.....	1
	1.2. Purpose of Research.....	11
<b>Chapter 2.</b>	<b>van der Waals Epitaxial Growth of <math>\alpha</math>-MoO<sub>3</sub> on Two-Dimensional Growth Template.....</b>	<b>34</b>
	2.1. Introduction.....	34
	2.2. Methods .....	37
	2.3. Results and Discussions .....	38
	2.4. Conclusion .....	53
<b>Chapter 3.</b>	<b>Thickness-Insensitive Properties of <math>\alpha</math>-MoO<sub>3</sub> Nanosheets by Weak Interlayer Coupling .....</b>	<b>54</b>
	3.1. Introduction.....	54
	3.2. Methods .....	56
	3.3. Results and Discussions .....	58
	3.4. Conclusion .....	75
<b>Chapter 4.</b>	<b>In-plane Anisotropy of Graphene by Strong Interlayer Interactions with van der Waals Epitaxially Grown MoO<sub>3</sub>.....</b>	<b>76</b>
	4.1. Introduction.....	76
	4.2. Methods .....	78
	4.3. Results and Discussions .....	81
	4.4. Conclusion .....	94
<b>Chapter 5.</b>	<b>Conclusion .....</b>	<b>95</b>
<b>Bibliography</b>	<b>.....</b>	<b>97</b>
<b>Abstract in Korean</b>	<b>.....</b>	<b>114</b>

# Chapter 1. Introduction

## 1.1. Study Background

### 1.1.1 Two-dimensional materials

Two-dimensional (2D) materials are composed of layers in which atoms are connected through strong covalent or ionic bonds, and these layers are held with each other by relatively weak van der Waals (vdW) force. The vdW force between the layers can be easily overcome mechanically, and mono- to few-layered nanosheets can be isolated on various substrates [1]. Due to their dangling-bond-free surface and extremely limited dimensionality, 2D materials exhibit distinctive properties compared to their bulk counterparts [2]. This novelty has triggered extensive research interest in various types of 2D materials.

#### *1.1.1.1 In-plane isotropic 2D materials*

Among the various 2D materials, graphene is the most notable example, consisting of a single layer of carbon atoms arranged in a hexagonal structure (Fig. 1.1a) [3]. Graphene is derived from graphite and has unique properties that have garnered significant attention in research. Graphene has semi-metallic property due to the touching of the valence band (VB) and conduction band (CB) at  $K$  and  $K'$  valley in its electronic band structure (Fig. 1.1b) [4]. The energy bands around the valleys exhibit linear dispersion, which indicates massless Dirac fermions in graphene [4]. Due to this linear dispersive band structure, graphene shows remarkable carrier mobility exceeding  $10^5 \text{ cm}^2 \text{ V}^{-1} \text{ s}^{-1}$  at room temperature [5, 6]. Furthermore, its carrier concentration can be modulated by electrostatic doping [5, 6]. By applying

positive (negative) gate bias, electrons (holes) are populated in CB (VB) by shift of Fermi level above (below) the Dirac cone (Fig. 1.1c) [5-7].

There are also other kinds of 2D materials which have similar structure with graphene. In hexagonal boron nitride (hBN), boron and nitrogen atoms alternatively occupy sublattice of hexagonal configuration forming covalent  $sp^2$  bonds (Fig. 1.2a) [8]. The lattice constant of hBN is nearly identical to that of graphene. hBN is widely used as an ultrathin 2D dielectric layer because of its wide band gap ( $\sim 6$  eV) [9, 10], dielectric constant comparable with  $SiO_2$  ( $\sim 3.7$ ) [11], thermal stability [12], and dangling-bond-free surface (Fig. 1.2b). When used as a substrate, hBN maintains the original band structure of graphene near the Dirac point resulting in enhancement of the mobility of graphene-based devices [2].

In group VI transition metal dichalcogenides with 2H phase (2H-TMDCs, e.g.,  $MoS_2$ ,  $MoSe_2$ ,  $WS_2$ ,  $WSe_2$ ), the metal atom is sandwiched by the two chalcogen atoms with trigonal prismatic arrangement (Fig. 1.3a) [13, 14]. 2H-TMDCs offer a broad range of band gap options that span the visible and infrared regions depending on the metal and chalcogen atoms [14]. In their monolayer form, most 2H-TMDCs exhibit a direct band gap, while their bulk counterparts typically have an indirect band gap (Fig. 1.3b) [14]. For instance, monolayer 2H-TMDCs such as  $MoS_2$  (1.8 eV),  $MoSe_2$  (1.5 eV),  $WS_2$  (2.1 eV), and  $WSe_2$  (1.7 eV) possess a direct band gap, whereas the bulk phases exhibit an indirect gap with lower energy values [14]. 2H-TMDCs can exhibit high mobility due to the absence of dangling bonds when suitable substrate and metal contacts are considered. For instance,  $MoS_2$  field-effect transistor with scandium contacts demonstrates a mobility of  $700\text{ cm}^2\text{ V}^{-1}\text{ s}^{-1}$  at room temperature [15].

These three types of 2D materials belong to hexagonal crystal system and exhibit almost identical in-plane properties due to their highly symmetric structure. These 2D materials are referred to as in-plane isotropic 2D materials.



### *1.1.1.2 In-plane anisotropic 2D materials*

In contrast to the 2D materials with in-plane isotropy, there are also other type of 2D materials that exhibit anisotropy along their in-plane directions. These materials are referred to as in-plane anisotropic 2D materials. Most of in-plane anisotropic 2D materials belong to low symmetric crystal systems, such as orthorhombic, monoclinic, and triclinic crystal systems. Due to the differences in lattice constants and bonding configurations, these materials exhibit different physical properties depending on their in-plane orientations.

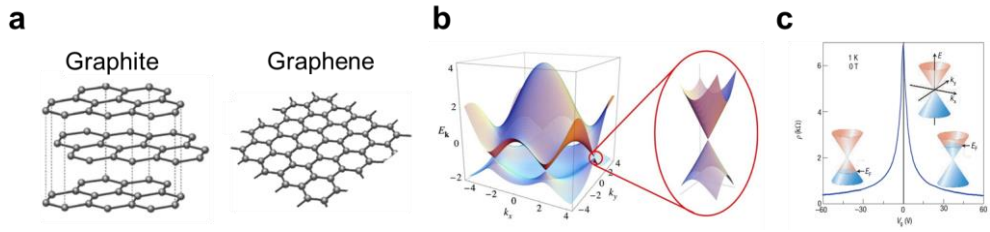
Black phosphorus (BP), also known as phosphorene, is the most extensively studied 2D material with in-plane anisotropy. Figure 1.4a illustrates the crystal structure of BP, which belongs to the  $Cmca$  space group and has an orthorhombic crystal structure [16]. BP exhibits a puckered arrangement of two subatomic layers, a consequence of the repulsion between the lone pair electrons in phosphorus atoms. The difference in lattice constants and bonding configurations along the armchair and zigzag directions leads to in-plane anisotropic mechanical, electrical, and optical properties (Fig. 1.4b) [16].

The crystal structures of group IV monochalcogenides (MXs, where  $M = \text{Ge}$  or  $\text{Sn}$  and  $X = \text{S}$  or  $\text{Se}$ ) share similarities with that of BP. However, unlike BP, which consists of a single-element composition, MXs are binary systems composed of two elements with different electronegativities. Additionally, while BP has two atomic sublayers, MXs have four sublayers in their atomic layers (Figs. 1.5a-b) [17]. As a result, MXs exhibit lower symmetry ( $Pnma$  space group) compared to BP. Notably, the monolayers of MXs exhibit an in-plane polarization and broken inversion symmetry, resulting in the emergence of piezoelectricity and ferroelectricity (Fig. 1.5c) [17-20].

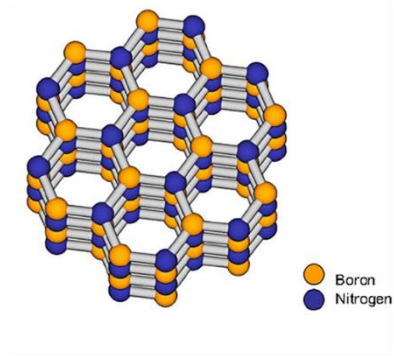
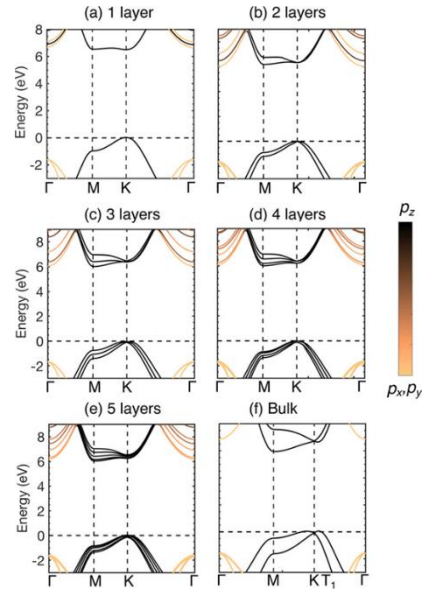
The monolayers of  $T_d$  phase group VI TMDCs exhibit dimerization of metal atoms by Peierls distortion (Fig. 1.6), leading to inversion of the VB and CB [21]. Furthermore, the inverted bands undergo additional hybridization through spin-orbit

coupling, resulting in  $T_d$  phase TMDCs to exhibit topologically nontrivial phases [21].

Rhenium dichalcogenides ( $\text{ReX}_2$ ) belong to triclinic crystal system and only have inversion symmetry. Rhenium, which belongs to group VII in periodic table, has one additional valence electron compared to group VI transition metals. The excess electron results in clustering of four Re atoms into rhombus shape (Fig. 1.7a), and the  $\text{Re}_4$  rhombuses are connected with Re-Re bridges.  $\text{ReX}_2$  has six-degenerated domains which can be distinguished by direction and patterns of  $\text{Re}_4$  rhombuses [22-25]. Since the domains can be transformed with each other by uniaxial strain [24], propagation of fracture [26], or e-beam irradiation [27],  $\text{ReX}_2$  exhibits ferroelasticity (Fig. 1.7b) [24].



**Figure 1.1.** (a) Crystal structure of graphite and graphene. Adapted from the reference [3] with permission. (b) Electronic band structure of monolayer graphene. Adapted from the reference [4] with permission. (c) Gate-dependent resistivity of monolayer graphene. Adapted from the reference [28] with permission.

**a****b**

**Figure 1.2.** (a) Crystal structure of hBN. Adapted from the reference [8] with permission. (b) Electronic band structure of hBN from monolayer to bulk. Adapted from the reference [9] with permission.

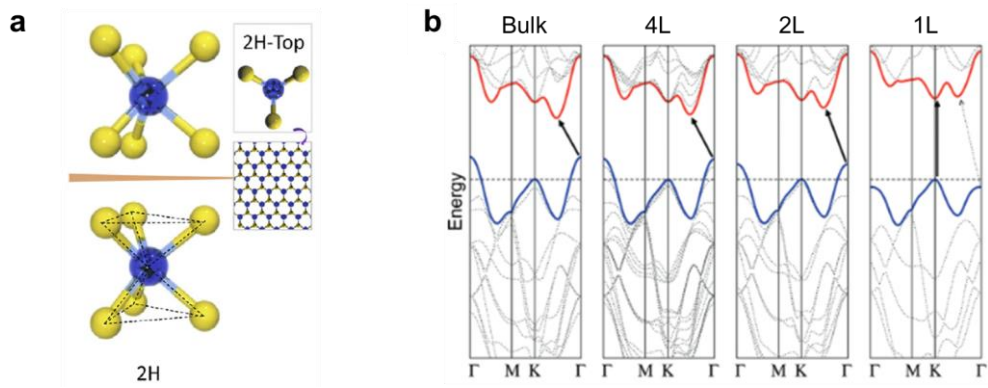


**Figure 1.3.** (a) Atomic arrangement of 2H-TMDCs. Adapted from the reference [14] with permission. (b) Electronic band stricture of MoS<sub>2</sub> from bulk to monolayer. Adapted from the reference [13] with permission.

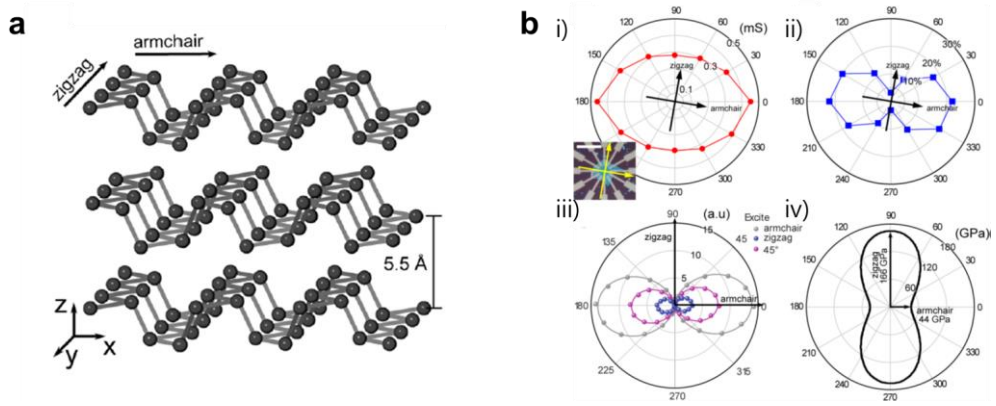


**Figure 1.4.** (a) Crystal structure of black phosphorous. (b) In-plane anisotropic i) conductance, ii) optical extinction, iii) photoluminescence, and iv) Young's modulus of black phosphorous. Adapted from the reference [16] with permission.

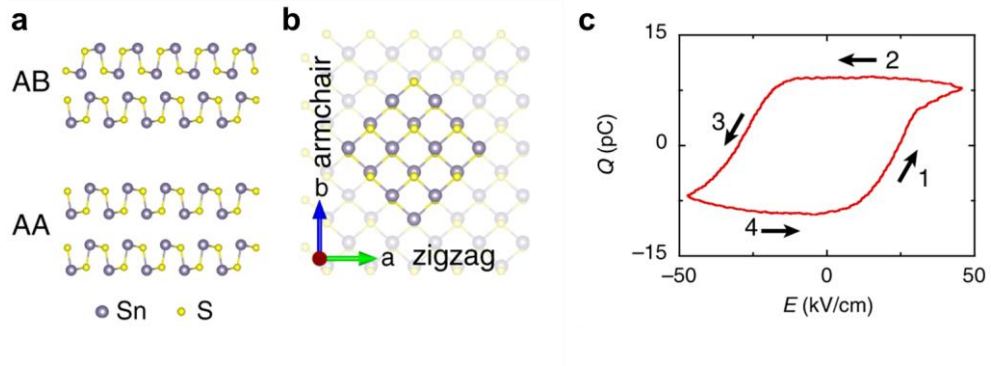


**Figure 1.5.** (a) Cross-sectional crystal structures of SnS with different stacking orders. (b) Top view of crystal structure of monolayer SnS (b) Ferroelectric resistive switching for Ag/SnS device. (a-c) are adapted from the reference [17] with permission.

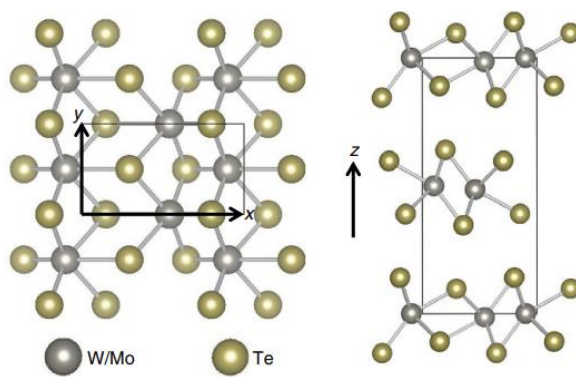


**Figure 1.6.** Crystal structure of group VI TMDCs with  $T_d$  phase. Adapted from the reference [21] with permission.



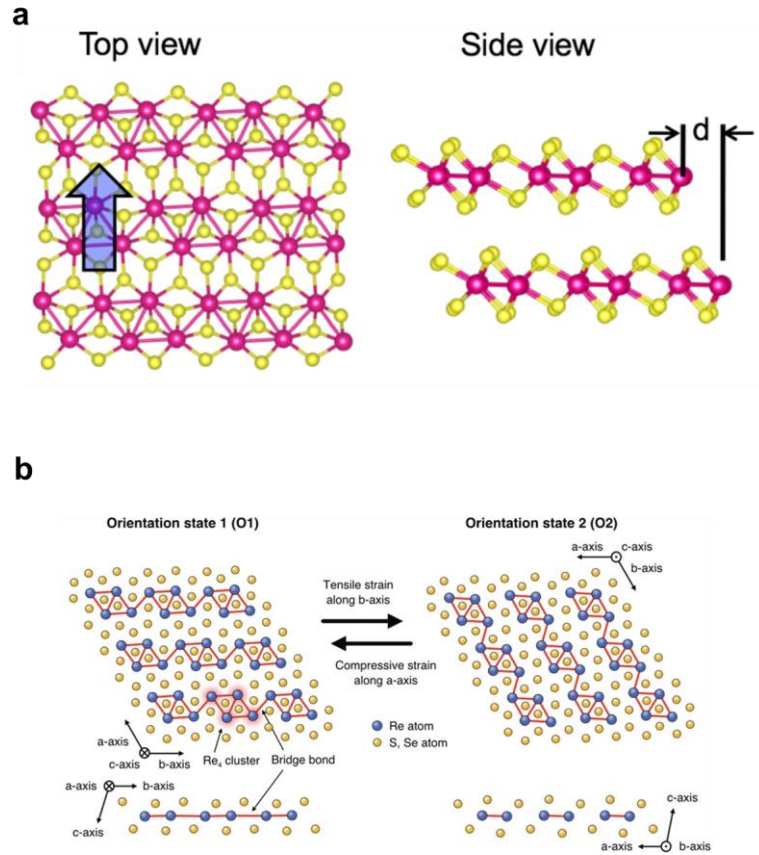


**Figure 1.7.** (a) Crystal structures of ReS<sub>2</sub>. Adapted from the reference [22] with permission.  
 (b) Ferroelastic switching between two ReS<sub>2</sub> domains. Adapted from the reference [24] with permission.

## **1.1.2 van der Waals heterostructures and moiré superlattices**

### *1.1.2.1 van der Waals heterostructures*

As opposed to exfoliation, it is also available to stack more than two layers of 2D materials by vdW force (Fig. 1.8) [2]. These structures are called vdW heterostructures (vdWHs) [2], and they exhibit distinctive characteristics compared to conventional heterostructures. In vdWHs, individual 2D materials are bound together by relatively weak vdW forces, and they have atomically sharp interfaces without gradient of atomic composition. Due to these interfacial characteristics, the vdWHs offer a substantially larger range of diversity compared to the conventional methods in which the combinations are restricted by lattice mismatch [2]. Consequently, by harnessing the advantages offered by 2D materials, vdWHs present new opportunities for the development of novel optoelectronic devices [29, 30].

### *1.1.2.2 Moiré superlattices with in-plane isotropic 2D materials*

The properties of vdWHs are not only determined by the types of 2D materials being stacked, but also affected by the stacking angle and lattice constant difference between them. The spatial overlap of atoms in the two layers can lead to the formation of long-range periodicities known as moiré superlattices (Fig. 1.9a) [31-33]. These superlattices give rise to unique phenomena which are not observed in the individual constituent materials.

When two monolayer graphene sheets are stacked with a small twist angle, a moiré superlattice is formed in the real space, resulting in a mini-Brillouin zone in reciprocal space (Fig. 1.9b) [32, 34]. The Dirac cones in adjacent minizone are hybridized by interlayer hopping, affecting the Fermi velocity at the Dirac cones [32, 34]. At specific twist angles known as magic angles, where the Fermi energy at the Dirac points becomes zero, a flattened band with a width of less than 10 meV is

formed which is separated from other bands by single-particle gaps (Fig. 1.9c) [35]. In the flat band, the conductance of charge carriers is strongly suppressed due to the competition between Coulomb energy and quantum kinetic energy, resulting in Mott-like insulator behavior in the twisted bilayer graphene [34]. Furthermore, slight modulation of the charge carrier concentration from the Mott-like state can induce unusual superconductivity in the twisted bilayer [35].

In the context of 2H-TMDCs, moiré excitons refer to excitons that are trapped within the potential minimum of the moiré patterns [32]. The moiré potential minima are typically found at high-symmetry sites that preserve three-fold rotation symmetry [31, 32, 36]. This property allows moiré-trapped excitons to exhibit valley-contrasting properties, leading to strong circular polarization. This polarization feature distinguishes them from quantum emitters localized by random extrinsic potentials [31, 32, 36]. Moreover, due to their spatial confinement, moiré-trapped excitons can serve as a platform for applications such as single-photon sources and quantum photonics [31, 32, 36].

In addition to above examples, there are peculiar moiré-related properties in diverse combinations of 2D materials, such as orbital magnetism and mid-infrared photoresponse in twisted bilayer graphene [37, 38], Hofstadter butterfly in graphene/hBN [39], and out-of-plane ferroelectricity in twisted bilayer hBN [40]. Until now, the experimental research about moiré superlattices is limited in stacking two hexagonal 2D materials.

The patterns of moiré superlattices can be calculated by mathematically as functions of lattice mismatch and twist angle between the consisting layers [41, 42]. Considering two individual monolayers denoted as “*layer 1*” and “*layer 2*”, the lattice parameters the layers can be represented as  $(\mathbf{R}_1, \mathbf{R}_2)\omega$  and  $(\mathbf{R}_1', \mathbf{R}_2')\omega'$ . Here  $\mathbf{R}_1$  ( $\mathbf{R}_1'$ ) and  $\mathbf{R}_2$  ( $\mathbf{R}_2'$ ) are the length of unit lattice vectors, and  $\omega$  ( $\omega'$ ) is angle between the lattice vectors for the *layer 1* (*layer 2*) [41, 42]. Next, the moiré patterns can be denoted as  $(p_1 \times p_2)\mathbf{R}(\alpha_1, \alpha_2)$ , where  $p_1$  are  $p_2$  are the scaling factors of the two unit lattice vectors of individual monolayers,  $\alpha_1$  are  $\alpha_2$  twist angles  $\mathbf{R}_1$  and  $\mathbf{R}_1'$  and  $\mathbf{R}_2$  and

$\mathbf{R}_2'$ , respectively [41, 42]. Therefore, the geometric parameters of the moiré patterns can be represented as follows:

$$\mathbf{R}_1^M = \kappa_1 \mathbf{R}_1 \dots \dots \dots \text{equation (1.1)}$$

$$\mathbf{R}_2^M = \kappa_2 \mathbf{R}_2 \dots \dots \dots \text{equation (1.2)}$$

$$\delta = \omega - (\gamma_1 - \alpha_1) = \omega - (\gamma_2 - \alpha_2) \dots \dots \text{equation (1.3)}$$

where  $\mathbf{R}_1^M$  and  $\mathbf{R}_2^M$  are periodicities of moiré vectors,  $\delta$  is angle between the moiré vectors, and  $\gamma_1$  ( $\gamma_2$ ) is angle between  $\mathbf{R}_1^M$  and  $\mathbf{R}_1$  ( $\mathbf{R}_2$ ), respectively (Fig. 1.10) [41]. By calculating atomic superposition between the two monolayers, the geometric parameters of the moiré patterns can be represented as:

$$\kappa_1 = \frac{p_1}{\Lambda} \sqrt{1 + p_2^2 - 2p_2 \cos \alpha_1} \dots \dots \dots \text{equation (1.4)}$$

$$\kappa_2 = \frac{p_2}{\Lambda} \sqrt{1 + p_1^2 - 2p_1 \cos \alpha_2} \dots \dots \dots \text{equation (1.5)}$$

$$\cos \gamma_1 = \frac{(\cos \alpha_1 - p_2)}{\sqrt{1 + p_2^2 - 2p_2 \cos \alpha_1}} \dots \dots \dots \text{equation (1.6)}$$

$$\cos \gamma_2 = \frac{(\cos \alpha_2 - p_1)}{\sqrt{1 + p_1^2 - 2p_1 \cos \alpha_2}} \dots \dots \dots \text{equation (1.7)}$$

$$\begin{aligned} \cos \delta \\ = \frac{\cos \omega' - p_1 \cos(\omega - \alpha_1) - p_2 \cos(\omega + \alpha_2) + p_1 p_2 \cos \omega}{\sqrt{1 + p_1^2 - 2p_1 \cos \alpha_2} \sqrt{1 + p_2^2 - 2p_2 \cos \alpha_1}} \dots \text{equation (1.8)} \end{aligned}$$

where,  $\Lambda = [\sin \omega' + p_1 p_2 \sin \omega - \sin \left( \frac{\omega + \omega'}{2} \right) \cos \left( \frac{\alpha + \alpha'}{2} \right) (p_1 + p_2) + \cos \left( \frac{\omega + \omega'}{2} \right) \sin \left( \frac{\alpha + \alpha'}{2} \right) (p_1 - p_2)] / \sin \omega$  [41].

For the two hexagonal monolayers, since the scaling factors, angles between the unit lattice vectors, and twist angles are all identical ( $p_1 = p_2$ ,  $\omega_1 = \omega_2 = 60^\circ$ , and  $\alpha_1 = \alpha_2$ ),  $\kappa$  and  $\gamma$  are also equal for both layers ( $\kappa = \kappa_1 = \kappa_2$  and  $\gamma = \gamma_1 = \gamma_2$ ). Therefore, the moiré vectors have the identical lengths ( $|\mathbf{R}_1^M| = |\mathbf{R}_2^M|$ ), and the equation (1.8) can be reduced into  $\cos \delta = 0.5$  ( $\delta = 60^\circ$ ). These results demonstrate that the moiré patterns between two hexagonal materials also exhibit hexagonal patterns. In this regard, it can be inferred that moiré-related properties in the system exhibit in-plane isotropic characteristics.

### 1.1.2.3 Moiré superlattices with in-plane anisotropic 2D materials

In contrast, moiré superlattices based on in-plane anisotropic 2D materials such as BP/BP and BP/graphene generally have parallelogram shaped moiré patterns. Due to the different periodicities of moiré vectors, theoretical studies have reported in-plane anisotropic moiré-related properties which cannot be observable in moiré superlattice with hexagonal 2D materials.

For example, moiré superlattice between twisted bilayer black phosphorus (tbBP) is represented in Fig. 1.11a [43]. There are four high-symmetry local stacking configurations in tbBP: AA, AB, AA', and AB' (Fig. 1.11b) [43]. The natural stacking order is AB, and the other configurations can be achieved by translating the upper layer along specific directions [43]. Interestingly, the CB and VB of tbBPs exhibit flat bands along the  $\Gamma$ -X (armchair) direction (Fig. 1.11c) [43]. The CB remains flat in all directions due to strong localization on AB' stacking, while the valence band is localized along the x direction on AA and AB stacking. These flat bands indicate a significantly high effective mass, leading to a sharp decrease in carrier mobility along the x-direction. The carrier mobility in the y-direction can also be affected by the twist angle, particularly at  $\theta = 2.7^\circ$ , where the conduction wave

function is highly localized even in the y-direction, resulting in a drastic reduction of electron mobility along the y-direction (Fig. 1.11d) [43].

Furthermore, moiré superlattices in twisted bilayer MX (tbMX) are expected to exhibit similar but more diverse properties [44, 45]. Due to the reduced symmetry of MXs compared to BP, the stacking configurations of tbMXs at  $\theta$  and  $180^\circ - \theta$  angles are not identical. Consequently, there are eight distinct types of high-symmetry local stacking configurations in tbMXs. However, both tbGeSe and tbSnS exhibit 1D flat band as well as charge carrier localization in 1D wires, similar to tbBP (Figs. 1.12a and b) [44]. The dispersion and charge modulation along a 1D wire can be explained by using the ionic Hubbard model [44]. The tbGeSe, depending on the twist angle and chemical potential, can exhibit diverse phases of matter, including band insulator (BI), Mott insulator (MI), bond-oriented wave (BOW), and Luttinger liquid (LL) (Fig. 1.12c) [44].

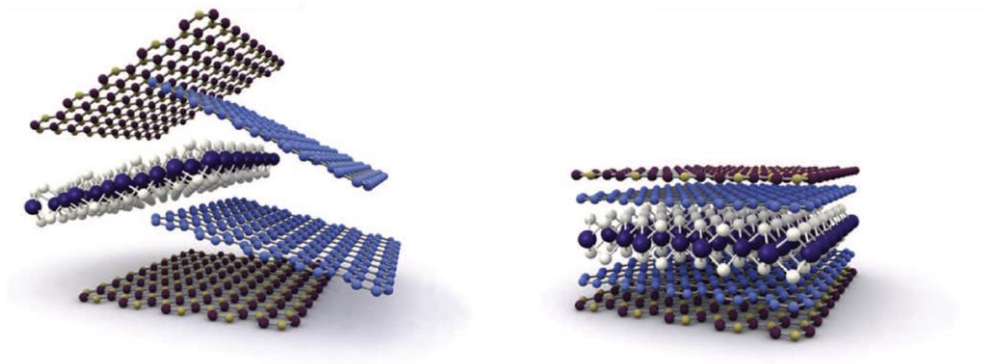


**Figure 1.8.** Schematic images of mechanically assembled van der Waals heterostructure. Adapted from the reference [2] with permission.

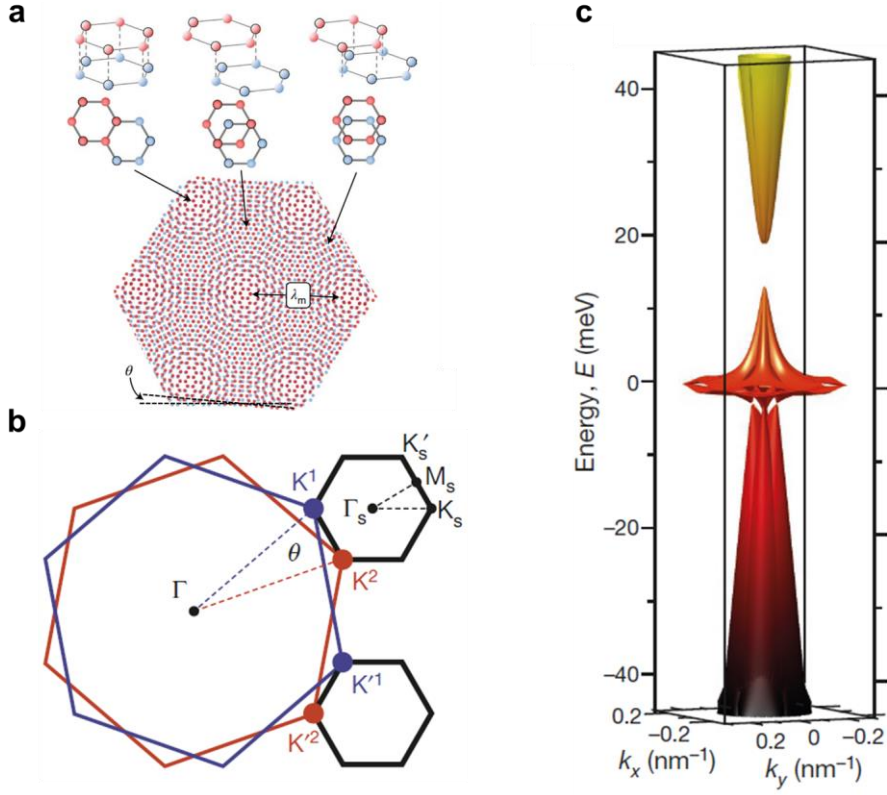


**Figure 1.9.** Moiré superlattice and its band structures. (a) Moiré superlattice and high symmetric points between twisted bilayer graphene. Adapted from the reference [33] with permission. (b) The constructed mini-Brillouin zone in twisted bilayer graphene. Adapted from the reference [34] with permission. (c) The band energy of twisted bilayer graphene at  $\theta = 1.05^\circ$  in the first mini-Brillouin zone of the superlattice. Adapted from the reference [35] with permission.



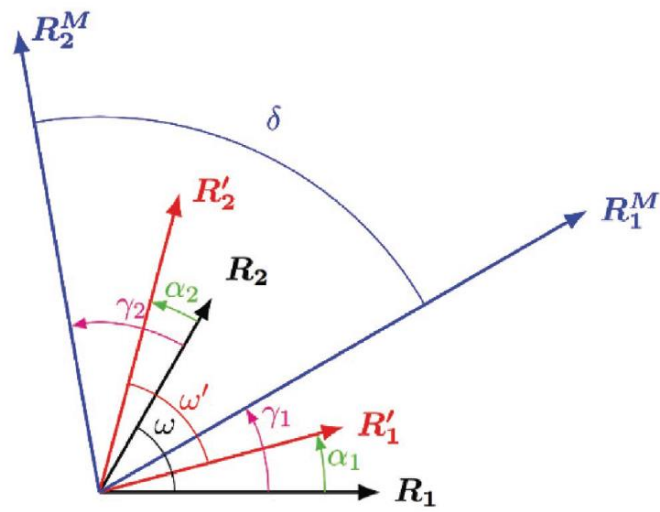


**Figure 1.10.** Lattice vectors of two individual monolayers and geometric parameters of moiré superlattice. Adapted from the reference [41] with permission.

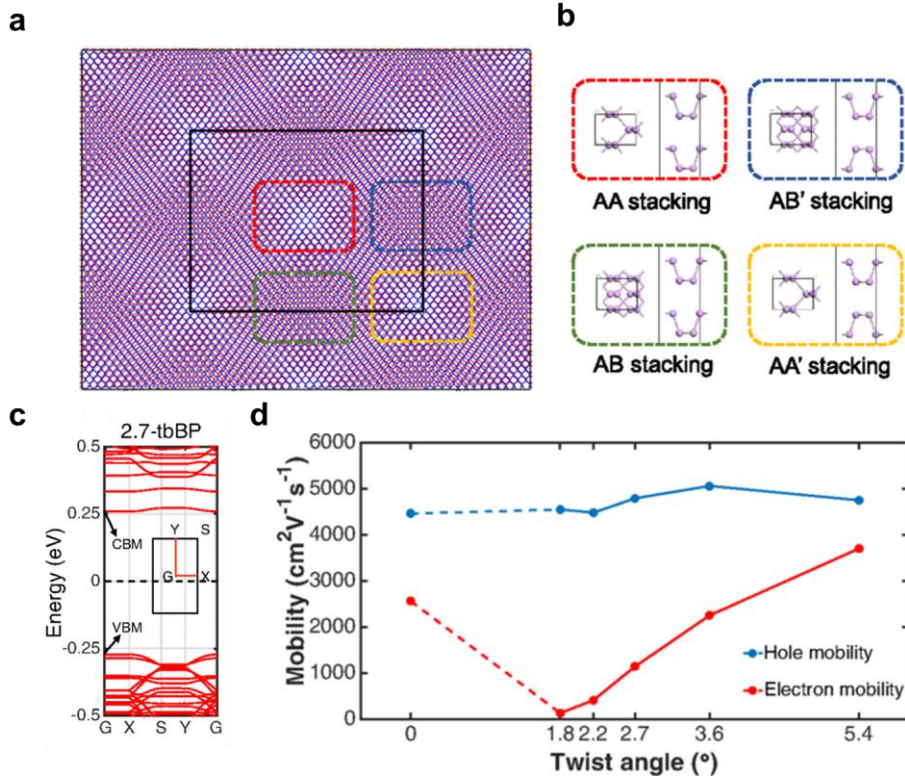


**Figure 1.11.** (a) Moiré superlattice formed by tbBP with 2.7° twist angle. (b) Four representative high-symmetry local configurations in tbBP. (c) Electronic band structure of 2.7°-tbBP. (d) Deformation limited carrier mobility along armchair direction of tbBP depending on the twist angle. (a-d) are adapted from the reference [43] with permission.

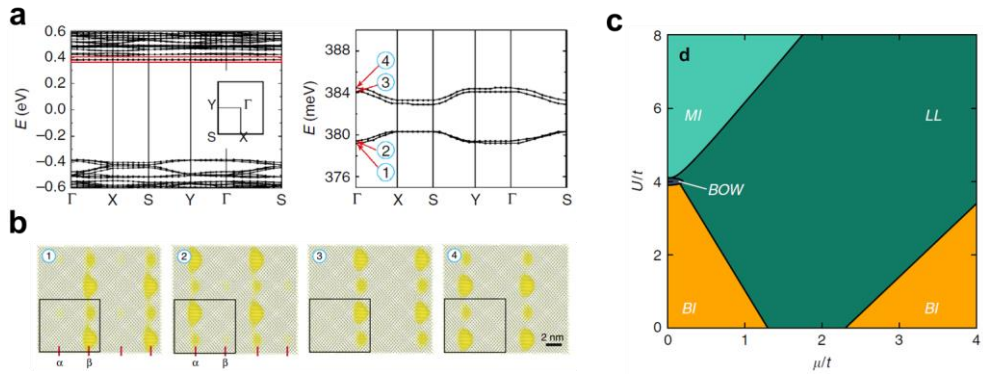


**Figure 1.12.** (a) Band structure of 6.61°-tbGeSe. (b) The real space charge density of the bands labeled by 1–4 in (a). (c) Phase diagram of many-body electron correlation in tbGeSe. (a-c) are adapted from the reference [44] with permission.

## 1.2. Purpose of Research

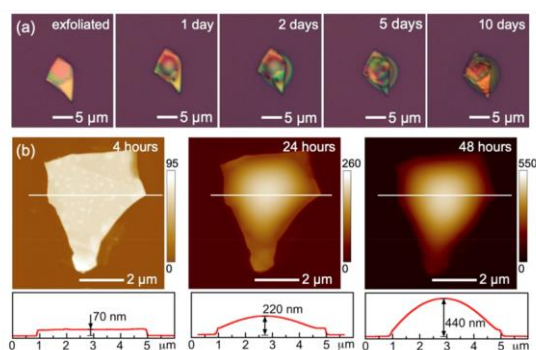
### 1.2.1 Requirement of air-stable in-plane anisotropic 2D materials as building blocks of moiré superlattice

Despite the intriguing moiré-related properties composed of in-plane anisotropic 2D materials, there have been few experimental studies on moiré superlattices with in-plane anisotropic 2D materials. The limited results can be attributed to the instability of in-plane anisotropic 2D materials under ambient conditions.

Compared to in-plane isotropic 2D materials, in-plane anisotropic 2D materials exhibit more diverse physical properties due to their higher degree of freedom. However, most of in-plane anisotropic 2D materials are unstable in the ambient conditions. BP and MXs have lone pair electrons at phosphorus and metal atoms, respectively, which act as Lewis bases [46-48]. They easily react with oxygen or water in the air, thus BP and MXs are degraded by forming oxide states (Fig. 1.13a) [46-48].  $T_d\text{-WTe}_2$  is also vulnerable to oxygen and water because the weak W-Te bonds due to small electronegativity difference between the atoms (Fig. 1.13b) [49].

Up until now, most techniques used to create moiré superlattices, such as exfoliation, selecting suitable flakes, and transferring them to other substrates, have been carried out in ambient environments. The in-plane anisotropic 2D materials are easily degraded during these procedures, which makes it challenging to achieve atomically sharp and ultra-clean interfaces. Therefore, it is necessary to explore air-stable in-plane anisotropic 2D materials to bridge the gap between the theoretical expectations and their experimental realization of moiré superlattices with in-plane anisotropic 2D materials.

**a**



**b**

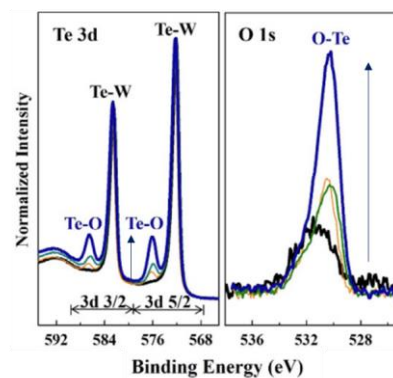


**Figure 1.13.** Air instability of in-plane anisotropic 2D materials. (a) Optical and atomic force microscope images demonstrating oxidation of GeS in ambient conditions. Adapted from the reference [47] with permission. (b) X-ray photoelectron spectroscopy results in degradation of  $T_d$ -WTe<sub>2</sub> in ambient conditions. Adapted from the reference [49] with permission.

## 1.2.2 $\alpha$ -MoO<sub>3</sub>: air-stable in-plane anisotropic 2D oxide

### 1.2.2.1 Crystal structure of $\alpha$ -MoO<sub>3</sub>

$\alpha$ -MoO<sub>3</sub> is one of air-stable in-plane anisotropic 2D materials. MoO<sub>3</sub> can exist in various phases, such as orthorhombic  $\alpha$  phase, monoclinic  $\beta$  phase, and hexagonal  $\gamma$  phase [50]. These phases are all composed of MoO<sub>6</sub> octahedra, but they show different structures depending on the sharing of oxygen atoms between the octahedra [50]. Among these phases,  $\alpha$ -MoO<sub>3</sub> is the most thermodynamically stable and possesses a layered structure. The layers of  $\alpha$ -MoO<sub>3</sub> consist of distorted MoO<sub>6</sub> double layers. Along the vertical [010] direction corresponding to the out-of-plane direction, the distorted MoO<sub>6</sub> octahedra are stacked through weak vdW forces, and the distance between two adjacent layers is approximately 0.7 nm [51, 52]. The crystal structure of  $\alpha$ -MoO<sub>3</sub> is shown in Fig. 1.14a [53], and experimental lattice constants are  $a=3.96$ ,  $b=13.86$ , and  $c=3.70$  Å [52].

In addition, the connectivity of the distorted MoO<sub>6</sub> octahedra is different along crystal orientations, and the properties of the Mo-O bond depend on the equilibrium bond distance. The crystal structures of  $\alpha$ -MoO<sub>3</sub> contain three types of oxygen atoms, each with a different coordination. These include apical ( $O_a$ ), edge-sharing ( $O_e$ ), and corner-sharing ( $O_c$ ) oxygen atoms (Fig. 1.14b) [53, 54]. In particular, the  $O_a$  atoms, oriented along the out-of-plane direction, are strongly double-bonded with the Mo atoms [50, 54]. This characteristic contributes to the stability of stoichiometric  $\alpha$ -MoO<sub>3</sub> in ambient conditions [55, 56], distinguishing it from other in-plane anisotropic 2D materials. Meanwhile,  $O_e$ -Mo- $O_e$ , and  $O_c$ -Mo- $O_c$  bonds are oriented along the two distinctive in-plane directions, respectively [50, 54].

In addition,  $O_a$  atoms at two adjacent layers are interdigitated with vdW gap of  $\sim 0.08$  nm [50, 53, 54]. The interatomic distance in  $\alpha$ -MoO<sub>3</sub> is extremely shorter than in other 2D materials, resulting in stronger interlayer interaction between the layers in comparison with other 2D materials. The elastic modulus values in the  $x$  ( $y$ )

direction for mono-, bi-, and trilayer  $\alpha$ -MoO<sub>3</sub> are 152.80 (95.64), 332.19 (205.09), and 516.1 (317.09) J m<sup>-2</sup>, respectively [54]. The relationship between thickness and elastic modulus shows a dependence larger than linear, indicating that the interlayer elastic coupling between the double layers increases with the thickness in the few-layer system [54].

### 1.2.2.2 Band structure of $\alpha$ -MoO<sub>3</sub>

Density functional theory (DFT) has revealed that  $\alpha$ -MoO<sub>3</sub> possesses a wide but indirect band gap of approximately 3 eV (Fig. 1.15) [53, 57, 58]. The density of states (DOS) of  $\alpha$ -MoO<sub>3</sub>, calculated using optB88-vdW, are shown in Figs. 1.16a [54]. It can be observed that the states at the VBM are primarily composed of O 2p states, while the CBM is dominated by Mo 4d states, with slight hybridization involving O 2p states [53, 54].

Additionally, site- and orbital-resolved DOS can be identified in Fig. 1.16b and Figs. 1.16c-f, respectively [54]. It has been demonstrated that the VBM is determined by the 2p states of the O<sub>c</sub> and O<sub>e</sub> oxygens. Especially, the VBM states of the O<sub>e</sub> and O<sub>c</sub> atoms are dominated by the  $p_y$  and  $p_x$  orbitals, respectively [53, 54]. On the other hand, the CBM is predominantly composed of the in-plane Mo- $d_{xy}$  orbital, with slight hybridization involving the  $p_x$  orbital of the O<sub>c</sub> atoms [53, 54]. These results indicate both VBM and CBM are governed by the in-plane atomic orbitals [53, 54].

### 1.2.2.3 High work function of $\alpha$ -MoO<sub>3</sub>

Bulk  $\alpha$ -MoO<sub>3</sub> has work function larger than 6 eV [50, 51, 59]. The extremely high work function of  $\alpha$ -MoO<sub>3</sub> make the material suitable for various applications such as a transparent anode and hole transport layer in light emitting diodes or solar cells.

The larger work function in  $\alpha$ -MoO<sub>3</sub> is influenced by its closed shell structure and additional dipole layers resulted from the apical O<sub>a</sub> [51]. The closed shell system of  $\alpha$ -MoO<sub>3</sub> results in the VBM being composed of O 2p states located deep below the vacuum level, approximately 9.8 eV [51]. In addition, due to the O<sub>a</sub> atoms, additional dipole layers are formed in  $\alpha$ -MoO<sub>3</sub> layer [51]. The dipole results in deeper potential inside of the  $\alpha$ -MoO<sub>3</sub> layer compared to other closed shell structures, such as TiO<sub>2</sub>, ZnO, or SnO<sub>2</sub> (Fig. 1.17) [51].



#### *1.2.2.4. In-plane anisotropy of $\alpha$ -MoO<sub>3</sub>*

As discussed above,  $\alpha$ -MoO<sub>3</sub> has three different lattice constants and bonding configurations along each crystallographic orientation. The differences lead to in-plane anisotropy in  $\alpha$ -MoO<sub>3</sub>.

As mentioned in Chapter 1.2.2.1, in-plane elastic modulus of  $\alpha$ -MoO<sub>3</sub> is orientation-dependent because of different bonding configurations [54]. Since bonding along a-axis is stronger than that along c-axis, the elastic modulus is also higher along a-axis [54].

In addition,  $\alpha$ -MoO<sub>3</sub> has in-plane anisotropic thermal expansion coefficient (TEC) [60]. As the temperature rises, lattice constant along the stacking direction of b-axis increases greatly. There is a slight expansion along the a-axis. It is also worth to note that TEC along c-axis has negative value for wide range of temperature (0 to 1000K) [60].

Furthermore,  $\alpha$ -MoO<sub>3</sub> exhibit in-plane anisotropic electrical and optical properties [61, 62]. These characteristics make  $\alpha$ -MoO<sub>3</sub> a promising 2D building block combined with its stability.

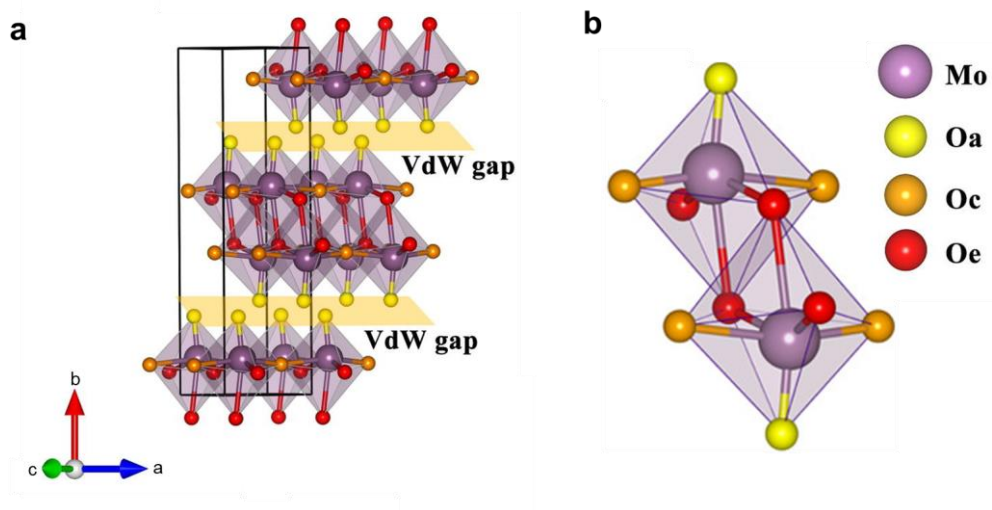


**Figure 1.14.** (a) Crystal structure of  $\alpha$ - $\text{MoO}_3$ . (b)  $\text{MoO}_6$  octahedra and three different oxygen atoms in  $\alpha$ - $\text{MoO}_3$ . (a) and (b) are adapted from the references [53] and [54] with permissions, respectively.

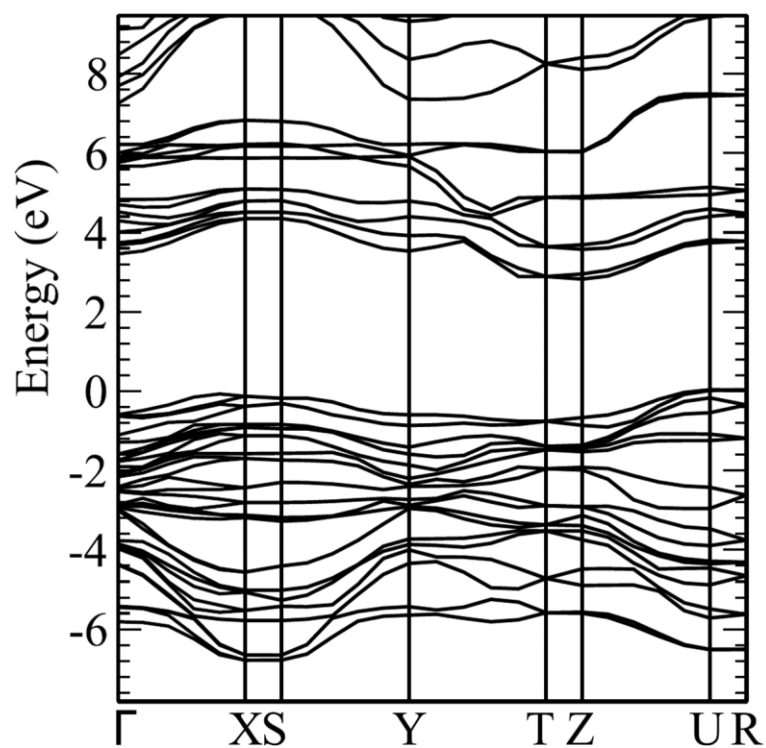


**Figure 1.15.** Electronic band structure of  $\alpha$ - $\text{MoO}_3$ . Adapted from the reference [51] with permission.

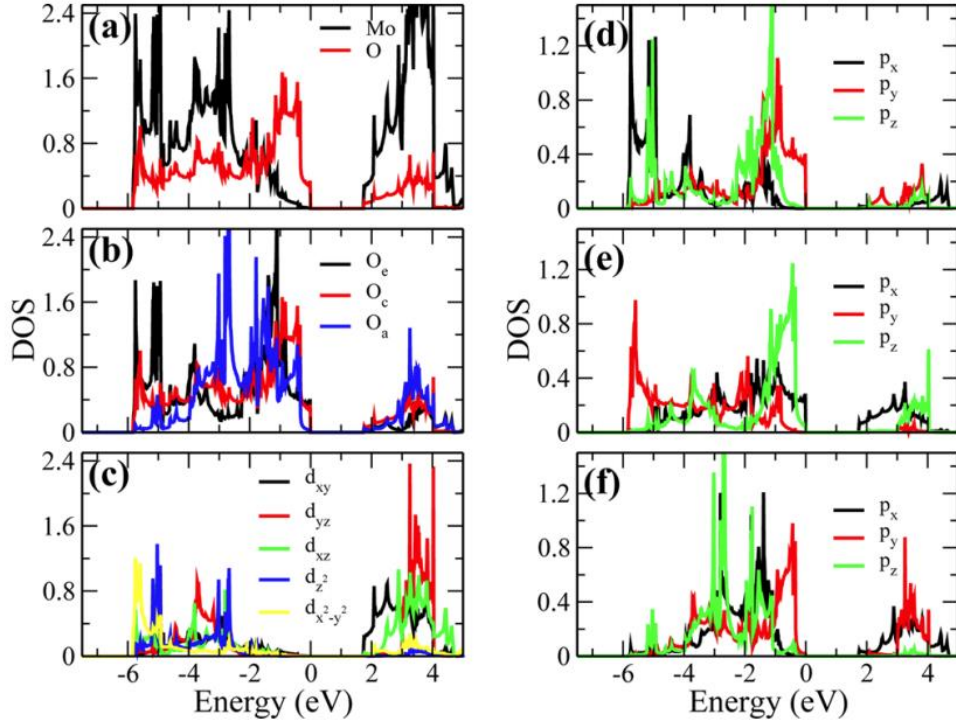


**Figure 1.16.** Density of states of  $\alpha$ -MoO<sub>3</sub>. (a) The partial DOS of Mo 4d and O 2p orbitals. (b). The site-resolved DOSs of three inequivalent oxygens. (c-f) The orbital-resolved DOSs of Mo, O<sub>e</sub>, O<sub>c</sub>, and O<sub>a</sub> atoms, respectively. (a-f) are adapted from the reference [54] with permission.

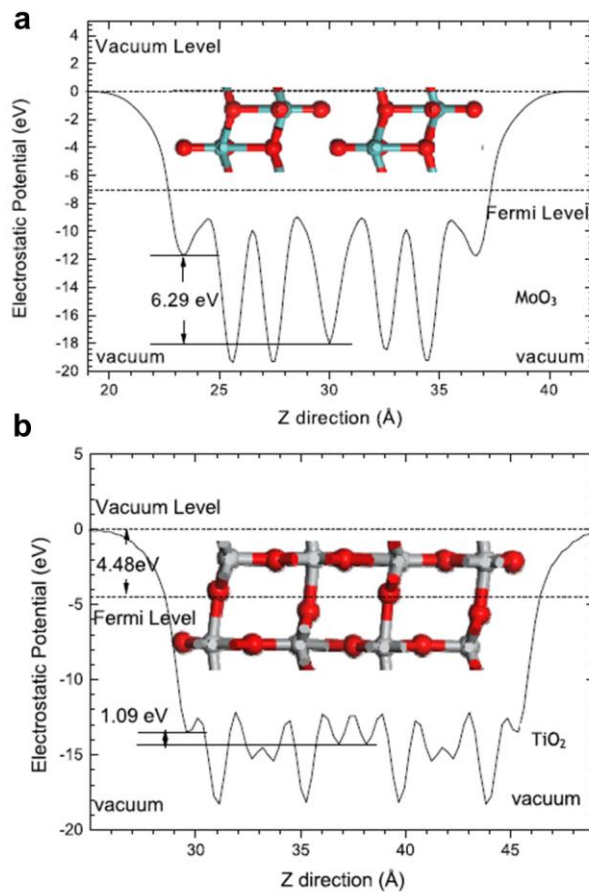


**Figure 1.17.** Electrostatic potential of (a)  $\alpha$ - $\text{MoO}_3$  slab and (b)  $\text{TiO}_2$  rutile slab with line average. (a) and (b) are adapted from the reference [51] with permission.

### 1.2.3 van der Waals epitaxial growth of $\alpha$ -MoO<sub>3</sub>

As discussed in Chapter 1.2.2,  $\alpha$ -MoO<sub>3</sub> is an air-stable building block for the moiré superlattices with in-plane anisotropic 2D materials. In addition, peculiar interlayer interaction with other 2D materials can be expected by its large work function and in-plane anisotropy. However,  $\alpha$ -MoO<sub>3</sub> has higher exfoliation energy compared with other conventional 2D materials, such as graphene or MoS<sub>2</sub> [53, 63]. This higher exfoliation energy can be attributed to the extremely short interatomic distance between O<sub>a</sub> atoms in adjacent layers, making it challenging to obtain high-quality and sufficiently large lateral size ultrathin  $\alpha$ -MoO<sub>3</sub> flakes. While  $\alpha$ -MoO<sub>3</sub> can be exfoliated like other 2D materials, the resulting flakes usually have thicknesses in the tens of nanometers [64]. Moreover, the synthesized  $\alpha$ -MoO<sub>3</sub> tends to have an island shape or limited lateral size in the hundreds of nanometers range. Since these morphologies are not appropriate to be used as a component of moiré superlattices, it is necessary to develop methods to enable fabrication of ultrathin  $\alpha$ -MoO<sub>3</sub> with high quality and  $\mu$ m-wide lateral size.

I suggest a vdW epitaxial growth of  $\alpha$ -MoO<sub>3</sub> on 2D templates to achieve mono- to few-layered high crystalline  $\alpha$ -MoO<sub>3</sub> with large lateral size. The dangling-bond-free and flat surface of the 2D materials enhances surface diffusion of precursors of  $\alpha$ -MoO<sub>3</sub>, leading to lateral growth of  $\alpha$ -MoO<sub>3</sub>.

In Chapter 2, a detailed method of vdW epitaxial growth of  $\alpha$ -MoO<sub>3</sub> is provided. By evaporating amorphous molybdenum oxide thin film under ambient conditions, mono- to multilayer  $\alpha$ -MoO<sub>3</sub> nanosheets were successfully synthesized on various 2D substrates. The crystallinity, band structure, and electrical properties of  $\alpha$ -MoO<sub>3</sub> are demonstrated.

In Chapter 3, comprehensive study using AFM microscopy was conducted on  $\alpha$ -MoO<sub>3</sub> nanosheets. Due to its unique crystal structure,  $\alpha$ -MoO<sub>3</sub> grown on graphite exhibits high friction and weak thickness-dependence.

In Chapter 4, interlayer interaction between  $\alpha$ -MoO<sub>3</sub> and monolayer graphene is demonstrated. Because of difference in TEC and Fermi level, the monolayer graphene is compressed and extremely p-doped. In addition, it is demonstrated that in-plane anisotropy is induced in the monolayer graphene by vdW epitaxially grown  $\alpha$ -MoO<sub>3</sub>.

In Chapter 5, the dissertation is summarized and concluded, and lists of future works will be given.

# Chapter 2. van der Waals Epitaxial Growth of $\alpha$ -MoO<sub>3</sub> on Two-Dimensional Growth Template<sup>1</sup>

## 2.1. Introduction

$\alpha$ -MoO<sub>3</sub> serves as an air-stable building block for moiré superlattices with in-plane anisotropic 2D materials [54, 55, 60]. Its large work function and in-plane anisotropy suggest unique interlayer interactions with other 2D materials. However, compared to conventional 2D materials such as graphene, hBN, or MoS<sub>2</sub>,  $\alpha$ -MoO<sub>3</sub> exhibits higher exfoliation energy [53, 63]. This can be attributed to the extremely short interatomic distance between O<sub>a</sub> atoms in adjacent layers, making it challenging to obtain ultrathin  $\alpha$ -MoO<sub>3</sub> flakes of high quality and sufficient lateral size. The thinnest thicknesses of the exfoliated  $\alpha$ -MoO<sub>3</sub> flakes are in the range of tens of nanometers [64]. This result is in contrast with other 2D materials of which monolayers with few-angstrom-thick are readily obtained. Even though there also have been approaches to synthesize  $\alpha$ -MoO<sub>3</sub> on bulk substrates such as SiO<sub>2</sub> and SrTiO<sub>3</sub>, the grown  $\alpha$ -MoO<sub>3</sub> tends to have an island shape or limited lateral size in the hundreds of nanometers range [65], which is not suitable to fabricate moiré superlattice with other 2D materials. In this regard, it is necessary to develop methods that enable the fabrication of ultrathin  $\alpha$ -MoO<sub>3</sub> with high quality and a lateral size on the scale of at least few micrometers.

In this study, I propose vdW epitaxial growth to achieve high crystalline  $\alpha$ -MoO<sub>3</sub> with a mono to few-layer structure and a large lateral size. I employed 2D

---

<sup>1</sup> The content of this Chapter is derived from a paper published in the *2D Mater.* **6**, 015016 (2019). The manuscript and figures in this Chapter have been reproduced with permission from IOP Publishing and the coauthors involved.



materials as growth templates. The dangling-bond-free and flat surface of these 2D materials enhance the surface diffusion of  $\alpha$ -MoO<sub>3</sub> precursors, facilitating the lateral growth of  $\alpha$ -MoO<sub>3</sub> (Fig. 2.1) [66].

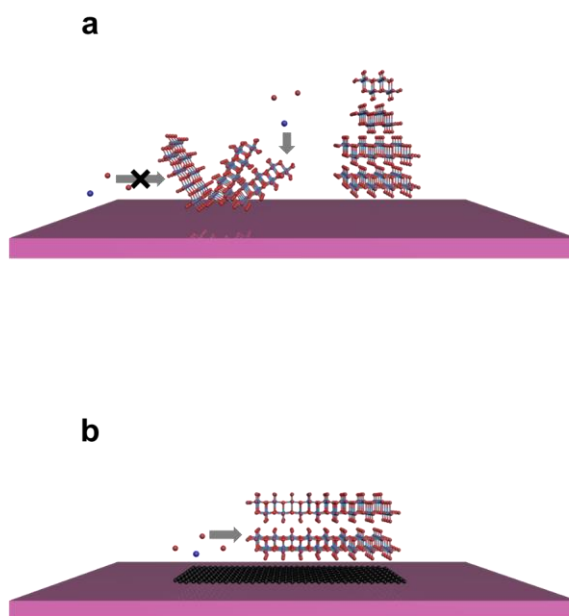


**Figure 2.1.** Schematic images of growth mechanism of  $\alpha$ - $\text{MoO}_3$  on (a) rough and amorphous substrate and (b) flat 2D templates.

## 2.2. Methods

### Sample preparation

A 50 nm-thick Mo film is deposited on a Si substrate covered with a 285 nm-thick SiO<sub>2</sub> layer using a DC magnetron sputter. The deposited Mo film serves as a source of Mo and is placed on a pre-heated heater at 550 °C in ambient conditions. The target substrate containing the 2D materials is placed upside down at 0.5 mm-above using a modified hotplate method [67, 68].

### Characterizations

Raman spectroscopy is performed using a Renishaw Raman inVia Confocal Raman microscope with a 532 nm excitation laser. Atomic force microscopy (AFM) is conducted using a Park Systems NX-10 instrument and a home-built high-resolution AFM. Transmission electron microscopy (TEM) is carried out using a JEOL JEM-ARM 200F instrument. X-ray photoelectron spectroscopy (XPS) is performed with a Thermo Scientific instrument using monochromatic Al K $\alpha$  as the X-ray source. UV-vis spectroscopy is conducted using an Agilent Cary5000 instrument, with mica serving as a transparent substrate and its effect subtracted from the measured raw data. Grazing incidence X-ray diffraction (GIXRD) is performed using a Rigaku SmartLab instrument.

### Device fabrication

After the growth of  $\alpha$ -MoO<sub>3</sub> on hBN, e-beam lithography (TESCAN Vega 3) is employed to define the source-drain electrodes on the  $\alpha$ -MoO<sub>3</sub>. Subsequently, a Cr/Au layer (1 nm/70 nm) is deposited using a thermal evaporator. Electrical measurements are carried out under ambient conditions using a semiconductor analyzer (Keithley 4200).

## 2.3. Results and Discussion

### 2.3.1. Fabrication of $\alpha$ -MoO<sub>3</sub>

Figure 2.2 illustrates the setup for growing  $\alpha$ -MoO<sub>3</sub> layers on 2D materials. A thin molybdenum film was deposited on an SiO<sub>2</sub> substrate to be used as a molybdenum source substrate. Under ambient conditions, the source substrate is placed on a heater with  $\sim 500^{\circ}\text{C}$  to form sub-stoichiometric MoO<sub>x</sub> which can be easily sublimated at relatively low temperature. Meanwhile, as a target substrate, 2D flakes are mechanically exfoliated on the other SiO<sub>2</sub> substrate. The target substrate is positioned  $\sim 0.5$  mm above the bottom target substrate with upside down. It is important to note that the target substrate is located on the heater once the growth temperature is reached to prevent damage to the 2D flakes.

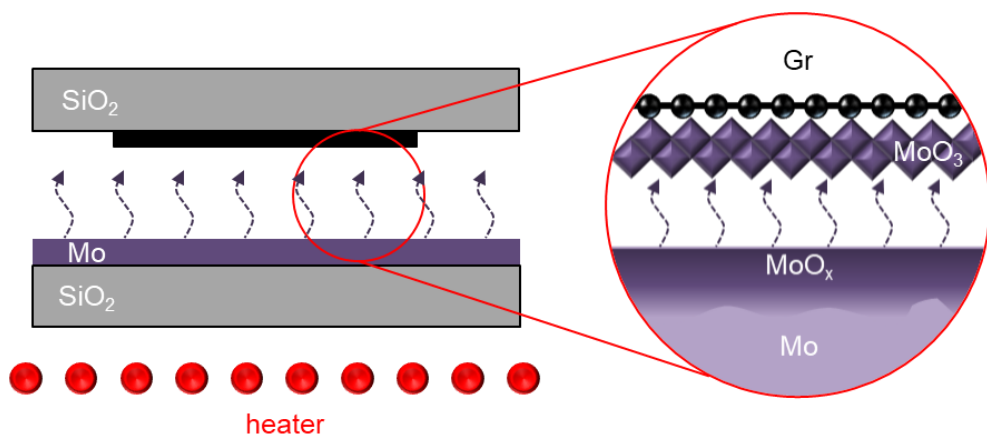


**Figure 2.2.** Schematic image of the growth system of  $\alpha$ - $\text{MoO}_3$ . Adapted from the reference [66] with permission.

### 2.3.2. Morphology $\alpha$ -MoO<sub>3</sub> and epitaxial relation with the 2D templates

The dangling-bond-free and smooth surfaces of 2D materials make them ideal growth templates by enhanced lateral migration of precursors with low energy barriers [69-71]. The growth method of  $\alpha$ -MoO<sub>3</sub> was applied to various 2D materials. The optical microscopic images demonstrate the epitaxial growth of  $\alpha$ -MoO<sub>3</sub> nanosheets on different 2D materials, including graphene, hBN, mica, and MoSe<sub>2</sub> (Fig. 2.3a). The angles between the edges of  $\alpha$ -MoO<sub>3</sub> nanosheets on various 2D materials are summarized in Fig. 2.3b. The relative angles between the edges of the  $\alpha$ -MoO<sub>3</sub> are within integer multiples of 60°, indicating alignment of  $\alpha$ -MoO<sub>3</sub> with underneath 2D materials. These results are in contrast with the morphology of  $\alpha$ -MoO<sub>3</sub> grown on non-crystalline substrates. The  $\alpha$ -MoO<sub>3</sub> synthesized on amorphous SiO<sub>2</sub>/Si and glass substrate exhibit irregular shape particles. Therefore, it can be inferred that highly crystalline and flat 2D materials act as appropriate growth templates for vdW growth of  $\alpha$ -MoO<sub>3</sub>.

AFM was used to investigate the morphology of  $\alpha$ -MoO<sub>3</sub> grown on graphene and hBN (Figs. 2.4a and b). The measured angles between the edges of the  $\alpha$ -MoO<sub>3</sub> nanosheets are approximately multiples of 60°, similar to the angle distribution measured by optical microscope. This suggests successful vdW epitaxial growth of  $\alpha$ -MoO<sub>3</sub> on multilayer graphene and hBN, consistent with the previous reports [67, 69]. The AFM height distributions of the synthesized  $\alpha$ -MoO<sub>3</sub> nanosheets and underlying graphene and hBN substrates demonstrate similar roughness between  $\alpha$ -MoO<sub>3</sub> nanosheets and the 2D substrates (Figs. 2.4c and d), indicating atomic smoothness and high crystallinity of the synthesized  $\alpha$ -MoO<sub>3</sub> nanosheets.

These results indicate that the grown  $\alpha$ -MoO<sub>3</sub> is epitaxially correlated with the crystal structures of the underlying 2D substrates. As the growth time increases, the coverage and thickness of the  $\alpha$ -MoO<sub>3</sub> nanosheets also increase. Due to the epitaxial relation between the  $\alpha$ -MoO<sub>3</sub> and 2D templates, the separated  $\alpha$ -MoO<sub>3</sub> islands

coalesce together, forming a single crystal and ultimately resulting in an atomically smooth single-crystal  $\alpha$ -MoO<sub>3</sub> film without visible grain boundaries.

To investigate the primitive growth stage of  $\alpha$ -MoO<sub>3</sub> nanosheets, they were synthesized on multilayer graphene with short growth time of 5 minutes. In the AFM image shown in Figs. 2.5a and b, it can be observed that bilayer (2L)  $\alpha$ -MoO<sub>3</sub> islands are predominantly grown with the morphology of round-cornered squares. On the other hand, the morphology of monolayer  $\alpha$ -MoO<sub>3</sub> (denoted as 1L in Figs. 2.5a and b) region is distinct from the multilayer  $\alpha$ -MoO<sub>3</sub> observed in my study and other reports [72, 73]. The monolayer  $\alpha$ -MoO<sub>3</sub> with ~0.7 nm thickness exhibits irregular shapes, and they are also mobile during AFM scanning. These results indicate its instability and weak binding to the underlying graphene substrate. The rarity of observing monolayer  $\alpha$ -MoO<sub>3</sub> in previous reports also could be attributed to the high instability and weak binding forces at the heterointerface.

To investigate epitaxial relation between  $\alpha$ -MoO<sub>3</sub> and graphene, high-resolution AFM was conducted on the 2L  $\alpha$ -MoO<sub>3</sub> (red square) and the adjacent graphene regions (blue square in Fig. 2.5c). It was available to capture atomic-scale patterns in both the height and friction images. The friction images obviously demonstrate the crystal structures of  $\alpha$ -MoO<sub>3</sub> and graphene through atomic-scale stick-slip phenomena (Fig. 2.5d) [74-76]. The friction image of 2L  $\alpha$ -MoO<sub>3</sub> revealed quasi-square patterns (red lines) with an interatomic distance of around 0.4 nm. On the other hand, multilayer graphene shows rhombic patterns with a length of around 0.3 nm indicated by blue lines in Fig. 2.5d, resembling AB stacking structure of graphite [72, 77, 78]. In addition, it also can be noted that the c-axis of  $\alpha$ -MoO<sub>3</sub> aligns with zigzag direction of graphene which supports the epitaxial growth of  $\alpha$ -MoO<sub>3</sub> on graphene. The crystal structure of graphene was maintained perfectly, demonstrating negligible damage during the growth procedure.

Furthermore,  $\alpha$ -MoO<sub>3</sub>/graphene heterostructure was examined using plan-view TEM, as depicted in Fig. 2.6a. The TEM image in Fig. 2.6a corroborated the AFM results in Fig. 2.5d by revealing a distinct rectangular lattice structure with

dimensions of  $0.40\text{ nm} \times 0.38\text{ nm}$  along the a- and c-axes, respectively. Additionally, the selected area electron diffraction pattern (SAED) shown inset of Fig. 2.6a provided further evidence of the epitaxial relationship between the  $\alpha\text{-MoO}_3$  and graphene, with red and yellow circles representing the diffraction spots of  $\alpha\text{-MoO}_3$  and graphene, respectively. The (001) direction of  $\alpha\text{-MoO}_3$  was found to be aligned with one of zigzag direction of the underlying graphene.

A high-resolution cross-section TEM image Fig. 2.6b was obtained to gain detailed insight into the interface between  $\alpha\text{-MoO}_3$  and graphene. The uniformly grown  $\alpha\text{-MoO}_3$  film exhibits interlayer spacing of approximately  $0.7\text{ nm}$ , corresponding to the thickness of a monolayer of  $\alpha\text{-MoO}_3$ . The  $\alpha\text{-MoO}_3$  layers appear continuous and smooth, confirming the absence of grain boundaries. These observations validate the growth of single crystalline  $\alpha\text{-MoO}_3$  films on 2D growth templates. In addition, the layered structures of multilayer graphene are also well-preserved with an interlayer distance of  $0.35\text{ nm}$ . However, the very first  $\alpha\text{-MoO}_3$  layer on multilayer graphene exhibited slightly blurred structure in comparison with the above-deposited  $\alpha\text{-MoO}_3$  layers. As discussed above, the first monolayer is unstable and weakly bound with the graphene template. Consequently, it can be inferred that the initial  $\alpha\text{-MoO}_3$  layer acts as a buffer layer to relax the strain induced during epitaxial growth. This buffer layer accommodates the lattice mismatch strain, preventing further transmission of strain to the upper layers [75, 79]. This finding coincides with the emergence of the  $\alpha$ -phase structure immediately after completing bilayer  $\alpha\text{-MoO}_3$  growth on Au substrates [67, 72, 74, 76, 80-83]. Theoretical predictions also support this observation, indicating a substantial increase in the elastic modulus of  $\alpha\text{-MoO}_3$  as discussed in the Chapter 1.2.2.1 [54]. Hence, the initial layer of  $\alpha\text{-MoO}_3$  performs an important role to relax lattice misfit strain. Once the strain is substantially relaxed by the initial layer, the growth of  $\alpha\text{-MoO}_3$  on multilayer graphene becomes feasible, as illustrated in the schematic diagram of Fig. 2.6c.



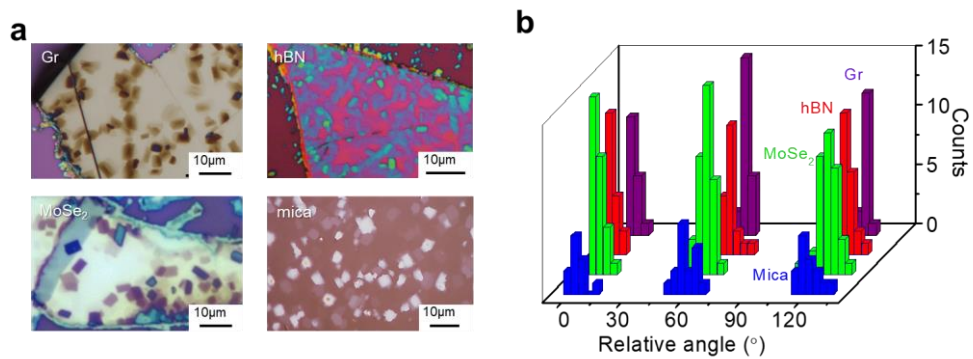


**Figure 2.3.** (a) Optical microscope image of  $\alpha$ - $\text{MoO}_3$  on various 2D templates. (b). Statistical distribution of angle between longer edges of  $\alpha$ - $\text{MoO}_3$ . (a) and (b) are adapted from the reference [66] with permission.

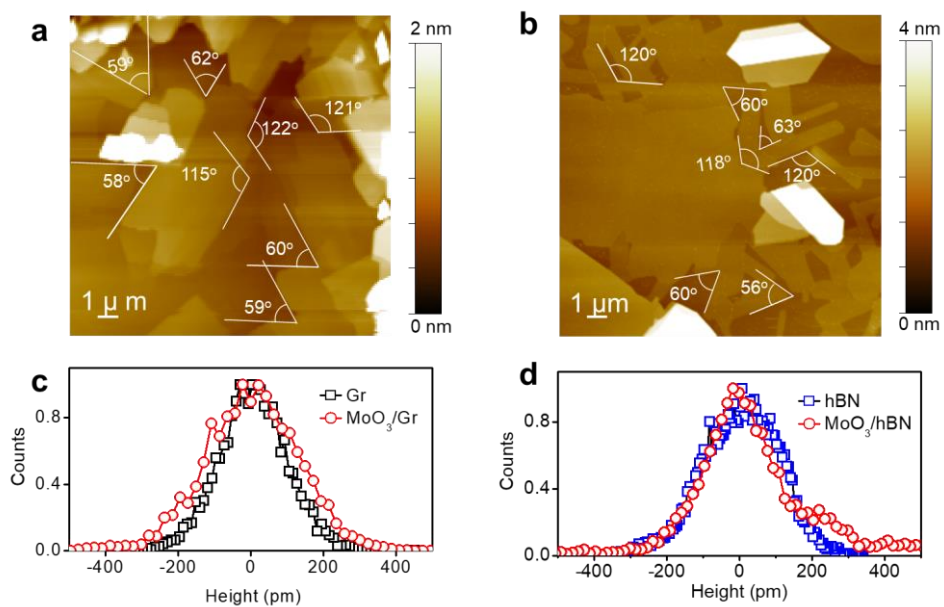


**Figure 2.4.** AFM images of  $\alpha$ - $\text{MoO}_3$  on (a) multilayer graphene and (b) hBN. AFM height distribution of  $\alpha$ - $\text{MoO}_3$  on (c) multilayer graphene and (d) hBN. (a-d) are adapted from the reference [66] with permission.

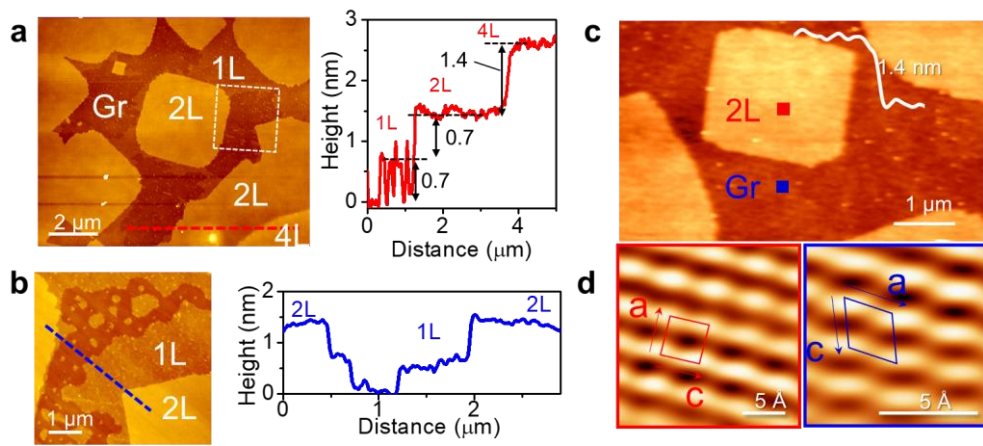


**Figure 2.5.** (a) AFM image and line profile at the primitive growth stage of  $\alpha$ -MoO<sub>3</sub>. (b) A magnified image and line profile at white box in (a). (c) High resolution AFM image of 2L  $\alpha$ -MoO<sub>3</sub> and exposed multilayer graphene. (d) Friction images of 2L  $\alpha$ -MoO<sub>3</sub> (left) and multilayer graphene (right). (a-d) are adapted from the reference [66] with permission.

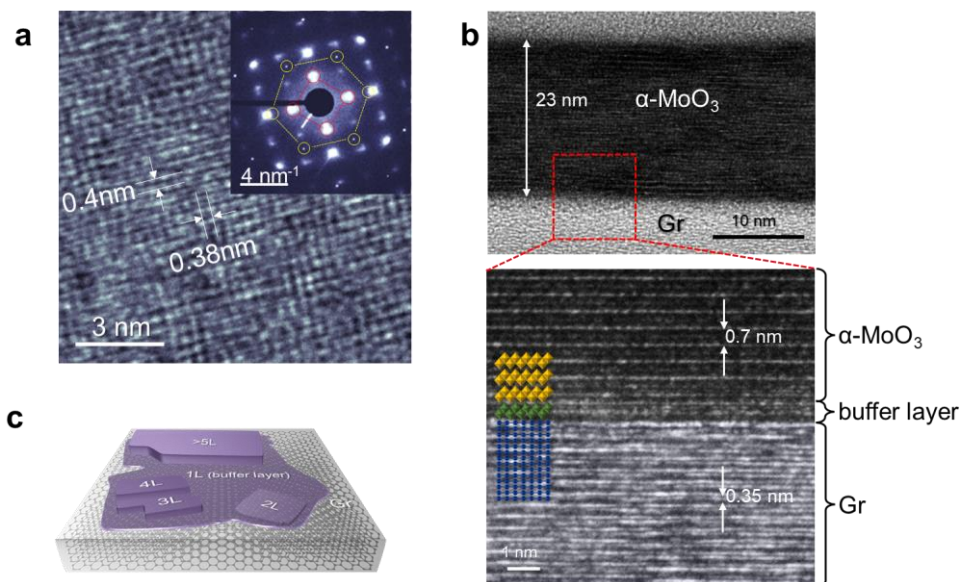


**Figure 2.6.** (a) Top-view TEM image and SAED (inset) of  $\alpha$ -MoO<sub>3</sub>/graphene heterostructure. (b) Cross-section TEM images of  $\alpha$ -MoO<sub>3</sub>/graphene. (c) Schematic image representing growth mechanism of  $\alpha$ -MoO<sub>3</sub> on graphene. (a-c) are adapted from the reference [66] with permission.

### 2.3.3. Crystallinity of $\alpha$ -MoO<sub>3</sub>

To analyze the crystal structure of  $\alpha$ -MoO<sub>3</sub>, a grazing incidence X-ray diffraction (GIXRD) measurement was performed on a thick  $\alpha$ -MoO<sub>3</sub> film (20–30 nm) grown on multilayer graphene (Fig. 2.7a). Four main peaks at 13°, 26°, 39°, and 52° are observable, and they correspond with (020), (040), (060), and (080) planes of  $\alpha$ -MoO<sub>3</sub>, respectively. These peaks matched the reference positions of  $\alpha$ -MoO<sub>3</sub> (ICCD, No. 01-074-7909). The interlayer spacing of  $\alpha$ -MoO<sub>3</sub>, calculated from the diffraction peak of (020), was found to be 0.692 nm, which coincides with the value measured by AFM and TEM. By the absence of other peaks, it can be confirmed that the crystal structure of the  $\alpha$ -MoO<sub>3</sub> film is highly oriented along the b-axis, distinguishing it from the growth methods leading to formation of randomly oriented  $\alpha$ -MoO<sub>3</sub> [77, 84]. The small width of the diffraction peaks ( $\sim 0.3^\circ$ ) demonstrates the outstanding crystallinity of the  $\alpha$ -MoO<sub>3</sub>.

The crystal structure of ultrathin  $\alpha$ -MoO<sub>3</sub> nanosheets with different thicknesses ranging from 2L to 18L at the micron scale was confirmed by Raman spectroscopy (Fig. 2.7b). The left and right panels of the figure represent the characteristic Raman bands of  $\alpha$ -MoO<sub>3</sub> and multilayer graphene (growth template), respectively. The peak positions of the Raman spectra for  $\alpha$ -MoO<sub>3</sub> nanosheets of different thicknesses did not exhibit any noticeable shifts, except for variations in peak intensities. The most prominent Raman peak is centered at 817 cm<sup>-1</sup> [78, 85]. Despite the weak Raman intensities of ultrathin  $\alpha$ -MoO<sub>3</sub> nanosheets, even 2L  $\alpha$ -MoO<sub>3</sub> shows an observable Raman peak at 817 cm<sup>-1</sup>. However, the peak cannot be identified for monolayer  $\alpha$ -MoO<sub>3</sub> which can be attributed to its instability and non-crystalline structure.

For the graphene template, an indicator of defects on graphene was not observable (Fig. 2.7b). This observation, in accordance with the AFM and TEM images, suggests that the graphene remains intact during  $\alpha$ -MoO<sub>3</sub> growth. The relative intensities of the  $\alpha$ -MoO<sub>3</sub> Raman peak at 817 cm<sup>-1</sup> and the G peak of

multilayer graphene ( $I(\text{MoO}_3)/I(\text{Gr})$ ) were plotted as a function of  $\alpha\text{-MoO}_3$  thickness (Fig. 2.7b). The relative intensity increased with the number of  $\alpha\text{-MoO}_3$  layers. Notably, the Raman spectrum in Fig. 2.7b does not show significant shift in the  $\alpha\text{-MoO}_3$  Raman peak, distinct from the behavior observed in TMDCs [86].

XPS was conducted to investigate the composition of the grown  $\alpha\text{-MoO}_3$  on multilayer graphene. The resulting Mo 3d core-level spectra revealed two doublets corresponding to two different oxidation states:  $\text{Mo}^{6+}$  (red curve) and  $\text{Mo}^{5+}$  (blue curve). The binding energies of Mo 3d 5/2 were measured at 235.8 eV (234.8 eV) for  $\text{Mo}^{6+}$  ( $\text{Mo}^{5+}$ ). The ratio of  $\text{Mo}^{6+}$  is dominant compared to  $\text{Mo}^{5+}$  (94:6). By comparing the peak areas of  $\text{Mo}^{6+}$  and  $\text{Mo}^{5+}$  to O 1s, the atomic ratio of molybdenum and oxygen was calculated as Mo:O = 1:2.84, indicating a deficient amount of oxygen in the  $\alpha\text{-MoO}_3$  film [83, 87, 88]. This oxygen deficiency is attributed to the presence of oxygen vacancies, which have a low formation energy. Additionally, the  $\text{Mo}^{6+}$  cation is vulnerable to reduction to the lower  $\text{Mo}^{5+}$  state through electron transfer by the chemical potential difference with graphene or surface dipoles of water and OH bonds at the interface [89, 90].

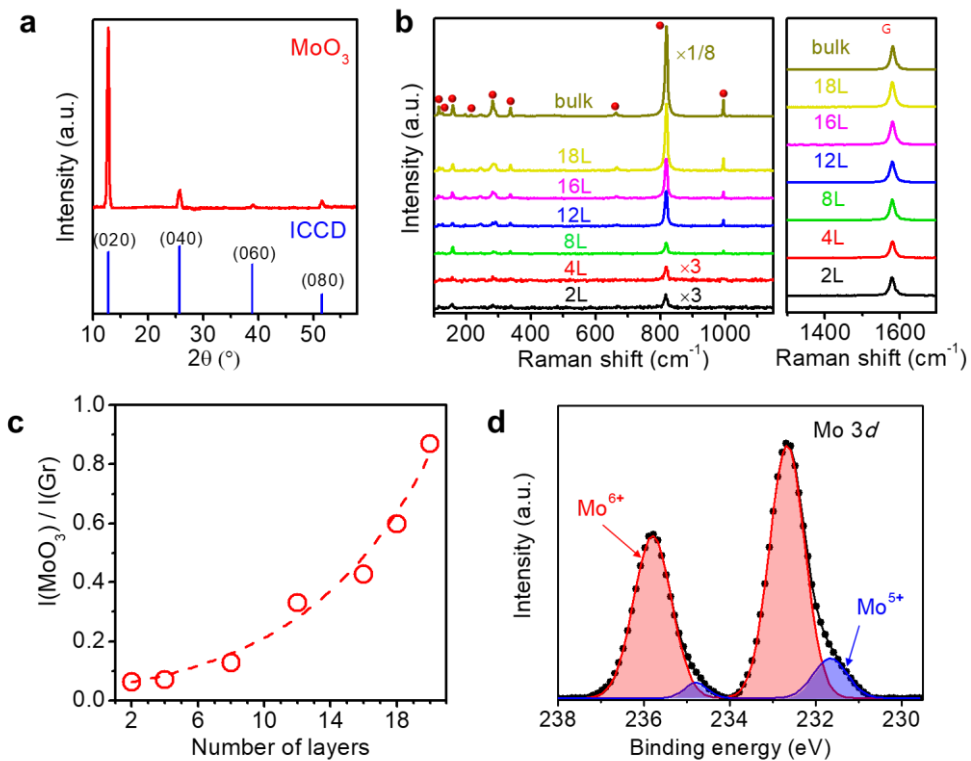


**Figure 2.7.** (a) GIXRD result of the  $\alpha$ - $\text{MoO}_3$  on multilayer graphene. (b) Raman spectra of  $\alpha$ - $\text{MoO}_3$  on multilayer graphene as a function of  $\alpha$ - $\text{MoO}_3$  thickness. (c) Ratio between Raman intensities of  $\alpha$ - $\text{MoO}_3$  and graphene. (d) XPS result of Mo 3d core level composed with  $\text{Mo}^{6+}$  and  $\text{Mo}^{5+}$  states. (a-d) are adapted from the reference [66] with permission.

### 2.3.4. Band structure and electrical properties of $\alpha$ -MoO<sub>3</sub>

To investigate the electronic band structure of  $\alpha$ -MoO<sub>3</sub>, ultraviolet-visible absorption measurements were conducted on  $\alpha$ -MoO<sub>3</sub> grown on mica with various growth durations (Fig. 2.8a). The indirect band gap of  $\alpha$ -MoO<sub>3</sub> was calculated by using Tauc's equation. The resulting data showed that the band gap of  $\alpha$ -MoO<sub>3</sub> increased with decreasing growth time, ranging from 2.9 eV for bulk  $\alpha$ -MoO<sub>3</sub> to 3.2 eV for the thinnest portion (Fig. 2.8b) [91]. This contradicts previous reports suggesting a constant band gap in  $\alpha$ -MoO<sub>3</sub>, which is expected due to weak interlayer interaction [67]. The observed increase in band gap for thinner  $\alpha$ -MoO<sub>3</sub> may be attributed to the formation of amorphous-phase monolayer  $\alpha$ -MoO<sub>3</sub>, which has a larger band gap, strain accumulated at the interface, and strong interaction with the underlying 2D substrate [92]. However, further studies are required to verify this hypothesis.

Ultraviolet photoelectron spectroscopy (UPS) was performed on  $\alpha$ -MoO<sub>3</sub> grown on multilayer graphene for 10 minutes (Fig. 2.8c). The UPS spectrum revealed that the VBM of  $\alpha$ -MoO<sub>3</sub> is located 2.8 eV below the Fermi level (Fig. 2.8d). In addition, gap states ( $d_1$  state) were observed between the Fermi level and the VB edge, resulting from the oxygen vacancies. The reduction of Mo<sup>6+</sup> to Mo<sup>5+</sup> and the occupation of excess electrons in the gap states lead to n-doping of  $\alpha$ -MoO<sub>3</sub> [93-95]. The work function of  $\alpha$ -MoO<sub>3</sub> was estimated to be 4.6 eV, indicating a highly n-doped nature. The low work function is attributed to the presence of oxygen vacancies and surface adsorbates [96], which can be improved by surface cleaning [87, 90].

To investigate electrical properties of  $\alpha$ -MoO<sub>3</sub>, a field-effect transistor (FET) was fabricated (Fig. 2.8e). An  $\alpha$ -MoO<sub>3</sub> flake on grown hBN was used as a channel. The output curves showed a linear increase with drain voltage and gate-voltage dependence, indicating n-type transport behavior. The observed n-type behavior is consistent with the above investigated electronic band structure of  $\alpha$ -MoO<sub>3</sub>. The  $\alpha$ -



MoO<sub>3</sub> FET exhibited on/off ratio of approximately 10<sup>3</sup>, and its field-effect mobility of electron was 0.03 cm<sup>2</sup> V<sup>-1</sup> s<sup>-1</sup>. The relatively low field-effect mobility may be attributed to high contact resistance and charged impurity scattering caused by oxygen vacancies. Since the measured mobility is highly smaller than the theoretical values (~1000 cm<sup>2</sup> V<sup>-1</sup> s<sup>-1</sup>), further optimization including surface encapsulation, surface treatment, and contact engineering is necessary to realize the full potential of  $\alpha$ -MoO<sub>3</sub>.

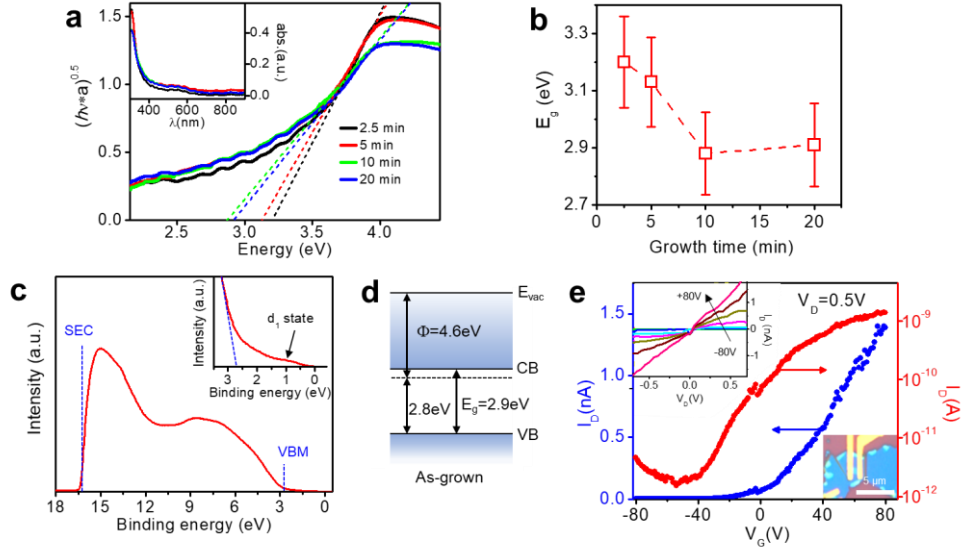


**Figure 2.8.** (a) UV-vis absorption spectra of  $\alpha$ -MoO<sub>3</sub> grown on mica with different growth time. (b) Energy band gaps measured from (a) as a function of growth time. (c) UPS valence band spectrum of  $\alpha$ -MoO<sub>3</sub>. The secondary cut-off (SEC) and VBM were determined as indicated by blue dashed lines. (d) Schematic band structure of  $\alpha$ -MoO<sub>3</sub> estimated from the UPS and UV-vis spectra analyses. (e) Electrical properties of the  $\alpha$ -MoO<sub>3</sub> field-effect transistor. (a-d) are adapted from the reference [66] with permission.

## 2.4. Conclusion

In conclusion, I have successfully developed a vdW growth technique for producing large and single crystalline  $\alpha$ -MoO<sub>3</sub> nanosheets on 2D growth templates. Through this method, I achieved high-quality epitaxial growth of  $\alpha$ -MoO<sub>3</sub> nanosheets on various 2D materials, with a strong alignment with underlying 2D materials and the initial  $\alpha$ -MoO<sub>3</sub> layer. I have also investigated the thickness-dependent crystal structure and band structure of ultrathin  $\alpha$ -MoO<sub>3</sub> nanosheets. The epitaxially grown  $\alpha$ -MoO<sub>3</sub> exhibited a significant band gap ranging from 2.9 to 3.2 eV and a small work function of 4.6 eV, indicating a high n-doping level attributed to oxygen vacancies and surface chemicals. Consequently, FETs based on  $\alpha$ -MoO<sub>3</sub> demonstrated n-type characteristics, with a moderate on/off ratio.  $\alpha$ -MoO<sub>3</sub> holds enormous potential as essential components in future electronic devices based on 2D materials, serving a wide-band gap semiconductor.

# Chapter 3. Thickness-Insensitive Properties of $\alpha$ -MoO<sub>3</sub> Nanosheets by Weak Interlayer Coupling<sup>2</sup>

## 3.1. Introduction

After development of the growth method, it is required to investigate of mechanical and electrical properties of the vdW epitaxially grown  $\alpha$ -MoO<sub>3</sub> to utilize it as a building block for vdW heterostructures.

It has been known that bulk  $\alpha$ -MoO<sub>3</sub> has high dielectric constant of 6-18 [89, 97-99]. Furthermore, theoretical studies predicted that the variation of orbital overlapping in  $\alpha$ -MoO<sub>3</sub> is negligibly small regardless of the number of layers, i.e., the electrical and mechanical properties of  $\alpha$ -MoO<sub>3</sub> would have small correlation with the number of layers [54, 100]. Because most of the 2D insulating materials show thickness-sensitive properties such as dielectric constant, breakdown voltage, and friction, the 2D insulators that retain the bulk properties are highly required for nanoelectronics applications. Despite tremendous attempts to obtain  $\alpha$ -MoO<sub>3</sub> nanosheets [66, 67, 69, 101], the detailed research of thickness-dependent characteristics of the  $\alpha$ -MoO<sub>3</sub> is still obscure due to the limited crystallinity of  $\alpha$ -MoO<sub>3</sub> nanosheets.

Here I comprehensively investigated electrical and tribological properties of  $\alpha$ -MoO<sub>3</sub> on graphite by using scanning probe microscopy (SPM). I found that  $\alpha$ -MoO<sub>3</sub> has higher friction compared to graphene, reduced work function (4.73 eV for > 2L) compared to bulk  $\alpha$ -MoO<sub>3</sub>, and high dielectric constant (6 for 2L and 10.5~11 for > 3L). Interestingly, all the properties are independent of the thickness due to weak

---

<sup>2</sup> The content of this Chapter is derived from a paper published in the *Nano Lett.* **19**, 8868 (2019). The manuscript and figures in this Chapter have been reproduced with permission from ACS Publications and the coauthors involved.

interlayer coupling, which is distinctive from the most of the 2D materials showing thickness-sensitive properties.

## 3.2. Methods

### Sample preparation

Using a DC magnetron sputter, sufficiently thick Mo film ( $> 100$  nm) is first deposited on a SiO<sub>2</sub> (285 nm)/Si substrate. Multiple graphite flakes were prepared on the target substrate via mechanical exfoliation. The Mo-deposited substrate is placed onto a pre-heated heater of 550 °C in ambient conditions, and the target substrate with 2D materials is placed 0.5 mm-above the source substrate. The thickness and coverage of the synthesized  $\alpha$ -MoO<sub>3</sub> film are controlled by varying the deposition time.

### Material Characterizations

The as-grown samples were examined by Raman spectroscopy (Renishaw Raman, inVia Confocal Raman microscope with a 532-nm excitation laser) as a preliminary test. All kinds of SPM measurements were carried out by NX-10 (Park systems) at the ambient conditions. For contact modes like friction force microscopy (FFM) and conductive AFM (c-AFM), soft Pt-coated tip (PPP-CONTSCPT, Nanosensors) was used, and its nominal spring constant is as small as  $\sim 0.2$  N m<sup>-1</sup>. The loading force was set at  $\sim 2$  nN. The elastic constant of the tip was calibrated relying on the method of Cleveland *et al.* [102] where the elastic constant ( $k$ ) of a rectangular probe can be defined as  $k = 2\pi^3 l^3 w \rho^{1.5} E^{-0.5} f_0^3$  [102]. Here,  $l$  and  $w$  correspond to the length and width of the cantilever, respectively, which are measured by scanning electron microscopy. The elastic modulus ( $E$ ) and the density ( $\rho$ ) are set by the manufacturer-provided specifications.  $f_0$  is the resonance frequency of the tip when tip is disengaged from the sample. In addition, the lateral torsion signal of the used AFM tip can be converted to the unit of nN based on Tocha *et al.* [103] and trapezoidal silicon grating sample (TGF11, MIKROMASCH). During the friction ( $F_f$ ) versus AFM tip loading force ( $F_{tip}$ ) spectroscopy ( $F_{tip}$ - $F_f$ ), the motion

along the slow-scan ( $Y$ ) direction was fixed so that only a single line along  $X$ -direction is repeatedly scanned. While the loading force was changed on a line-by-line basis, the differences between the forward and backward lateral signals were recorded from 512 lines. Therefore, the friction force for each loading force was calculated by averaging each data set (i.e., 256 measurements).

For the c-AFM measurements, a specimen was mounted on a metallic sample holder, and the external current amplifier (DLPCA-200, FEMTO) was used to measure the extremely low current. Tip was directly connected to the signal ground of amplifier while the bias voltage is applied to the sample stage. The current gain was set at  $10^8 \text{ V A}^{-1}$ . Like FFM, soft tip coated by Pt (PPP-CONTSCPT, Nanosensors) was used to reduce the scan damage to surface. To minimize the tip damages caused by the excessive tip-current, the bias-sweeping range was controlled at  $\sim +2 \text{ V}$ .

As the contact potential difference (CPD) results of KPFM (Kelvin probe force microscopy) should be applied to local dielectric constant, KPFM and measurement of local dielectric constant were conducted sequentially. I used an identical Au-coated non-contact tip (PPP-NCSTAu, Nanosensors) whose elastic constant was  $\sim 7.4 \text{ N m}^{-1}$  and the resonance frequency is  $\sim 170 \text{ KHz}$  [104]. The topography and surface potential signal were measured simultaneously with a mechanical drive frequency of  $75 \text{ kHz}$  and an AC modulation of  $1 \text{ V}$  at  $10 \text{ kHz}$ . The first harmonics of the force ( $F_{1\omega}$ ) exerting on the tip were extracted by Lock-in technique [104]. In my KPFM system, CPD was decided as tip voltage bias to nullify the electrostatic force existing between a conductive tip and a sample. As shown in the equation (3.8), if the value is assumed to be equivalent to the difference of work function or Fermi level between tip and sample, the site-depending variation of work function of sample can be identified. Meanwhile, when  $F$ - $D$  spectroscopy was performed to find dielectric constant of  $\alpha\text{-MoO}_3$ ,  $+9\text{V-DC}$  bias was applied to tip to enhance the electrostatic force between tip and sample. Both AC modulations (for topography and KPFM) were shut down.

### 3.3. Results and Discussion

#### 3.3.1. Fabrication of $\alpha$ -MoO<sub>3</sub>

To examine the electrical and mechanical properties,  $\alpha$ -MoO<sub>3</sub> nanosheets were epitaxially grown on graphite in a way suggested in Chapter 2. Graphite, which is both conductive and atomically smooth, served as the growth template. To ensure partial exposure of the graphene surface,  $\alpha$ -MoO<sub>3</sub> was deposited by evaporating a thin Mo film in ambient air for a short growth time of 5 minutes. This led to the formation of  $\alpha$ -MoO<sub>3</sub> partially covering the graphene surface. The  $\alpha$ -MoO<sub>3</sub> nanosheets grown on graphite is hard to be recognized in the optical microscopic image of Fig. 3.1a. However, AFM topography image in the inset of Fig. 3.1b show that square-like  $\alpha$ -MoO<sub>3</sub> nanosheets are synthesized on the surface of graphite.



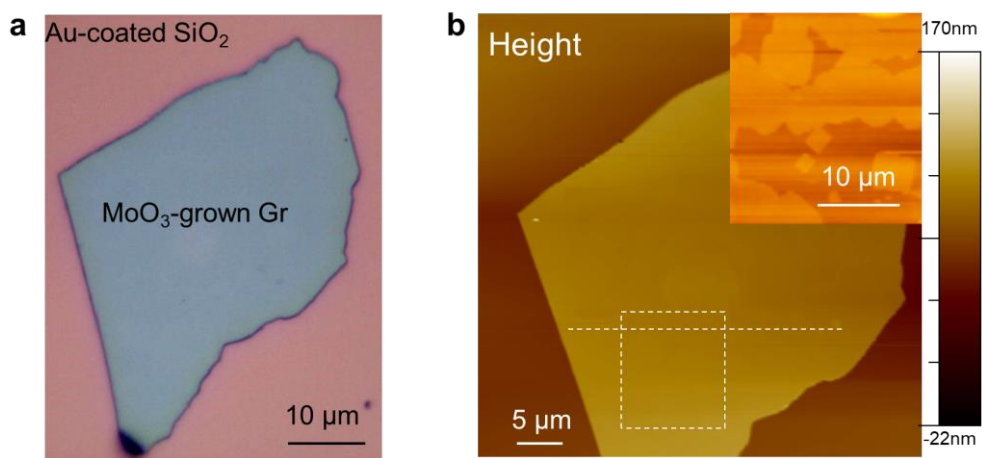


**Figure 3.1.** (a) Optical microscopic and (b) AFM images of  $\alpha$ -MoO<sub>3</sub>-grown graphite flake on an Au-coated SiO<sub>2</sub> substrate. (a) and (b) are adapted from the reference [105] with permission.

### 3.3.2. Surface properties of $\alpha$ -MoO<sub>3</sub> and graphite

Surface properties of the synthesized  $\alpha$ -MoO<sub>3</sub> were thoroughly examined by FFM, c-AFM, and KPFM (Fig. 3.2a). Figures 3.2b-d display the friction, CPD, and current images of the  $\alpha$ -MoO<sub>3</sub> nanosheets grown on graphene surface, respectively. Similarly, the line profiles in Fig. 3.2e show height, friction, CPD, and current along the white dashed line of Figs. 3.2b-d. Analysis of the height profile reveals that the thinnest  $\alpha$ -MoO<sub>3</sub> nanosheets (bilayer) possess a thickness of 1.4 nm, which coincide with the unit lattice length along b-axis. Furthermore, the thickness of monolayer  $\alpha$ -MoO<sub>3</sub> is measured to be 0.7 nm, equivalent to half of the unit lattice length along the b-axis. In comparison to graphene, the  $\alpha$ -MoO<sub>3</sub> nanosheets demonstrate distinct surface properties, including larger friction, smaller CPD, and larger electrical resistivity. These contrasting characteristics allow for the differentiation between  $\alpha$ -MoO<sub>3</sub> and graphene, based on their surface properties.

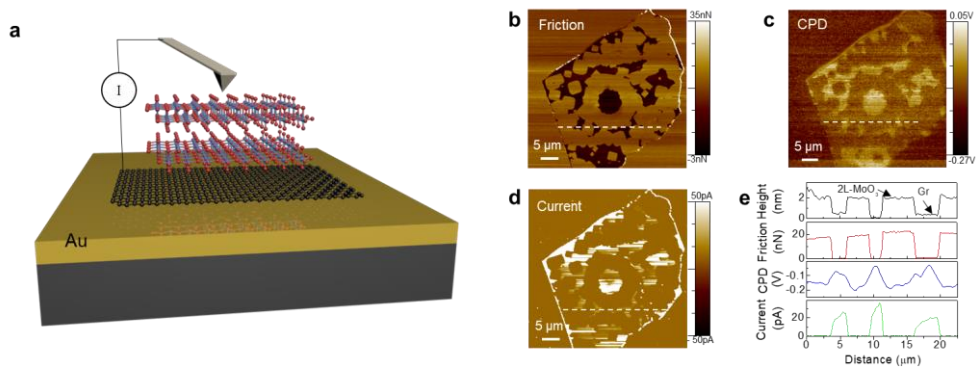


**Figure 3.2.** (a) SPM set-up for characterization of surface properties in  $\alpha$ -MoO<sub>3</sub>/graphite on Au-coated SiO<sub>2</sub> substrate. (b) Friction, (c) CPD, and (d) current images obtained by different AFM modes of FFM, KPFM, and c-AFM, respectively. (e) Profiles of height, friction, CPD, and current obtained along the white dashed lines of (b-e). (a-e) are adapted from the reference [105] with permission.

### 3.3.3. Tribological properties of $\alpha$ -MoO<sub>3</sub>

AFM/FFM studies have proven to be valuable for exploring the nanotribological properties of 2D materials, allowing for the investigation of phenomena such as stick-slip behavior [106]. Previous research has also highlighted the thickness-dependent friction tendencies of exfoliated 2D materials, attributed to the puckering effect [75]. Here, the friction of  $\alpha$ -MoO<sub>3</sub> nanosheets with different thicknesses was investigated from 2L to 7L (Figs. 3.3a and b), following the calibration of the AFM tip cantilever's spring constant and friction force [102]. The results of monolayer  $\alpha$ -MoO<sub>3</sub> were not included due to its instability [66].

The friction image shown in Fig. 3.3b at loading force of 2 nN demonstrates that the friction of  $\alpha$ -MoO<sub>3</sub> does not show clear thickness-dependence. To investigate the correlation between the layer number and friction, height, and friction profiles along the white dashed lines of Figs. 3.3a and b are plotted in Fig. 3.3c

It can be observed that the friction of 2L  $\alpha$ -MoO<sub>3</sub> is larger than that of the graphite by 11 nN. Interestingly, as shown in the inset of Fig. 3.3c, the friction of  $\alpha$ -MoO<sub>3</sub> is rapidly saturated as the thickness increases (more than 3L). This result is distinctive from the 2D materials usually exhibiting thickness dependence. The difference in friction between 2L and 3L  $\alpha$ -MoO<sub>3</sub> is only 1 nN, and no further change in friction is observed beyond 3L.

Since FFM images also can be affected by adhesion, the adhesive properties of  $\alpha$ -MoO<sub>3</sub> were investigated by force-distance ( $F$ - $D$ ) spectroscopy. As shown in Figs. 4b and c, the pull-off forces of  $\alpha$ -MoO<sub>3</sub> nanosheets (38.0–38.8 nN) were slightly larger compared with that of graphene (~36 nN). This marginal difference results from a slightly higher tip-surface interaction of  $\alpha$ -MoO<sub>3</sub>. In addition, the surface roughness of  $\alpha$ -MoO<sub>3</sub> nanosheets (0.13 nm) is slightly larger than that of graphene (0.1 nm) as shown in Fig. 3.4a.

A plot of  $F_{\text{tip}}-F_{\text{f}}$  is presented in Fig. 3.3d for quantitative investigation of the

local friction features. The spectroscopy was performed by scanning the surface of  $\alpha$ -MoO<sub>3</sub> nanosheets with the same thickness along 100 nm at different loading forces and with a fixed scan speed of 1 Hz. It is observed that the friction shows linear relation to the loading force for all cases, following the relation:

$$F_f = \mu(F_{tip} + F_{adh}) \cdots \cdots \cdots \text{equation (3.1)}$$

where  $\mu$  and  $F_{adh}$  are friction coefficient and adhesion force at a zero nominal normal force, respectively [107, 108].

The graphene surface without  $\alpha$ -MoO<sub>3</sub> exhibited friction coefficient of 0.01, in accordance with the superlubricity of graphite [109]. On the other hand, the friction coefficients of  $\alpha$ -MoO<sub>3</sub> were 0.158, 0.168, and 0.173 for 2L, 3L, and 7L, respectively (inset of Fig. 3.3d), exhibiting thickness-insensitive after 3L.

The extremely short interatomic distance between O<sub>a</sub> atoms leads to large lateral stiffness. The friction of  $\alpha$ -MoO<sub>3</sub> on graphite can be estimated by the shear deformation of  $\alpha$ -MoO<sub>3</sub> layers based on the 2D-multiple spring model [110, 111]:

$$\frac{1}{K_t} = \frac{1}{K_{\perp,interf}} + \frac{n-1}{K_{\perp}} + \frac{1}{K_{\parallel}} \cdots \cdots \cdots \text{equation (3.2)}$$

where  $n$  is the number of layers of 2D material anchored by substrate,  $K_t$  is the total lateral stiffness of tip-sample system,  $K_{\parallel}$  and  $K_{\perp}$  are the intralayer and interlayer stiffness, respectively, and  $K_{\perp,interf}$  is the interlayer stiffness at the interface between  $\alpha$ -MoO<sub>3</sub> and graphite [105]. The  $K_{\parallel}$  and  $K_{\perp}$  are determined by the strong in-plane interatomic bonding and weak vdW bonding, respectively. Therefore,  $K_{\parallel}$ -term is generally ruled out due to the strong covalent bonds but negligible vdW force for conventional 2D materials. However, the distance between the nearest atoms in two adjacent layers of  $\alpha$ -MoO<sub>3</sub> is dramatically shorter than that of graphene (~0.34 nm) and MoS<sub>2</sub> (~0.31 nm) [112]. Due to extremely short

interatomic distance of  $\alpha$ -MoO<sub>3</sub> notably increases  $K_{\perp}$ , which in turn result in suppression of the  $K_{\perp}$ -term on the  $K_t$  [54]. This hypothesis can be supported by theoretically calculated interlayer sliding energy of  $\alpha$ -MoO<sub>3</sub>, graphene, and MoS<sub>2</sub>. The interlayer sliding energy between  $\alpha$ -MoO<sub>3</sub> layers (~500 meV) is much larger than those of graphene (~10 meV) and MoS<sub>2</sub> (~50 meV) [112-114]. Therefore, the layer dependence of total friction is greatly weakened by extremely high  $K_{\perp}$  of  $\alpha$ -MoO<sub>3</sub>. When the layer number of  $\alpha$ -MoO<sub>3</sub> is very few, the incommensurate interface (made by orthorhombic  $\alpha$ -MoO<sub>3</sub> and hexagonal graphene) is likely to reduce the friction to some extent, which was reported in some other incommensurate systems [115].

Atomic-resolution friction images were acquired to verify the hypothesis in the lattice scale. In Figs. 3.4d and e, line profiles of the friction force for  $\alpha$ -MoO<sub>3</sub> and graphite are represented, respectively. The measured frictional patterns of  $\alpha$ -MoO<sub>3</sub> exhibit rectangular 0.4 nm  $\times$  0.4 nm periodicities (inset of Fig. 3.4d), which coincide with the crystal structure and lattice constant of the bulk  $\alpha$ -MoO<sub>3</sub> (schematic inset of Fig. 3.3c). Similarly, graphite shows the triangular patterns with a length of approximately 0.3 nm (inset of Fig. 3.4e). The effective lateral stiffness was determined from the slopes of the lateral forces in the stick regions ( $K_m$ , indicated by blue solid lines in Figs. 3.4d and e). The values of  $K_m$  for  $\alpha$ -MoO<sub>3</sub> and graphite are approximately 5.2 and 2.6 N m<sup>-1</sup>, respectively.

The area of the friction hysteresis loop represents the energy dissipated during a scanning cycle. While the hysteresis on graphite is negligible, that of  $\alpha$ -MoO<sub>3</sub> is more significant due to its different crystal structure. The effective lateral stiffness between the tip and 2D surface was estimated based on the 1D Prandtl-Tomlinson (PT) model. The lateral stiffnesses of  $\alpha$ -MoO<sub>3</sub> and graphite are 6.3 and 3.2 N m<sup>-1</sup>, respectively, demonstrating twice larger values for  $\alpha$ -MoO<sub>3</sub>. It is important to note that the peculiar crystal structure of  $\alpha$ -MoO<sub>3</sub> contributes to increased friction and higher lateral stiffness. Therefore, the increased  $K_{\perp}$  in  $\alpha$ -MoO<sub>3</sub> weakened the layer dependence of the effective lateral stiffness in the equation (3.2).

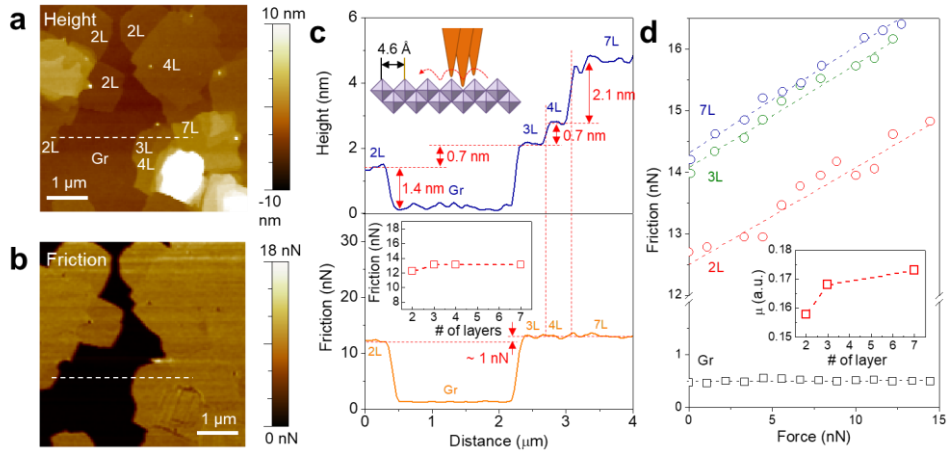


**Figure 3.3.** (a) Morphology and (b) friction images of  $\alpha$ -MoO<sub>3</sub> on graphite. (c) Line profiles of height and friction along the white dashed lines in (a) and (b), respectively. Inset of upper (c) Schematic for stick-slip behavior on the  $\alpha$ -MoO<sub>3</sub> surface. Inset of lower (c) The friction of  $\alpha$ -MoO<sub>3</sub> as a function of  $\alpha$ -MoO<sub>3</sub> layers. (d) Friction as a function of normal force ( $F_{\text{tip}}$ - $F_f$ ). (a-d) are adapted from the reference [105] with permission.

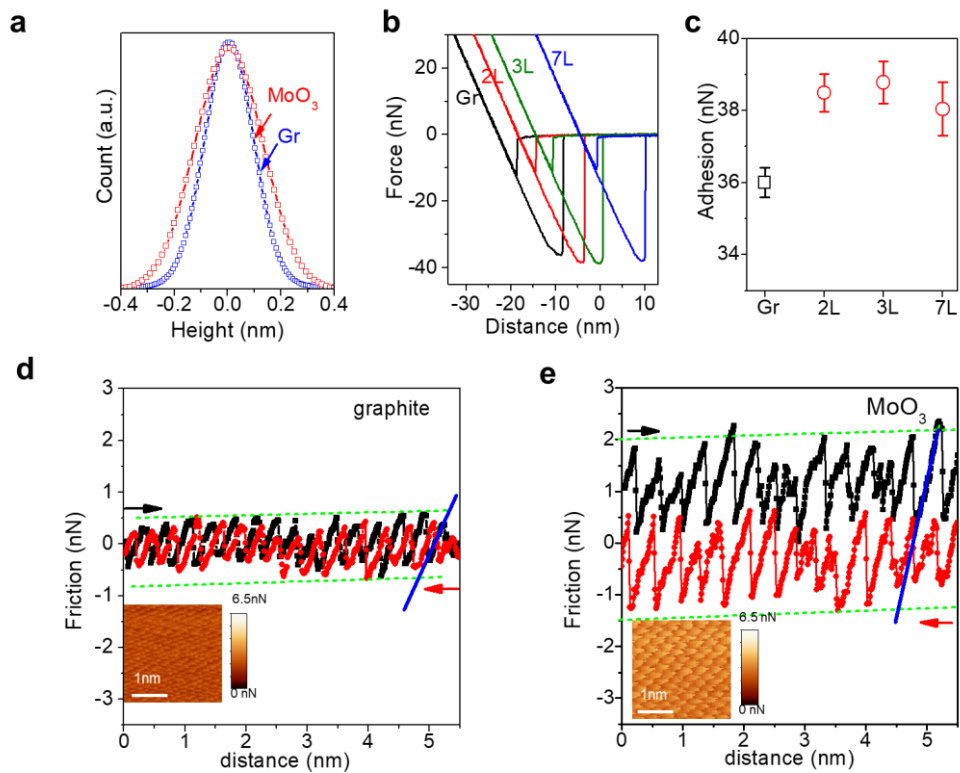


**Figure 3.4.** (a) Roughness of  $\alpha$ -MoO<sub>3</sub> and graphite. (b)  $F$ - $D$  curves of  $\alpha$ -MoO<sub>3</sub> and graphite. (c) Adhesion of the  $\alpha$ -MoO<sub>3</sub> and graphite calculated from (b). Lattice-scale friction loops of (d) graphite and (e) 2L  $\alpha$ -MoO<sub>3</sub>. The insets of (d) and (e) show the corresponding lattice-scale friction images. (a-e) are adapted from the reference [105] with permission.



### 3.3.4. Dielectric properties of $\alpha$ -MoO<sub>3</sub>

To evaluate the insulating properties of epitaxially-grown  $\alpha$ -MoO<sub>3</sub> nanosheets for their potential use as ultrathin dielectrics, current measurements were conducted by using c-AFM. Simultaneous topography and current maps were obtained for  $\alpha$ -MoO<sub>3</sub> nanosheets grown on graphite, with a sample bias  $V_s = 0.5$  V and a loading force of 2 nN, as shown in Figs. 3.5a and b. The completely linear  $I$ - $V$  result on graphite area without  $\alpha$ -MoO<sub>3</sub> demonstrates that contact resistance between tip and graphite is negligible. Contrary to graphite, the thinnest  $\alpha$ -MoO<sub>3</sub> nanosheet with 2L thickness exhibited an extremely low current, indicating that the  $\alpha$ -MoO<sub>3</sub> nanosheets are uniformly insulating and free of pinholes. The  $I$ - $V$  curves on  $\alpha$ -MoO<sub>3</sub> with various thicknesses were evaluated as shown in Fig. 3.5c. The  $dI/dV$  curves revealed significant current gaps for the 2L and 3L  $\alpha$ -MoO<sub>3</sub> nanosheets, with values of 1.6 V and 2.8 V, respectively (Fig. 3.5d). Furthermore, negligible current was observed across the 7L  $\alpha$ -MoO<sub>3</sub> nanosheet for the entire voltage sweep range, exhibiting completely insulating characteristics. The asymmetric  $I$ - $V$  curves can be attributed to the gradient in the concentration of oxygen vacancy [105].

The energy barrier for tunneling can be calculated by using Fowler–Nordheim tunneling as described by following equation [114]:

$$I(V) = \frac{A_{eff} q^3 m_e}{8\pi h \Phi_B t^2 m_{eff}} V^2 \exp \left[ -\frac{8\pi\sqrt{2m^*}\Phi_B^{3/2}t}{3hqV} \right] \dots\dots\dots \text{equation (3.3)}$$

where  $A_{eff}$ ,  $q$ ,  $m_e$ ,  $m_{eff}$ ,  $h$ ,  $t$ , and  $\Phi_B$  denote the effective tip area, electron charge, the mass of the rest electron, effective mass of electron, Planck constant, thickness, and the height of energy barrier, respectively [105]. The ratio between the effective mass of electron to mass of the rest electron ( $m_{eff}/m_e$ ) is 0.45 [116]. The equation (3.3) can be represented in logarithm expression:

$$\ln \frac{I(V)}{V^2} = \ln \frac{A_{eff} q^3 m_e}{8\pi h \Phi_B t^2 m_{eff}} - \frac{8\pi \sqrt{2m^*} \Phi_B^{\frac{3}{2}} t}{3h q V} \dots \dots \dots equation (3.4)$$

The  $\ln(I/V^2)$  versus  $1/V$  was plotted for 2L and 3L  $\alpha$ -MoO<sub>3</sub> (Fig. 3.5e). The energy barriers can be estimated by linear fitting the equation (3.4), and those for 2L and 3L  $\alpha$ -MoO<sub>3</sub> were 1.42 eV and 1.52 eV, respectively. In consideration of band gap of  $\alpha$ -MoO<sub>3</sub> (~3 eV), this value is almost half of the band gap size. The noise in the result can be attributed to tip contamination or water absorption [117, 118]. In addition, the dielectric breakdown strength of  $\alpha$ -MoO<sub>3</sub> was calculated to be 14 MV cm<sup>-1</sup>. Since this result is larger than that of hBN (8 MV cm<sup>-1</sup>) and bulk  $\alpha$ -MoO<sub>3</sub> (3 MV cm<sup>-1</sup>), ultrathin  $\alpha$ -MoO<sub>3</sub> has potential to be applied as an ultrathin gate dielectric [117, 119].

In addition, dielectric constant of  $\alpha$ -MoO<sub>3</sub> ( $\epsilon_r$ ) was evaluated by *F-D* spectroscopy with a DC-biased KPFM tip (Fig. 3.6). After positioning the conductive tip over the  $\alpha$ -MoO<sub>3</sub> surface at a distance of  $z_0$ , the tip was biased with DC voltage of  $V_{tip}$ . As a result, the tip relocated to a new position of  $z$ . The capacitive force exerted on the tip ( $F(z)$ ) is defined as follow [120]:

$$F(z) = -\frac{\partial C_{ts}}{\partial z} (V_{tip} - V_s)^2 + F_o \dots \dots \dots equation (3.5)$$

where  $F_o$ ,  $V_s$ , and  $C_{ts}$  are the force exerted on the macroscopic tip body, surface potential, and capacitance between tip and sample, respectively [105]. The capacitances ( $C_{ts}$ ) for metal and dielectric surfaces can be estimated by [121, 122]:

$$C_{ts,metal} = 2\pi\epsilon_0 \ln \left( 1 + \frac{R(1-\sin\theta)}{z} \right) \dots \dots \dots equation (3.6a) \text{ for metal}$$

$$C_{ts,dielectric} = 2\pi\epsilon_0 \ln \left( 1 + \frac{R(1-\sin\theta)}{z+h/\epsilon_r} \right) \dots \dots \dots equation (3.6b) \text{ for dielectric}$$

where  $z$ ,  $R$ ,  $h$  and  $\theta$  are the distance between tip and sample, the radius of the tip, the thickness of dielectrics, and the cone angle of tip apex, respectively [105]. By combining the equations (3.6a) and (3.6b) with the equation (3.5), the capacitive force applied on the tip can be expressed:

$$F(z)_{metal} = -\frac{2\pi\epsilon_0 R^2(1-\sin\theta)}{z(z+R(1-\sin\theta))} + F_o \dots\dots\dots equation (3.7a)$$

for metal

$$F(z)_{dielectric} = -\frac{2\pi\epsilon_0 R^2(1-\sin\theta)}{\left(z+\frac{h}{\epsilon_r}\right)\left(z+\frac{h}{\epsilon_r}+R(1-\sin\theta)\right)} + F_o \dots\dots\dots equation (3.7b)$$

for dielectric, respectively.

The tip radius was firstly determined to be 29 nm by performing DC-biased  $F$ - $D$  spectroscopy on the graphite exposed region. Next, the dielectric constant of ultrathin  $\alpha$ -MoO<sub>3</sub> was measured by the identical  $F$ - $D$  spectroscopy on the  $\alpha$ -MoO<sub>3</sub> covered regions. The dielectric constant of 2L  $\alpha$ -MoO<sub>3</sub> was calculated to be 6, and 3L and 7L  $\alpha$ -MoO<sub>3</sub> exhibit higher values with 10.5 and 11, respectively. These results coincide with the bulk  $\alpha$ -MoO<sub>3</sub> [89, 97-99]. Unlike conventional dielectric materials such as HfO<sub>2</sub> and Al<sub>2</sub>O<sub>3</sub>, of which properties are rapidly degraded for below 5 nm,  $\alpha$ -MoO<sub>3</sub> shows a high dielectric constant, absence of leakage current, and pinhole-less surface. These characteristics make  $\alpha$ -MoO<sub>3</sub> nanosheet a candidate for ultrathin dielectric layer.

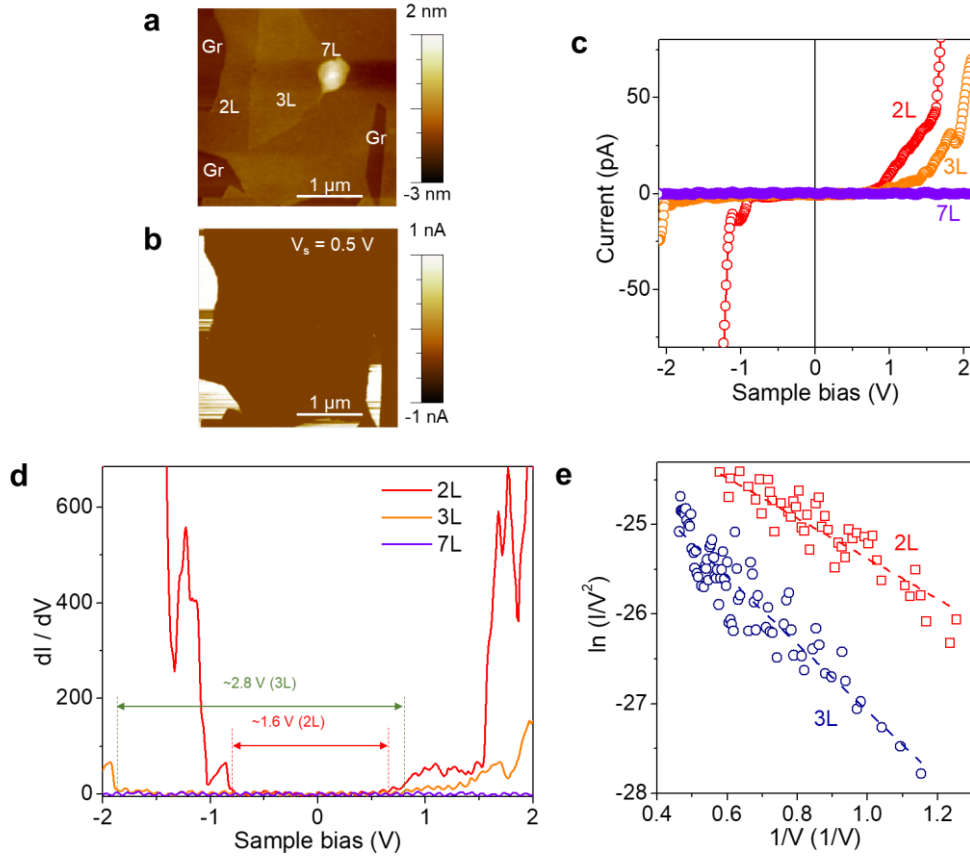


**Figure 3.5.** (a) Morphology and (b) current images of  $\alpha$ -MoO<sub>3</sub> on graphite. The current was measured at the sample bias of 0.5 V. (c) Tunneling current of  $\alpha$ -MoO<sub>3</sub> as a function of tip bias. (d)  $dI/dV$  curves and (e)  $\ln(I/V^2)$  versus  $1/V$  curves of 2L, 3L, and 7L  $\alpha$ -MoO<sub>3</sub>. The dashed lines are fitted results based on the equation (3.4). (a-e) are adapted from the reference [105] with permission.

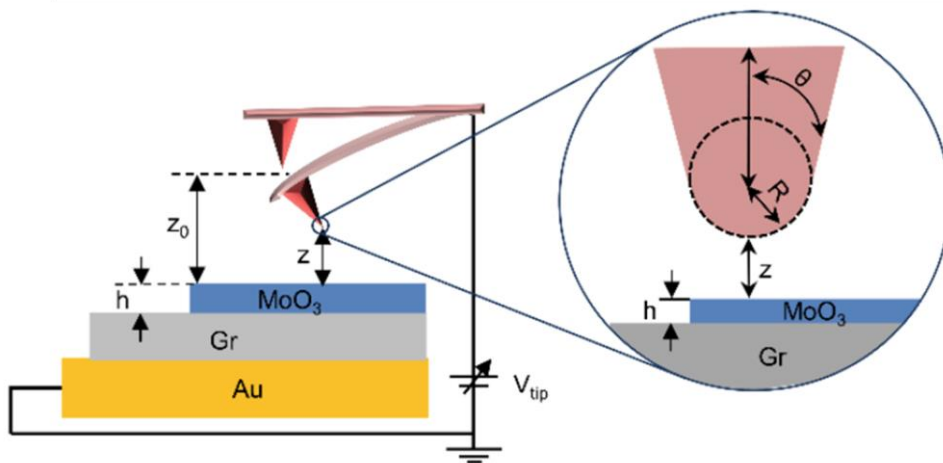


**Figure 3.6.** Schematic image of DC-biased *F-D* spectroscopy. Adapted from the reference [105] with permission.

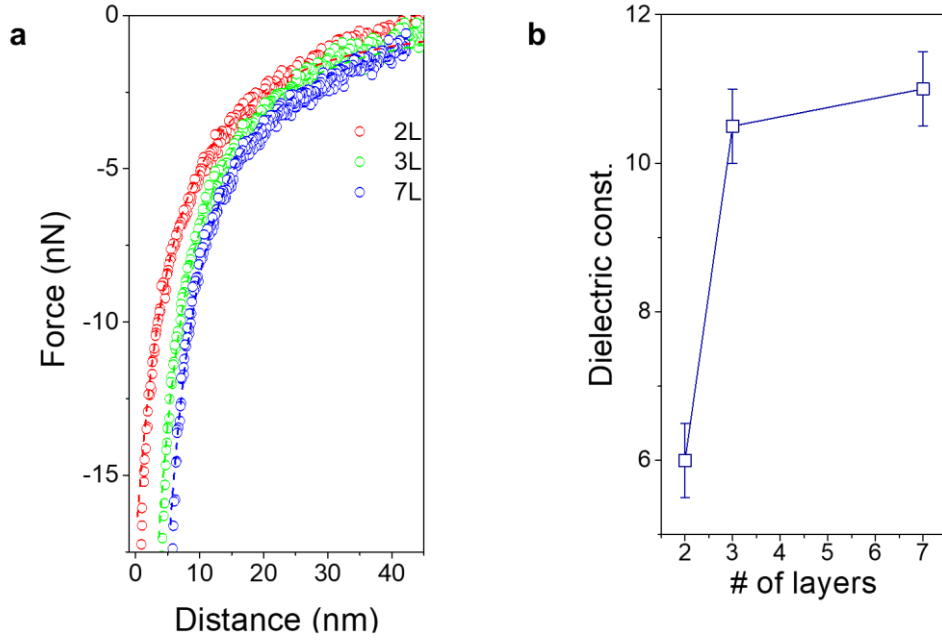


**Figure 3.7.** (a)  $F$ - $D$  curves of  $\alpha$ - $\text{MoO}_3$  with different thicknesses at a tip bias of 9 V. The dashed lines indicate the fitting results for 2L, 3L, and 7L  $\alpha$ - $\text{MoO}_3$  by the equation 3.7b. The inset shows the relation between the calculated dielectric constants and  $\alpha$ - $\text{MoO}_3$  thickness. (a) and (b) are adapted from the reference [105] with permission.

### 3.3.5. Surface potential of $\alpha$ -MoO<sub>3</sub>

The surface potential of  $\alpha$ -MoO<sub>3</sub> nanosheets grown on graphene was evaluated using KPFM, as shown in Fig. 3.8a. The topography and CPD images depicted in Figs. 3.8a and b clearly demonstrate noticeable variations in surface potential between  $\alpha$ -MoO<sub>3</sub> and graphene regions. In a mode where the bias of the tip is changed, the measured CPD can be expressed as

$$\text{CPD} = \frac{\phi_{\text{tip}} - \phi_{\text{sample}}}{e} \dots \dots \dots \text{equation (3.8)}$$

, where  $\phi_{\text{tip}}$  and  $\phi_{\text{sample}}$  sample represent the work functions of the tip and sample, respectively, while  $e$  is the elementary charge. Consequently, a higher CPD value (brighter region in Fig. 3.8b) indicates a lower work function. The profiles of height and CPD along the dashed lines in Figs. 3.8a and b are presented in Fig. 3.8c. It is evident that  $\alpha$ -MoO<sub>3</sub> exhibits lower CPD values than graphene by 140 mV. Interestingly, 2L and 4L  $\alpha$ -MoO<sub>3</sub> exhibited similar CPD values. The  $\phi_{\text{tip}}$  was calibrated on a reference graphene sample ( $\phi_{\text{gr}} = 4.6$  eV). The work function of the HOPG substrate without  $\alpha$ -MoO<sub>3</sub> was estimated as 4.61 eV, closely similar to that of pristine graphene. This result indicates that the intrinsic electrical properties of the HOPG surface are preserved after the growth of  $\alpha$ -MoO<sub>3</sub>, corroborating the Raman and FFM results that the graphene surface remains intact during the  $\alpha$ -MoO<sub>3</sub> growth process. Furthermore, when  $\alpha$ -MoO<sub>3</sub> nanosheets with varying numbers of layers were examined, it was observed that  $\alpha$ -MoO<sub>3</sub> consistently displayed a uniform work function of 4.73 eV for all measured thicknesses, as shown in Fig. 3.8d. These results are distinctive from other 2D materials such as graphene and MoS<sub>2</sub>, which exhibit thickness-dependent work functions [123, 124].

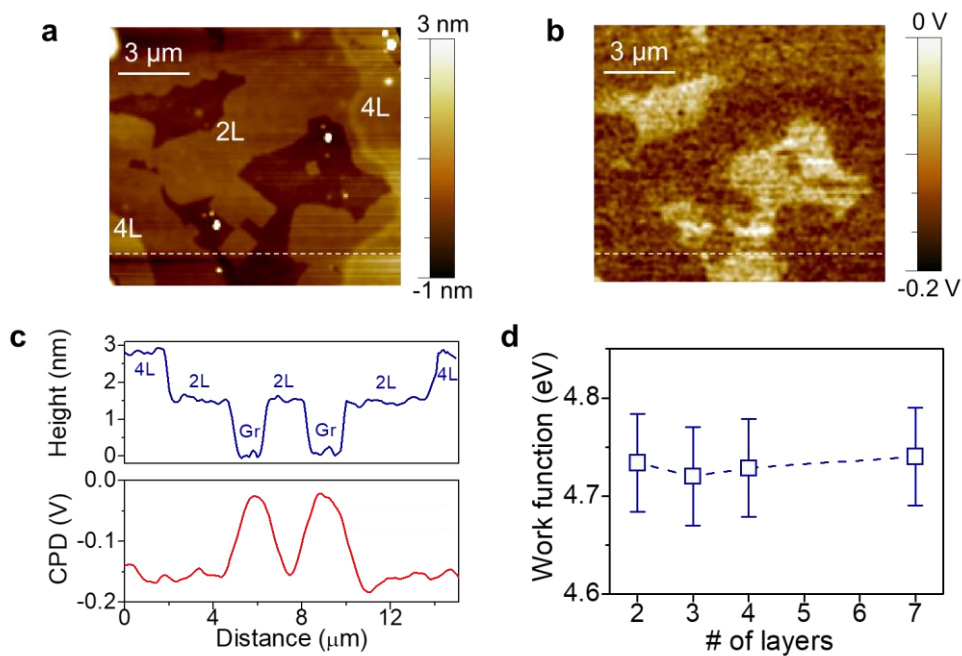


**Figure 3.7.** (a) Morphology and (b) CPD images of 2L and 4L  $\alpha$ -MoO<sub>3</sub> nanosheets grown in graphite. (c) Profiles of height and CPD obtained along the white dashed lines in (a) and (b). (d) Work functions calculated from CPDs of  $\alpha$ -MoO<sub>3</sub> nanosheets. (a-d) are adapted from the reference [105] with permission.



### 3.4. Conclusion

In conclusion, comprehensive studies based on AFM revealed that the tribological and electrical of  $\alpha$ -MoO<sub>3</sub> nanosheets are preserved even for few-layered thicknesses. In addition, the properties exhibit thickness-insensitivity in comparison with other 2D materials. The peculiar crystal structure of  $\alpha$ -MoO<sub>3</sub> increases lateral stiffness, which in turn results in high friction with thickness-insensitivity. Furthermore, work function and dielectric constant do not have thickness dependence. These results demonstrate that crystal and electronic structures of  $\alpha$ -MoO<sub>3</sub> are not severely affected by adjacent layers.

# **Chapter 4. In-plane Anisotropy of Graphene by Strong Interlayer Interactions with van der Waals Epitaxially Grown $\text{MoO}_3$ <sup>3</sup>**

## **4.1. Introduction**

In Chapter 2 and 3, the vdW epitaxial growth of  $\alpha\text{-MoO}_3$  and its properties have been investigated. The vdW epitaxy offers significant advantages due to the absence of dangling bonds at the interface and the relatively weak vdW interactions between the growth templates and epitaxial layers [125]. These characteristics facilitate the growth of epilayers with substantial lattice [126] and symmetry [127-129] mismatches, without inducing significant interfacial strain or misfit dislocations. In the context of symmetry mismatch, interlayer interaction plays a crucial role in vdW epitaxy, as it leads to the formation of anisotropic superlattices [41, 42, 130, 131] and the occurrence of directional strain during the cooling process [132].

I present the observation of in-plane anisotropy in graphene, which is induced by the robust interlayer interaction with vdW epitaxially grown  $\alpha\text{-MoO}_3$ . The strong interlayer interaction at the vdW interface plays a crucial role in modifying the mechanical and electrical properties of monolayer graphene. Due to the distinct TECs of the epilayer and graphene template, graphene is highly compressed up to -0.6% as the thickness of  $\alpha\text{-MoO}_3$  increases. Additionally, regardless of the  $\alpha\text{-MoO}_3$  thickness, charge transfer from  $\alpha\text{-MoO}_3$  results in high p-doping of graphene ( $p =$

---

<sup>3</sup> The content of this Chapter is derived from a paper published in the *Sci. Adv.* **9**, eadg6696 (2023). The manuscript and figures in this Chapter have been reproduced with permission from American Association for the Advancement of Science (AAAS) and the coauthors involved.

$1.94 \times 10^{13} \text{ cm}^{-2}$ ). Interestingly, the graphene deposited with  $\alpha\text{-MoO}_3$  exhibits in-plane anisotropy in electrical conductance (conductance ratio of 1.43) due to the periodic potentials induced by the crystal orientation of  $\alpha\text{-MoO}_3$ . Remarkably, the outstanding hole mobility of  $8,155 \text{ cm}^2 \text{ V}^{-1} \text{ s}^{-1}$  is maintained in  $\alpha\text{-MoO}_3$ -deposited graphene. This study demonstrates that the vdW epitaxial interface can facilitate strong interlayer interaction and induce in-plane anisotropy, providing a means to engineer the symmetry of 2D materials.

## 4.2. Methods

**Sample preparation.** A  $\alpha$ -MoO<sub>3</sub>/graphene heterostructure was prepared using a similar method used in the previous Chapters. As a Mo source, 100 nm-thick Mo was deposited on a SiO<sub>2</sub> (285 nm)/Si substrate using a DC magnetron sputter or an e-beam evaporator. The quality and morphology of  $\alpha$ -MoO<sub>3</sub> did not show any difference regardless of the deposition method. Graphene-exfoliated SiO<sub>2</sub>/Si substrate was used as a target substrate. Only monolayer graphene flakes were selected and utilized as target templates after their thicknesses were identified using Raman spectroscopy. To synthesize  $\alpha$ -MoO<sub>3</sub> on monolayer graphene, the Mo film was placed on a preheated hot plate (~525 °C), and the target substrate was placed 0.5 mm above the Mo film. The MoO<sub>x</sub> was sublimated from the Mo film and condensed on the target substrate. After 10 minutes, the target substrate was immediately removed from the heater.

**Raman spectroscopy.** Raman spectra were obtained by a Raman spectroscope (Renishaw Raman, inVia Reflex Confocal Raman Microscope, 532 nm, 600 gratings). Angle-resolved polarized Raman results were measured by using a home-built confocal micro-Raman system with excitation sources of the 532 nm (2.33 eV) line from a diode-pumped-solid-state laser. The incident (scattered) beam was focused (collected) onto (from) the sample through an objective lens with 0.8 NA, and 50 $\times$ , t (backscattering geometry). A Jobin–Yvon HORIBA iHR550 spectrometer (2400 grooves per mm) was used to disperse the Raman signal, which was detected by a liquid-nitrogen-cooled back-illuminated charge-coupled device (CCD) detector. The laser power was kept below 0.1 mW. The angle of polarizer was fixed at specific angle ( $\theta_{in}$ ), and specific polarization of the scattered light was selected by rotating the analyzer angle ( $\theta_{out}$ ). The polarization direction with respect to the groove direction of the grating of the signal entering the spectrometer kept constant by

placing and achromatic half-wave plate in front of the spectrometer.

**Transmission electron microscopy.** To fabricate TEM samples, poly (methyl methacrylate) (PMMA)-based wet transfer method was adopted. PMMA was deposited by spin-coating on the SiO<sub>2</sub>/Si substrate where  $\alpha$ -MoO<sub>3</sub>/Gr was located. Next, the substrate was immersed in a 2 wt% KOH solution after scraping the edges of the substrate. By etching SiO<sub>2</sub> with KOH, the PMMA/MoO<sub>3</sub>/Gr film was delaminated from the substrate. The film was cleaned with deionized water and transferred onto a TEM grid (Au mesh with holey carbon membrane). The remaining PMMA was removed by acetone. HR-TEM images were captured using a spherical aberration-corrected TEM (JEOL JEM-ARM 200F Cs-corrected TEM).

**Atomic force microscopy.** A commercial AFM system (NX-10, Park Systems) was used to obtain AFM images. Considering the status of the samples, the morphology of the sample was measured by contact or tapping modes.

**Device fabrication and electrical characterization.** E-beam lithography was used to define the region for source and drain metals around the  $\alpha$ -MoO<sub>3</sub>/Gr. The Cr/Pd/Au (2 nm/30 nm/40 nm) was deposited on the patterned substrates by using an e-beam evaporator. The electrical properties of the devices were measured using a parameter analyzer (Keithley 4200) in the ambient conditions. The field-effect mobility ( $\mu_{FE}$ ) of the devices was estimated by following equation:

$$\mu_{FE} = g_m \frac{L}{WV_{DS}C} \quad \text{equation (4.1)}$$

where  $g_m = dI_{DS}/dV_G$  is the transconductance,  $L$  and  $W$  are the channel length and width,  $V_{DS}$  is the drain voltage, and  $C$  is the unit capacitance of back gate 285 nm SiO<sub>2</sub>, respectively. The hole concentration ( $p$ ) was calculated using the equation:

$$p = \frac{\epsilon_0 \epsilon_r V_{CNP}}{e t_{ox}} \quad \text{equation (4.2)}$$

, where  $\epsilon_0$ ,  $\epsilon_r$ ,  $V_{CNP}$ ,  $e$ , and  $t_{ox}$  are the vacuum permittivity, relative permittivity of SiO<sub>2</sub>, charge neutrality point of the  $\alpha$ -MoO<sub>3</sub>/Gr device, elemental charge, and thickness of SiO<sub>2</sub>, respectively.

**DFT calculations.** To investigate the electronic and transport properties of the  $\alpha$ -MoO<sub>3</sub>/graphene heterostructure, first-principles calculations based on DFT were performed [133, 134] using the VASP code [135, 136]. Projector-augmented wave potentials [137, 138] were used to describe the valence electrons. The cutoff energy for the plane wave basis was set to 450 eV, and atomic relaxation was performed until the Hellmann–Feynman force acting on every atom decreased below 0.01 eV/Å. Dipole correction was included to obtain more precise calculation. For the exchange-correlation function, the rev-vdW-DF2 method [139] was adopted to include vdW interactions. The Brillouin zone (BZ) was sampled using a 2×8×1  $k$ -grid for the rectangular superlattice of  $\alpha$ -MoO<sub>3</sub>/graphene heterostructure. A vacuum region of ~15 Å was introduced to avoid interlayer interaction along the out-of-plane direction.

## 4.3. Results and Discussion

### 4.3.1. Crystal structure of $\alpha$ -MoO<sub>3</sub>/graphene heterostructure

To explore the interlayer interaction at the interface composed with in-plane anisotropic 2D materials, I employed  $\alpha$ -MoO<sub>3</sub> as a building block [54, 60, 61, 67, 140]. The  $\alpha$ -MoO<sub>3</sub> was grown on exfoliated graphene by the identical methods as suggested in the previous Chapters. Figure 4.1a shows the monolayer graphene covered with  $\alpha$ -MoO<sub>3</sub> ( $\alpha$ -MoO<sub>3</sub>/Gr). In Fig. 4.1b, the Raman results of the as-exfoliated graphene and  $\alpha$ -MoO<sub>3</sub>/Gr samples are presented. The main Raman peaks of  $\alpha$ -MoO<sub>3</sub> were observable which are located at approximately 817 cm<sup>-1</sup> and 995 cm<sup>-1</sup> [62, 78]. The absence of the D peak, which indicates defects in graphene, suggests that there was no notable damage to graphene during the growth process [141, 142]. However, the G and 2D peaks exhibited dramatic shifts after the deposition of  $\alpha$ -MoO<sub>3</sub>. This observation indicates that the deposited  $\alpha$ -MoO<sub>3</sub> affects underlying graphene both mechanically and electrically, because the positions of G and 2D peaks are extremely sensitive to the strain and doping. The detailed discussion of the shift of these peaks will be provided later in the paper. By using AFM, the morphology and thickness of  $\alpha$ -MoO<sub>3</sub> were characterized as shown in Figs. 4.1c and d. The graphene surface was fully covered by bilayer  $\alpha$ -MoO<sub>3</sub> (referred to as 2L  $\alpha$ -MoO<sub>3</sub>) with a few thicker islands, consistent with the previous Chapters. The  $\alpha$ -MoO<sub>3</sub> surface appeared clean and flat, without any signs of contamination or damage. The height profile in Fig. 4.1d (taken from the white dashed line in Fig. 4.1c) demonstrates that the thickness of the monolayer  $\alpha$ -MoO<sub>3</sub> corresponds to approximately half of the unit cell (~0.7 nm) [52, 60, 67, 143, 144].

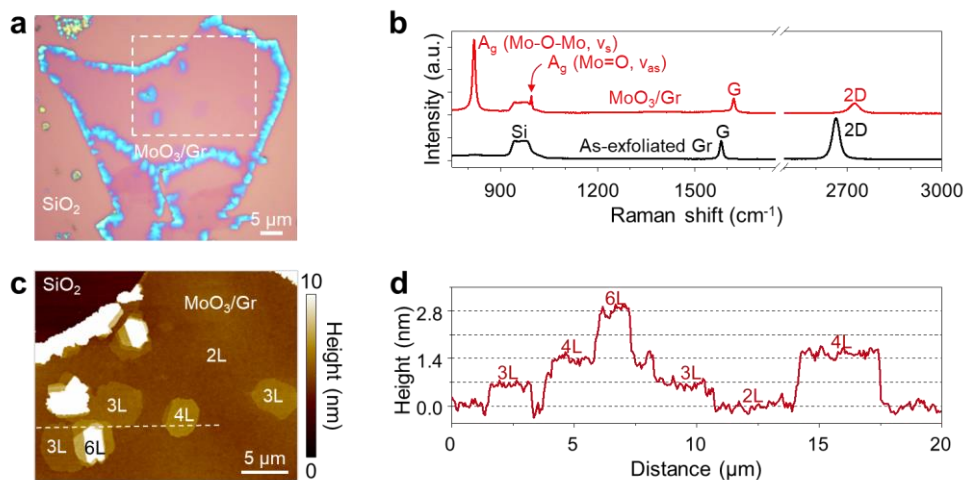


**Figure 4.1.** vdW epitaxial growth of  $\alpha$ -MoO<sub>3</sub> on monolayer graphene. (a) Optical microscope image of  $\alpha$ -MoO<sub>3</sub>/Gr. (b) Raman spectra of as-exfoliated Gr (black) and  $\alpha$ -MoO<sub>3</sub>/Gr (red). (c) AFM image of  $\alpha$ -MoO<sub>3</sub>/Gr of the dashed area in Fig. 1a. (d) AFM height profile along the white dashed line in Fig. 1c. (a-d) are adapted from the reference [145] with permission.



#### 4.3.2. Epitaxial relationship between $\alpha$ -MoO<sub>3</sub> and graphene

To analyze the crystal structures and epitaxial relationship between  $\alpha$ -MoO<sub>3</sub> and Gr, Cs-TEM was employed. Figure 4.2a displays a TEM image of  $\alpha$ -MoO<sub>3</sub>/Gr where 2L  $\alpha$ -MoO<sub>3</sub> is partially covering the graphene. The epitaxial growth of crystalline  $\alpha$ -MoO<sub>3</sub> on graphene is confirmed by the high-resolution TEM image shown in Fig. 4.2b. The diffraction pattern obtained by Fast Fourier Transform (FFT), depicted in the inset of Fig. 4.2b, verifies the alignment of the rhombic pattern (blue dashed line) of  $\alpha$ -MoO<sub>3</sub> with the hexagonal pattern (orange dashed line) of graphene. Specifically, the (200) plane of  $\alpha$ -MoO<sub>3</sub> is parallel to the (1 $\bar{1}$ 00) plane of graphene [146, 147]. By filtering the TEM images of graphene (left) and  $\alpha$ -MoO<sub>3</sub> (right) using FFT, as shown in Fig. 4.2c, the growth of rectangular  $\alpha$ -MoO<sub>3</sub> with unit lattice parameters of 3.97 (*a*) and 3.75 Å (*c*-axis) on graphene is clearly observed. The epitaxial relationship reveals that the *a*- and *c*-axes of  $\alpha$ -MoO<sub>3</sub> are aligned with the armchair (*ac*) and zigzag (*zz*) edges of graphene, respectively. Figure 4.2d presents an atomic model illustrating a superlattices (yellow dashed lines) in the  $\alpha$ -MoO<sub>3</sub>/Gr heterostructure. The rectangular superlattice in  $\alpha$ -MoO<sub>3</sub>/Gr leads to distinct periodicities along the *ac* and *zz* directions in graphene [41, 42, 130, 131].

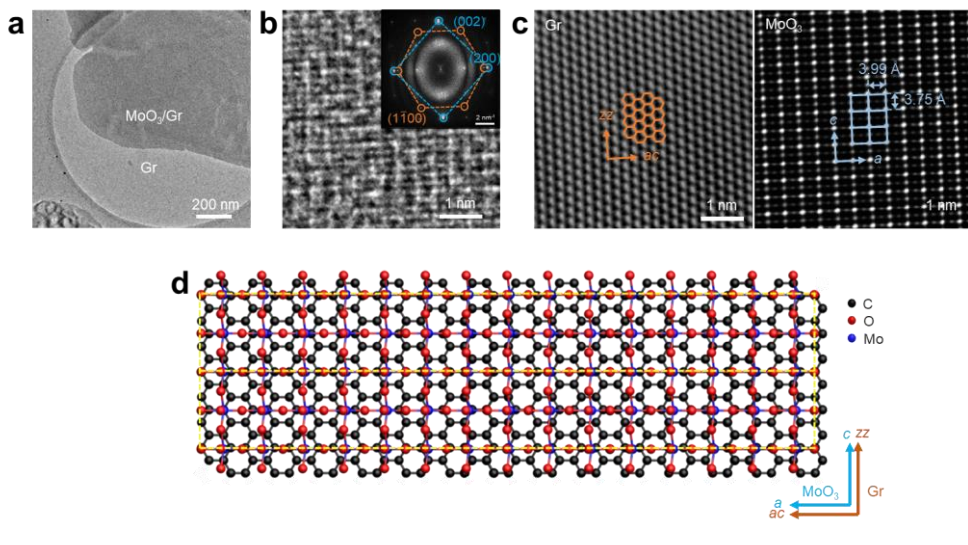


**Figure 4.2.** Epitaxial relationship between  $\alpha$ - $\text{MoO}_3$  epilayers and monolayer graphene growth template. (a) Low-magnification TEM image of  $\alpha$ - $\text{MoO}_3/\text{Gr}$ . (b) High-resolution TEM image of  $\alpha$ - $\text{MoO}_3/\text{Gr}$ . The inset shows the corresponding FFT image. Only a single set of rhombus pattern indicates the growth of single-crystal  $\alpha$ - $\text{MoO}_3$  (blue). In addition, the perfect alignment of  $\alpha$ - $\text{MoO}_3$  and graphene (orange) patterns demonstrates the epitaxial growth of  $\alpha$ - $\text{MoO}_3$  on monolayer graphene. (c) FFT-filtered images of graphene (left) and  $\alpha$ - $\text{MoO}_3$  (right). (d) Schematic of  $\alpha$ - $\text{MoO}_3/\text{Gr}$  superlattices (yellow dashed boxes) based on their epitaxial relationship. (a-d) are adapted from the reference [145] with permission.

### 4.3.3. Modulation of doping and strain in graphene by $\alpha$ -MoO<sub>3</sub> epilayer

To examine the interlayer interaction between  $\alpha$ -MoO<sub>3</sub> and graphene, I conducted Raman spectroscopy measurements on several regions of graphene covered by  $\alpha$ -MoO<sub>3</sub> islands with different thicknesses (1–5L), as depicted in Fig. 4.3a. The Raman spectra of the as-exfoliated graphene (gray) and the uncovered graphene (black) are also presented in Fig. 4.3a for comparison. The uncovered graphene region refers to the area where no  $\alpha$ -MoO<sub>3</sub> was deposited after the epitaxial growth. G and 2D peaks were slightly blue-shifted due to the annealing effect [148]. In contrast, G and 2D peaks of the  $\alpha$ -MoO<sub>3</sub>/Gr heterostructure are greatly blue shifted compared to the as-exfoliated and uncovered graphene. Moreover, these two peaks experienced pronounced blue-shifts with increasing  $\alpha$ -MoO<sub>3</sub> thickness. The substantial shifts in the Raman peaks indicate a robust interlayer interaction between the  $\alpha$ -MoO<sub>3</sub> epilayers and graphene, resulting in significant doping and strain in graphene depending on the thickness of  $\alpha$ -MoO<sub>3</sub> [141, 142].

To analyze the doping concentration ( $p$ ) and strain ( $\epsilon$ ) of  $\alpha$ -MoO<sub>3</sub>/Gr separately, the positions of the G ( $\omega_G$ ) and 2D ( $\omega_{2D}$ ) was marked on the correlation plot (Fig. 4.3b). By projecting  $\omega_G$  and  $\omega_{2D}$  onto the doping concentration (magenta) and strain axes (gray), respectively [149], it was available to quantify the doping and strain of graphene. As shown in Fig. 4.3a, the uncovered graphene exhibited p-doping ( $p = 7.8 \times 10^{12} \text{ cm}^{-2}$ ) and minor compression of  $-0.07$  [148, 150, 151]. In contrast, the graphene in the  $\alpha$ -MoO<sub>3</sub>/Gr region demonstrated significant p-doping ( $p = 1.94 \times 10^{13} \text{ cm}^{-2}$ ) for all  $\alpha$ -MoO<sub>3</sub> thicknesses. Meanwhile the compressive strain increased for thicker  $\alpha$ -MoO<sub>3</sub> layers. The distinct dependence on  $\alpha$ -MoO<sub>3</sub> thickness regarding the doping concentration and strain is clearly visible in Figs. 4.3c–e. Despite the deposition of  $\alpha$ -MoO<sub>3</sub> layers with varying thicknesses on graphene, as depicted in the AFM image in Fig. 4.3c, the p-doping concentration of graphene, determined through the Raman peaks, remained consistent irrespective of

the number of  $\alpha$ -MoO<sub>3</sub> layers, as shown in Fig. 4.3d. On the other hand, thicker  $\alpha$ -MoO<sub>3</sub> epilayers induced higher compressive strain, as illustrated in Fig. 4.3e.

To provide a comprehensive visualization of the relationship between  $\alpha$ -MoO<sub>3</sub> thickness and the doping and strain effects on graphene, I have plotted the doping concentration and compressive strain as a function of  $\alpha$ -MoO<sub>3</sub> thickness in Figs. 4.3f and 4.3g, respectively. It is evident from Fig. 4.3f that the p-doping concentration of 1L  $\alpha$ -MoO<sub>3</sub>/Gr is approximately twice as high as that of the uncovered graphene, and this high doping concentration remains relatively constant across 1-5L  $\alpha$ -MoO<sub>3</sub> thicknesses. This observation suggests that a significant p-doping effect on graphene can be achieved using only a monolayer of  $\alpha$ -MoO<sub>3</sub>. The significant p-doping observed in 1L  $\alpha$ -MoO<sub>3</sub>/Gr can be attributed to the efficient charge transfer facilitated by the large and thickness-insensitive work function of  $\alpha$ -MoO<sub>3</sub> [51, 105, 152, 153]. Conversely, the compressive strain experienced by graphene in the  $\alpha$ -MoO<sub>3</sub>/Gr system exhibits a clear dependence on the  $\alpha$ -MoO<sub>3</sub> thickness (Fig. 4.3g). This strain arises from the mismatch in the TECs between  $\alpha$ -MoO<sub>3</sub> and graphene [60, 154, 155], as well as the high lateral stiffness and friction of  $\alpha$ -MoO<sub>3</sub> [105, 112, 113]. The strain in graphene increases with the addition of  $\alpha$ -MoO<sub>3</sub> layers, albeit with a diminishing incremental effect. This behavior can be attributed to the formation of a progressively rigid  $\alpha$ -MoO<sub>3</sub> structure as the thickness increases. Both the doping and strain effects observed in graphene upon the deposition of  $\alpha$ -MoO<sub>3</sub> demonstrate the existence of a strong interlayer interaction between  $\alpha$ -MoO<sub>3</sub> and graphene, characterized by their epitaxial relationship.

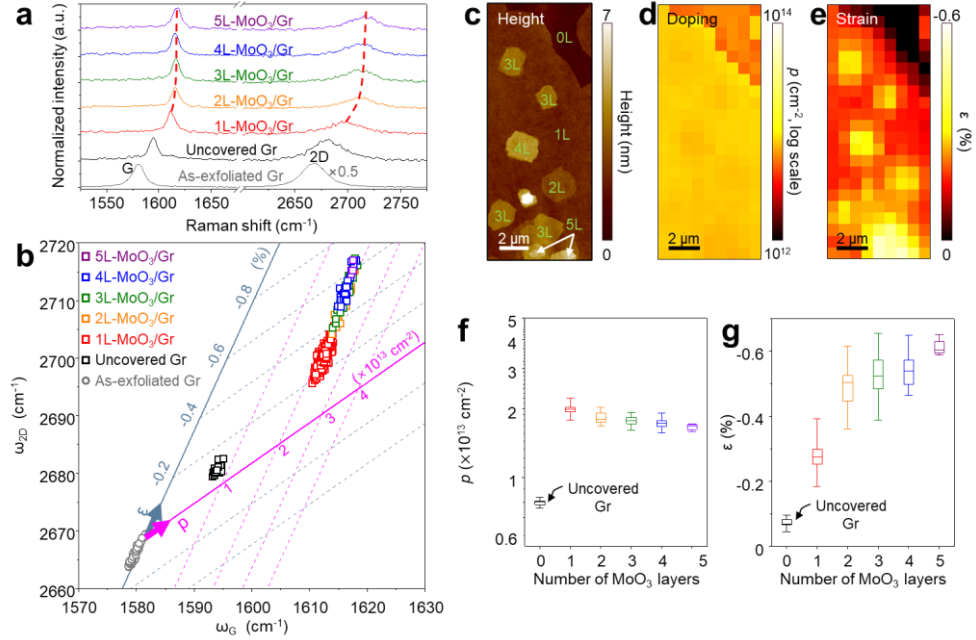


**Figure 4.3.** Hole concentration and strain in the  $\alpha$ -MoO<sub>3</sub>-grown graphene. (a) Raman spectra of the as-exfoliated Gr (gray), uncovered Gr (black), and  $\alpha$ -MoO<sub>3</sub>/Gr with various  $\alpha$ -MoO<sub>3</sub> thicknesses (rainbow-colored, red to purple with increasing  $\alpha$ -MoO<sub>3</sub> thickness). For  $\alpha$ -MoO<sub>3</sub>/Gr, the apexes of the G and 2D peaks are connected by dashed lines for visual guidance. (b), Correlation plot of the  $\omega_{2D}$ - $\omega_G$  for the samples shown in Fig. 3a. (c), AFM image of  $\alpha$ -MoO<sub>3</sub>/Gr with various  $\alpha$ -MoO<sub>3</sub> thicknesses. (d, e), mapping images of doping and strain of  $\alpha$ -MoO<sub>3</sub>/Gr, respectively. (f, g), Plots of hole concentration and strain as a function of the number of  $\alpha$ -MoO<sub>3</sub> layers. (a-g) are adapted from the reference [145] with permission.

#### 4.3.4. In-plane anisotropy of $\alpha$ -MoO<sub>3</sub>/Gr

To investigate the orientation-dependent structural modulation induced by the elongated superlattice and strong interlayer interaction at the  $\alpha$ -MoO<sub>3</sub>-Gr heterointerface, I conducted angle-resolved polarized Raman spectroscopy on  $\alpha$ -MoO<sub>3</sub>/Gr. This involved rotating an analyzer ( $\theta_{\text{out}}$ ) while keeping the polarizer fixed ( $\theta_{\text{in}}$ ). Figure. 4.4a illustrates the G peaks of 3L  $\alpha$ -MoO<sub>3</sub>/Gr measured at four specific angles. These G peaks were deconvoluted into two distinct peaks:  $G^+$  at  $1621.7 \text{ cm}^{-1}$  (red area) and  $G^-$  at  $1623.2 \text{ cm}^{-1}$  (blue area), respectively. The eigenvectors of these peaks are parallel and orthogonal to the strain direction, respectively [156-158]. The intensities of these peaks exhibit variations with  $\theta_{\text{out}}$ , leading to a periodic change of position of the convoluted G peak (Fig. 4.4b). The polar coordinates plot in Fig. 4.4c presents the intensities of  $G^+$  (red) and  $G^-$  (blue circles) peaks. Notably, these intensities demonstrate distinct  $\cos^2 \theta_{\text{out}}$  patterns, exhibiting repulsive behavior as predicted by theoretical expectations (solid lines in Fig. 4.4). This finding unequivocally confirms the uniaxial strain in graphene [156-158]. Therefore, the vdW epitaxially grown  $\alpha$ -MoO<sub>3</sub> induces a uniaxial strain in graphene [60, 132, 154, 155].

I conducted angle-resolved electrical transport measurements on the 1L  $\alpha$ -MoO<sub>3</sub>/Gr device to investigate the electrical anisotropy. The inset of Fig. 4.4d presents the device configuration with multiple electrodes of different angles deposited around the 1L  $\alpha$ -MoO<sub>3</sub> island. Figure. 4.4d displays the transfer curves ( $I_{\text{DS}}-V_{\text{G}}$ ) obtained from different electrodes at specific angles, revealing the highly p-doped nature of  $\alpha$ -MoO<sub>3</sub>/Gr, consistent with the Raman measurement. Moreover, in the transfer curve, both current and its slope exhibit strong dependence on the measured orientation. Figs. 4.4e-g depict the hole concentration at zero gate voltage, conductance ( $G$ ), and  $\mu_{\text{FE}}$  of  $\alpha$ -MoO<sub>3</sub>/Gr in polar coordinates. Notably, the doping level shows no orientation dependence, as it is primarily governed by the charge

transfer between  $\alpha$ -MoO<sub>3</sub> and graphene (Fig. 4.4e). In contrast, both conductance and  $\mu_{\text{FE}}$  exhibit anisotropy with 180° periodicity (Fig. 4.4f and g). The anisotropy conductance ratio ( $G_{\text{max}}/G_{\text{min}}$ ) reaches 1.43 at  $V_G = 0$  V, comparable to that of BP (~1.5) [16, 159, 160]. In addition,  $\mu_{\text{FE}}$  of  $\alpha$ -MoO<sub>3</sub>/Gr demonstrates a large anisotropy ratio ( $\mu_{\text{FE,max}}/\mu_{\text{FE,min}}$ ) of 1.77, while preserving outstanding mobility of 8,155 cm<sup>2</sup> V<sup>-1</sup> s<sup>-1</sup> at  $p = 1 \times 10^{12}$  cm<sup>-2</sup>. These observations demonstrate the induction of in-plane electrical anisotropy in graphene through the epitaxial growth of  $\alpha$ -MoO<sub>3</sub>.

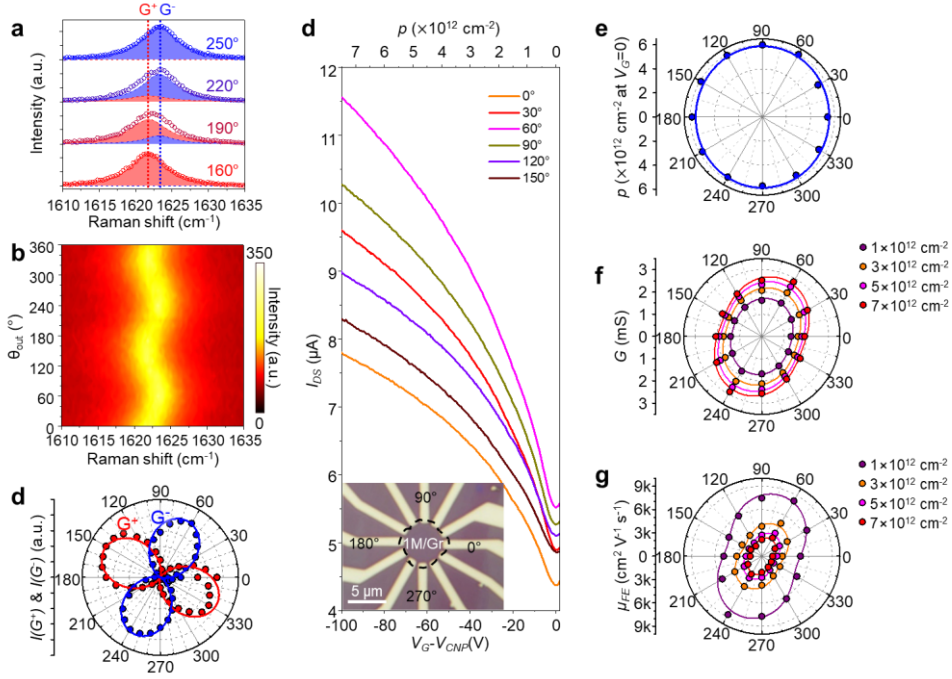


**Figure 4.4.** Anisotropy in graphene induced by  $\alpha$ -MoO<sub>3</sub> epilayers. (a) Fitting results of four representative angle-resolved polarized Raman spectra. The measured data are represented by the hollow circles, while the red and blue shaded areas correspond to the fitted results of the G<sup>+</sup> and G<sup>-</sup> peaks, respectively. The peak positions of G<sup>+</sup> and G<sup>-</sup> are indicated by the red and blue dotted lines, respectively. (b) Contour plot of the angle-resolved polarized Raman spectra of G peak as function of analyzer angle ( $\theta_{out}$ ). (c) Intensities of G<sup>+</sup> (red) and G<sup>-</sup> (blue) peaks plotted in the polar coordinate. Spheres correspond to the intensities, and solid lines correspond to the results fitted to the theoretical expectation (42, 43). (d), Orientation-dependent transfer characteristics of  $\alpha$ -MoO<sub>3</sub>/Gr electric device. The inset shows an optical image of the  $\alpha$ -MoO<sub>3</sub>/Gr electric device. (e, f, g) Polar coordinate plots of the hole concentration at zero-gate voltage (e), conductance (f), and field-effect mobility (g) of the  $\alpha$ -MoO<sub>3</sub>/Gr device in Fig. 4d, respectively. Conductance and field-effect mobility are measured under various carrier concentrations, which are represented with different colors. (a-g) are adapted from the reference [145] with permission.



#### 4.3.5 Anisotropic distortion of graphene band structure by $\alpha$ -MoO<sub>3</sub> epilayer

The origin of the anisotropy of  $\alpha$ -MoO<sub>3</sub>/Gr was revealed by first-principles calculations based on density functional theory (DFT). The band structure of graphene can be deformed by anisotropic periodic potentials [161, 162]. The elongated superlattice in  $\alpha$ -MoO<sub>3</sub>/Gr, as well as compressive strain, can result in out-of-plane deformation in monolayer graphene. By these factors, the synthesized  $\alpha$ -MoO<sub>3</sub> would generate the periodic potentials with anisotropy to graphene.

To confirm my hypothesis, I constructed a heterostructure of  $\alpha$ -MoO<sub>3</sub>/Gr under consideration of strain by TECs [60, 155]. In addition, the  $a$ -axis ( $c$ -axis) of  $\alpha$ -MoO<sub>3</sub> is parallel with the  $ac$  ( $zz$ ) directions of graphene, as observed in the TEM images in Fig. 4.2d. The graphene is compressed with 1.2 and 0.2% strain along the  $ac$  and  $zz$  directions by the  $\alpha$ -MoO<sub>3</sub> lattice, respectively. The out-of-plane corrugation of graphene is shown in Fig. 4.5a. In the superlattice (indicated by a black box), the graphene was deformed 0.09 Å along out-of-plane direction. The upward (downward) corrugation of the carbon atoms is represented with red (blue) color. Therefore, 1D-patterned corrugation parallel to the  $zz$  direction is exhibited in a graphene.

The 1D superlattice leads to periodic potentials on graphene. In the superlattice, the bands fold into small BZ of the supercell, thus the change of Dirac energy bands of graphene cannot be identified. To avoid this, dense energy bands in the supercell BZ was projected or unfolded into the original BZ of graphene [163-165]. Figure 4.5b illustrates the unfolded energy bands of the optimized  $\alpha$ -MoO<sub>3</sub>/graphene heterostructure (highlighted in fiery contour) projected onto the graphene layer, along two directions:  $x$  ( $ac$ ) and  $y$  ( $zz$ ), as depicted in Fig. 4.5a. The Fermi level ( $E_F$ , gray dashed lines) is shifted  $\sim 0.7$  eV below the Dirac point. For comparison, the band structures of the isolated graphene layer (represented by green dashed lines) were also shown. Note that the isolated graphene possesses the same compressive

strain as the  $\alpha$ -MoO<sub>3</sub>/graphene heterostructure. Notably, the presence of apparent gapful (gapless) Dirac points along the  $q_x$  ( $q_y$ ) direction in Fig. 4.5b can be attributed to the strain-induced shift of the Dirac point along the  $q_y$  direction. On the right side of Fig. 4.5b, the effective band structure along the y-axis undergoes significant alterations within certain energy ranges, while on the left side, along the x-axis, it closely resembles that of isolated graphene (indicated by white dashed boxes). Notably, there is noticeable band splitting around the Fermi level, indicating strong hybridization with the  $\alpha$ -MoO<sub>3</sub> layer. This directional electronic disparity depicted in Fig. 4.5b is estimated to induce anisotropy in the electrical transport properties of the  $\alpha$ -MoO<sub>3</sub>/graphene heterostructure.

By employing the Boltzmann transport equation under the assumption of a simple constant relaxation time ( $\tau$ ), I was able to estimate the conductivities ( $\sigma$ ) along the  $x$ - and  $y$ -axes based on the band structures [166]. The resulting expression for  $\sigma$  is as follows:

$$\sigma(\mu, T) = \frac{e^2 \tau}{8\pi^3} \int \int \sum_n \mathbf{v}_{n,\mathbf{k}} \otimes \mathbf{v}_{n,\mathbf{k}} \delta(\varepsilon - \varepsilon_{n,\mathbf{k}}) dk \left( -\frac{\partial f(\varepsilon, \mu, T)}{\partial \varepsilon} \right) d\varepsilon \quad \text{equation (4.3)}$$

where  $\mathbf{v}_{n,\mathbf{k}}$ ,  $\varepsilon_{n,\mathbf{k}}$ ,  $\tau$ , and  $f$  are the  $\mathbf{k}$ -dependent group velocity, energy of the  $n^{\text{th}}$  band, relaxation time (considered a constant for simplicity), and Fermi distribution function as functions of the energy ( $\varepsilon$ ), chemical potential ( $\mu$ ), and temperature ( $T$ ), respectively [145]. As depicted in Fig. 4.5c the electrical conductivities along the  $x$  and  $y$  axis show a notable difference, which aligns with my experimental findings.

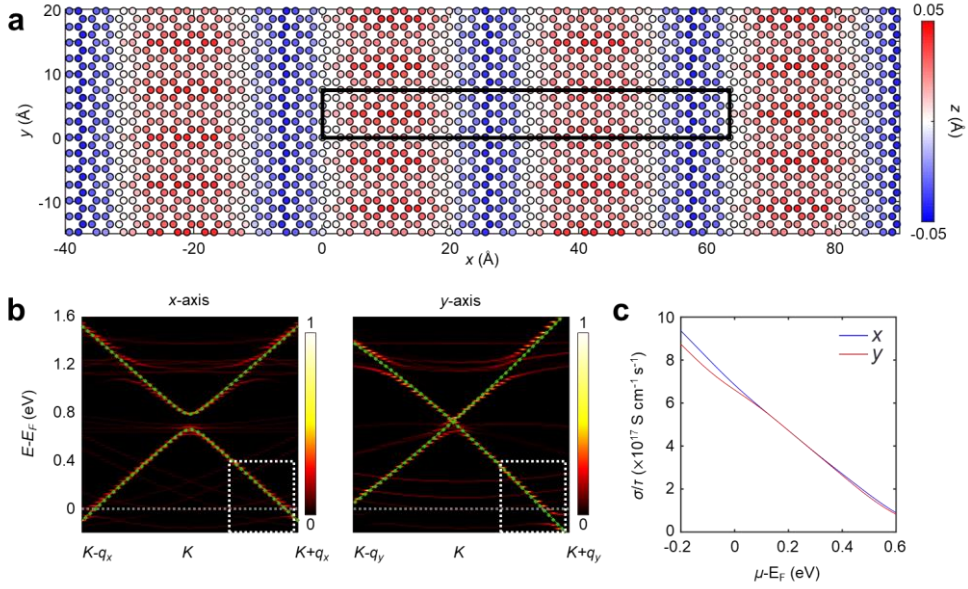


**Figure 4.5.** Anisotropic band distortion in  $\alpha$ -MoO<sub>3</sub>/Gr. (a) Out-of-plane deformation of graphene for optimized  $\alpha$ -MoO<sub>3</sub>/Gr heterostructure. Blue (red) color represents the displacement of carbon atoms below (above) the center of mass of the graphene layer. (b) Unfolded energy bands of the  $\alpha$ -MoO<sub>3</sub>/Gr heterostructure, projected onto the graphene layer, along the  $x$ -axis (left) and  $y$ -axis (right) in the vicinity of the  $K$  point. The gray dashed lines represent the Fermi level of  $\alpha$ -MoO<sub>3</sub>/Gr. The green dashed lines indicate the band structure of isolated graphene with the same compressive strain as that in the heterostructure, 1.2% along the  $ac$  direction and 0.2% along the  $zz$  direction. The color scale indicates the  $k$ -dependent spectral weight for the primitive BZ of the graphene layer. (c) Calculated in-plane electrical conductivities using the unfolded spectral functions projected on graphene at 300 K along the  $x$ - and  $y$ -axis. (a-c) are adapted from the reference [145] with permission.

## 4.4. Conclusion

To summarize, I conducted a comprehensive investigation into the interlayer interaction between  $\alpha$ -MoO<sub>3</sub> epilayers and monolayer graphene growth templates in symmetry-mismatched epitaxy. The results clearly demonstrated that the profound modulation of doping and strain in graphene was a direct result of the robust interlayer interaction with the  $\alpha$ -MoO<sub>3</sub> epilayers. Firstly, deposition of a single layer of  $\alpha$ -MoO<sub>3</sub> led to a significant enhancement in the hole concentration in graphene, comparable to other doping techniques involving the deposition of a charge-transfer layer on graphene [167, 168]. Moreover, by adjusting the thickness of the  $\alpha$ -MoO<sub>3</sub> epilayers, it was possible to control the strain exerted on graphene while maintaining a high hole concentration. Additionally, the directional deformation of the graphene band structure induced electrical conductance anisotropy in symmetrical graphene. In conclusion, this study demonstrates that the strong interlayer interaction between vdW epitaxially grown 2D oxides and 2D materials can serve as a viable approach for symmetry engineering of 2D materials, without compromising their exceptional electrical properties. These findings hold great promise for applications in optoelectronic devices that necessitate optical and electrical anisotropy.

## Chapter 5. Conclusion

In this dissertation, growth, characterization, and vdW heterostructures of  $\alpha$ -MoO<sub>3</sub> have been investigated.

In Chapter 2, I focused on the synthesis and characterization of  $\alpha$ -MoO<sub>3</sub> nanosheets on various 2D growth templates. The successful growth of monolayer to multilayer  $\alpha$ -MoO<sub>3</sub> nanosheets on 2D substrates was achieved, and a single-crystal  $\alpha$ -MoO<sub>3</sub> nanosheet without grain boundaries was obtained. The band gap of  $\alpha$ -MoO<sub>3</sub> increased with decreasing thickness, and the synthesized material exhibited high n-doping and a small work function. These results demonstrated the immense potential of ultra-thin  $\alpha$ -MoO<sub>3</sub> in 2D-material-based electronics.

In Chapter 3, the tribological and electrical properties of epitaxially grown single-crystal  $\alpha$ -MoO<sub>3</sub> nanosheets on graphite have been thoroughly examined. The study revealed the thickness-insensitivity of friction, work function, dielectric constant, and tunnel resistance in  $\alpha$ -MoO<sub>3</sub>. The thickness-insensitivity can be attributed to the weak interlayer coupling of  $\alpha$ -MoO<sub>3</sub>.

In Chapter 4, I explored the in-plane anisotropy and doping effects in graphene induced by vdW epitaxially grown  $\alpha$ -MoO<sub>3</sub> layers. It has been demonstrated that high p-doping of graphene and the compressive strain is induced in graphene by deposition of  $\alpha$ -MoO<sub>3</sub>. In addition, the asymmetrical band distortion in  $\alpha$ -MoO<sub>3</sub>-deposited graphene resulted in in-plane electrical anisotropy. This research presented a method to induce anisotropy in symmetric 2D materials through the formation of asymmetric superlattices.

Meanwhile, several further studies are required to fully expand the potential of  $\alpha$ -MoO<sub>3</sub> and related vdW heterostructures.

First, directional uniformity of  $\alpha$ -MoO<sub>3</sub> should be improved. Because of symmetry difference between orthorhombic  $\alpha$ -MoO<sub>3</sub> and conventional hexagonal 2D materials, the synthesized  $\alpha$ -MoO<sub>3</sub> have triply degenerated grain orientations. Even though the grain boundaries are well-stitched, the lateral size and uniformity of the  $\alpha$ -MoO<sub>3</sub> could be improved by reducing the degeneracy of the 2D templates, such as uniaxial strain or in-plane electric field.

Second, a method to control stoichiometry of  $\alpha$ -MoO<sub>3</sub> is required. Even though  $\alpha$ -MoO<sub>3</sub> grown on the 2D templates shows high crystallinity, its band structure can be modulated by controlling oxygen vacancy.

Finally, phase transition of  $\alpha$ -MoO<sub>3</sub> also widens the potential of MoO<sub>3</sub>-based heterostructures. Since MoO<sub>3</sub> possesses various structures and phases with different properties, novel physical phenomena can be achieved by phase transition and formation of multi-phased structures.

Collectively, growth and characterization  $\alpha$ -MoO<sub>3</sub> were investigated, and  $\alpha$ -MoO<sub>3</sub> was used as an in-plane anisotropic building block for moiré superlattice. The results open avenues for further research in the field of in-plane anisotropic 2D materials and symmetry engineering by vdW epitaxy.

# Bibliography

- [1] Novoselov K.S., Geim A.K., Morozov S.V., Jiang D., Zhang Y., Dubonos S.V., Grigorieva I.V. and Firsov A.A. 2004 Electric Field Effect in Atomically Thin Carbon Films *Science* **306** 666
- [2] Novoselov K.S., Mishchenko A., Carvalho A. and Castro Neto A.H. 2016 2D Materials and van der Waals Heterostructures *Science* **353** aac9439
- [3] Scarselli M., Castrucci P. and De Crescenzi M. 2012 Electronic and Optoelectronic Nano-Devices Based on Carbon Nanotubes *J. Phys. Condens. Matter* **24** 313202
- [4] Castro Neto A.H., Guinea F., Peres N.M.R., Novoselov K.S. and Geim A.K. 2009 The Electronic Properties of Graphene *Rev. Mod. Phys.* **81** 109
- [5] Morozov S.V., Novoselov K.S., Katsnelson M.I., Schedin F., Elias D.C., Jaszczak J.A. and Geim A.K. 2008 Giant Intrinsic Carrier Mobilities in Graphene and Its Bilayer *Phys. Rev. Lett.* **100** 016602
- [6] Bolotin K.I., Sikes K.J., Jiang Z., Klima M., Fudenberg G., Hone J., Kim P. and Stormer H.L. 2008 Ultrahigh Electron Mobility in Suspended Graphene *Solid State Commun.* **146** 351
- [7] Allen M.J., Tung V.C. and Kaner R.B. 2010 Honeycomb Carbon: A Review of Graphene *Chem. Rev.* **110** 132
- [8] Molaie M.J., Younas M. and Rezakazemi M. 2021 A Comprehensive Review on Recent Advances in Two-Dimensional (2D) Hexagonal Boron Nitride *ACS Appl. Elec. Mater.* **3** 5165
- [9] Wickramaratne D., Weston L. and van de Walle C.G. 2018 Monolayer to Bulk Properties of Hexagonal Boron Nitride *J. Phys. Chem. C* **122** 25524
- [10] Watanabe K., Taniguchi T. and Kanda H. 2004 Direct-Bandgap Properties and Evidence for Ultraviolet Lasing of Hexagonal Boron Nitride Single Crystal *Nat. Mater.* **3** 404
- [11] Laturia A., van de Put M.L. and Vandenberghe W.G. 2018 Dielectric

- Properties of Hexagonal Boron Nitride and Transition Metal Dichalcogenides: From Monolayer to Bulk *npj 2D Mater. Appl.* **2** 6
- [12] Li L.H., Cervenka J., Watanabe K., Taniguchi T. and Chen Y. 2014 Strong Oxidation Resistance of Atomically Thin Boron Nitride Nanosheets *ACS Nano* **8** 1457
- [13] Splendiani A., Sun L., Zhang Y., Li T., Kim J., Chim C.-Y., Galli G., and Wang F. 2010 Emerging Photoluminescence in Monolayer MoS<sub>2</sub> *Nano Lett.* **10** 1271
- [14] Choi W., Choudhary N., Han G.H., Park J., Akinwande D. and Lee Y.H. 2017 Recent Development of Two-Dimensional Transition Metal Dichalcogenides and Their Applications *Mater. Today* **20** 116
- [15] Das S., Chen H.Y., Penumatcha A.V. and Appenzeller J. 2013 High Performance Multilayer MoS<sub>2</sub> Transistors with Scandium Contacts *Nano Lett.* **13** 100
- [16] Castellanos-Gomez A. 2015 Black Phosphorus: Narrow Gap, Wide Applications *J. Phys. Chem. Lett.* **6** 4280
- [17] Higashitarumizu N., Kawamoto H., Lee C.J., Lin B.H., Chu F.H., Yonemori I., Nishimura T., Wakabayashi K., Chang W.H. and Nagashio K. 2020 Purely In-Plane Ferroelectricity in Monolayer SnS at Room Temperature *Nat. Commun.* **11** 2428
- [18] Bao Y., Song P., Liu Y., Chen Z., Zhu M., Abdelwahab I., Su J., Fu W., Chi X., Yu W., Liu W., Zhao X., Xu Q.H., Yang M. and Loh K.P. 2019 Gate-Tunable In-Plane Ferroelectricity in Few-Layer SnS *Nano Lett.* **19** 5109
- [19] Fei R., Li W., Li J. and Yang L. 2015 Giant Piezoelectricity of Monolayer Group IV Monochalcogenides: SnSe, SnS, GeSe, and GeS *Appl. Phys. Lett.* **107** 173104
- [20] Kwon K.C., Zhang Y., Wang L., Yu W., Wang X., Park I.H., Choi H.S., Ma T., Zhu Z., Tian B., Su C. and Loh K.P. 2020 In-Plane Ferroelectric Tin Monosulfide and Its Application in a Ferroelectric Analog Synaptic Device



- [21] Chang T.R., Xu S.Y., Chang G., Lee C.C., Huang S.M., Wang B., Bian G., Zheng H., Sanchez D.S., Belopolski I., Alidoust N., Neupane M., Bansil A., Jeng H.T., Lin H. and Zahid Hasan M. 2016 Prediction of an Arc-Tunable Weyl Fermion Metallic State in  $\text{Mo}_x\text{W}_{1-x}\text{Te}_2$  *Nat. Commun.* **7** 10639
- [22] He R., Yan J.A., Yin Z., Ye Z., Ye G., Cheng J., Li J. and Lui C.H. 2016 Coupling and Stacking Order of  $\text{ReS}_2$  Atomic Layers Revealed by Ultralow-Frequency Raman Spectroscopy *Nano Lett.* **16** 1404
- [23] Choi Y., Kim K., Lim S.Y., Kim J., Park J.M., Kim J.H., Lee Z. and Cheong H. 2020 Complete Determination of the Crystallographic Orientation of  $\text{ReX}_2$  (X =S, Se) by Polarized Raman Spectroscopy *Nanoscale Horiz.* **5** 308
- [24] Jeong J., Kim H.S., Kwon G., Jeong K., Lee H., Lee J.H., Park M., Lee C., Yu S., Kim H., Im S., Yoo K., Lee E. and Cho M.H. 2022 Ferroelastic-Ferroelectric Multiferroicity in van der Waals Rhenium Dichalcogenides *Adv. Mater.* **34** e2108777
- [25] Park J.M., Lee S., Na W., Kim K. and Cheong H. 2022 Precise Determination of Offset between Optical Axis and Re-Chain Direction in Rhenium Disulfide *ACS Nano* **16** 9222
- [26] Huang L., Zheng F., Deng Q., Thi Q.H., Wong L.W., Cai Y., Wang N., Lee C.S., Lau S.P., Ly T.H. and Zhao J. 2020 Anomalous Fracture in Two-Dimensional Rhenium Disulfide *Sci. Adv.* **6** eabc2282
- [27] Lin Y.C., Komsa H.P., Yeh C.H., Bjorkman T., Liang Z.Y., Ho C.H., Huang Y.S., Chiu P.W., Krashennnikov A.V. and Suenaga K. 2015 Single-Layer  $\text{ReS}_2$ : Two-Dimensional Semiconductor with Tunable In-Plane Anisotropy *ACS Nano* **9** 11249
- [28] Geim A.K. and Novoselov K.S. 2007 The Rise of Graphene *Nat. Mater.* **6** 183
- [29] Lee C.H., Lee G.H., van der Zande A.M., Chen W., Li Y., Han M., Cui X., Arefe G., Nuckolls C., Heinz T.F., Guo J., Hone J. and Kim P. 2014

- Atomically Thin p-n Junctions with van der Waals Heterointerfaces *Nat. Nanotechnol.* **9** 676
- [30] Yang W.-X., Zhou H.-L., Su D., Yang Z.-R., Song Y.-J., Zhang X.-Y. and Zhang T. 2022 Recent Progress in 2D Material van der Waals Heterostructure-Based Luminescence Devices Towards the Infrared Wavelength Range *J. Mater. Chem. C* **10** 7352
- [31] Tartakovskii A. 2019 Excitons in 2D Heterostructures *Nat. Rev. Phys.* **2** 8
- [32] He F., Zhou Y., Ye Z., Cho S.H., Jeong J., Meng X. and Wang Y. 2021 Moiré Patterns in 2D Materials: A Review *ACS Nano* **15** 5944
- [33] McGilly L.J., Kerelsky A., Finney N.R., Shapovalov K., Shih E.M., Ghiotto A., Zeng Y., Moore S.L., Wu W., Bai Y., Watanabe K., Taniguchi T., Stengel M., Zhou L., Hone J., Zhu X., Basov D.N., Dean C., Dreyer C.E. and Pasupathy A.N. 2020 Visualization of Moiré Superlattices *Nat. Nanotechnol.* **15** 580
- [34] Cao Y., Fatemi V., Demir A., Fang S., Tomarken S.L., Luo J.Y., Sanchez-Yamagishi J.D., Watanabe K., Taniguchi T., Kaxiras E., Ashoori R.C. and Jarillo-Herrero P. 2018 Correlated Insulator Behaviour at Half-Filling in Magic-Angle Graphene Superlattices *Nature* **556** 80
- [35] Cao Y., Fatemi V., Fang S., Watanabe K., Taniguchi T., Kaxiras E. and Jarillo-Herrero P. 2018 Unconventional Superconductivity in Magic-Angle Graphene Superlattices *Nature* **556** 43
- [36] Du L., Molas M.R., Huang Z., Zhang G., Wang F. and Sun Z. 2023 Moiré Photonics and Optoelectronics *Science* **379** eadg0014
- [37] Lu X., Stepanov P., Yang W., Xie M., Aamir M.A., Das I., Urgell C., Watanabe K., Taniguchi T., Zhang G., Bachtold A., MacDonald A.H. and Efetov D.K. 2019 Superconductors, Orbital Magnets and Correlated States in Magic-Angle Bilayer Graphene *Nature* **574** 653
- [38] Deng B., Ma C., Wang Q., Yuan S., Watanabe K., Taniguchi T., Zhang F. and Xia F. 2020 Strong Mid-Infrared Photoresponse in Small-Twist-Angle

Bilayer Graphene *Nat. Photon.* **14** 549

- [39] Hunt B., Sanchez-Yamagishi J.D., Young A.F., Yankowitz M., LeRoy B.J., Watanabe K., Taniguchi T., Moon P., Koshino M., Jarillo-Herrero P. and Ashoori R.C. 2013 Massive Dirac Fermions and Hofstadter Butterfly in a van der Waals Heterostructure *Science* **340** 1427
- [40] Yasuda K., Wang X., Watanabe K., Taniguchi T. and Jarillo-Herrero P. 2021 Stacking-Engineered Ferroelectricity in Bilayer Boron Nitride *Science* **372** 1458
- [41] Tang K. and Qi W. 2020 Moiré-Pattern-Tuned Electronic Structures of van der Waals Heterostructures *Adv. Funct. Mater.* **30** 2002672
- [42] Hermann K. 2012 Periodic Overlayers and Moiré Patterns: Theoretical Studies of Geometric Properties *J. Phys. Condens. Matter* **24** 314210
- [43] Kang P., Zhang W.-T., Michaud-Rioux V., Kong X.-H., Hu C., Yu G.-H. and Guo H. 2017 Moiré Impurities in Twisted Bilayer Black Phosphorus: Effects on the Carrier Mobility *Phys. Rev. B* **96** 195406
- [44] Kennes D.M., Xian L., Claassen M. and Rubio A. 2020 One-Dimensional Flat Bands in Twisted Bilayer Germanium Selenide *Nat. Commun.* **11** 1124
- [45] Zhang L., Zhang X. and Lu G. 2021 One-Dimensional Flat Bands and Anisotropic Moiré Excitons in Twisted Tin Sulfide Bilayers *Chem. Mater.* **33** 7432
- [46] Zhong Q. and Pang X. 2023 Exploring the Oxidation Mechanisms of Black Phosphorus: A Review *J. Mater. Sci.* **58** 2068
- [47] Sutter E., Zhang B., Sun M. and Sutter P. 2019 Few-Layer to Multilayer Germanium(II) Sulfide: Synthesis, Structure, Stability, and Optoelectronics *ACS Nano* **13** 9352
- [48] Walsh A. and Watson G.W. 2005 Influence of the Anion on Lone Pair Formation in Sn(II) Monochalcogenides: A Dft Study *J. Phys. Chem. B* **109** 18868
- [49] Lee C.H., Silva E.C., Calderin L., Nguyen M.A., Hollander M.J., Bersch B.,

- Mallouk T.E. and Robinson J.A. 2015 Tungsten Ditelluride: A Layered Semimetal *Sci. Rep.* **5** 10013
- [50] de Castro I.A., Datta R.S., Ou J.Z., Castellanos-Gomez A., Sriram S., Daeneke T. and Kalantar-Zadeh K. 2017 Molybdenum Oxides-from Fundamentals to Functionality *Adv. Mater.* **29** 1701619
- [51] Guo Y. and Robertson J. 2014 Origin of the High Work Function and High Conductivity of MoO<sub>3</sub> *Appl. Phys. Lett.* **105** 222110
- [52] Kihlborg L. 1963 Least Squares Refinement of Crystal Structure of Molybdenum Trioxide *Arkiv for Kemi* **21** 357
- [53] Qu Q., Zhang W.-B., Huang K. and Chen H.-M. 2017 Electronic Structure, Optical Properties and Band Edges of Layered MoO<sub>3</sub>: A First-Principles Investigation *Comput. Mater. Sci.* **130** 242
- [54] Zhang W.B., Qu Q. and Lai K. 2017 High-Mobility Transport Anisotropy in Few-Layer MoO<sub>3</sub> and Its Origin *ACS Appl. Mater. Interfaces* **9** 1702
- [55] Head A.R., Gattinoni C., Trotochaud L., Yu Y., Karslioglu O., Pletincx S., Eichhorn B. and Bluhm H. 2019 Water (Non-)Interaction with MoO<sub>3</sub> *J. Phys. Chem. C* **123** 16836
- [56] Yin X., Han H. and Miyamoto A. 2001 Structure and Adsorption Properties of MoO<sub>3</sub>: Insights from Periodic Density Functional Calculations *J. Mol. Model.* **7** 207
- [57] Yun J., Jang W., Lee T., Lee Y. and Soon A. 2017 Aligning the Band Structures of Polymorphic Molybdenum Oxides and Organic Emitters in Light-Emitting Diodes *Phys. Rev. Appl.* **7** 024025
- [58] Balendhran S., Walia S., Nili H., Ou J.Z., Zhuiykov S., Kaner R.B., Sriram S., Bhaskaran M. and Kalantar-zadeh K. 2013 Two-Dimensional Molybdenum Trioxide and Dichalcogenides *Adv. Funct. Mater.* **23** 3952
- [59] Meyer J., Hamwi S., Kroger M., Kowalsky W., Riedl T. and Kahn A. 2012 Transition Metal Oxides for Organic Electronics: Energetics, Device Physics and Applications *Adv. Mater.* **24** 5408

- [60] Negishi H., Negishi S., Kuroiwa Y., Sato N. and Aoyagi S. 2004 Anisotropic Thermal Expansion of Layered MoO<sub>3</sub> Crystals *Phys. Rev. B* **69** 064111
- [61] Puebla S., D'Agosta R., Sanchez-Santolino G., Frisenda R., Munuera C. and Castellanos-Gomez A. 2021 In-plane Anisotropic Optical and Mechanical Properties of Two-Dimensional MoO<sub>3</sub> *npj 2D Mater. Appl.* **5** 37
- [62] Ma W., Alonso-Gonzalez P., Li S., Nikitin A.Y., Yuan J., Martin-Sanchez J., Taboada-Gutierrez J., Amenabar I., Li P., Velez S., Tollan C., Dai Z., Zhang Y., Sriram S., Kalantar-Zadeh K., Lee S.T., Hillenbrand R. and Bao Q. 2018 In-plane Anisotropic and Ultra-Low-Loss Polaritons in a Natural van der Waals Crystal *Nature* **562** 557
- [63] Novak T.G., Kim J., Tiwari A.P., Kim J., Lee S., Lee J. and Jeon S. 2020 2D MoO<sub>3</sub> Nanosheets Synthesized by Exfoliation and Oxidation of MoS<sub>2</sub> for High Contrast and Fast Response Time Electrochromic Devices *ACS Sustain. Chem. Eng.* **8** 11276
- [64] Kalantar-zadeh K., Tang J., Wang M., Wang K.L., Shailos A., Galatsis K., Kojima R., Strong V., Lech A., Wlodarski W. and Kaner R.B. 2010 Synthesis of Nanometre-Thick MoO<sub>3</sub> Sheets *Nanoscale* **2** 429
- [65] Du Y., Li G., Peterson E.W., Zhou J., Zhang X., Mu R., Dohnalek Z., Bowden M., Lyubinetsky I. and Chambers S.A. 2016 Iso-Oriented Monolayer  $\alpha$ -MoO<sub>3</sub>(010) Films Epitaxially Grown on SrTiO<sub>3</sub>(001) *Nanoscale* **8** 3119
- [66] Kim J.H., Dash J.K., Kwon J., Hyun C., Kim H., Ji E. and Lee G.-H. 2018 van der Waals Epitaxial Growth of Single Crystal  $\alpha$ -MoO<sub>3</sub> Layers on Layered Materials Growth Templates *2D Mater.* **6** 015016
- [67] Molina-Mendoza A.J., Lado J.L., Island J.O., Nino M.A., Aballe L., Foerster M., Bruno F.Y., Lopez-Moreno A., Vaquero-Garzon L., van der Zant H.S.J., Rubio-Bollinger G., Agrait N., Perez E.M., Fernandez-Rossier J. and Castellanos-Gomez A. 2016 Centimeter-Scale Synthesis of Ultrathin Layered MoO<sub>3</sub> by van der Waals Epitaxy *Chem. Mater.* **28** 4042

- [68] Yan B., Zheng Z., Zhang J., Gong H., Shen Z., Huang W. and Yu T. 2009 Orientation Controllable Growth of MoO<sub>3</sub> Nanoflakes: Micro-Raman, Field Emission, and Birefringence Properties *J. Phys. Chem. C* **113** 20259
- [69] Cai L., McClellan C.J., Koh A.L., Li H., Yalon E., Pop E. and Zheng X. 2017 Rapid Flame Synthesis of Atomically Thin MoO<sub>3</sub> Down to Monolayer Thickness for Effective Hole Doping of WSe<sub>2</sub> *Nano Lett.* **17** 3854
- [70] Li X., Cui F., Feng Q., Wang G., Xu X., Wu J., Mao N., Liang X., Zhang Z., Zhang J. and Xu H. 2016 Controlled Growth of Large-Area Anisotropic ReS<sub>2</sub> Atomic Layer and Its Photodetector Application *Nanoscale* **8** 18956
- [71] Dumcenco D., Ovchinnikov D., Marinov K., Lazic P., Gibertini M., Marzari N., Lopez Sanchez O., Kung Y.C., Krasnozhan D., Chen M.W., Bertolazzi S., Gillet P., Fontcuberta i Morral A., Radenovic A. and Kis A. 2015 Large-Area Epitaxial Monolayer MoS<sub>2</sub> *ACS Nano* **9** 4611
- [72] Volta J.-C., Forissier M., Theobald F. and Pham T.P. 1981 Dependence of Selectivity on Surface Structure of MoO<sub>3</sub> Catalysts *Faraday Discuss.* **72** 225
- [73] Sreedhara M.B., Matte H.S., Govindaraj A. and Rao C.N. 2013 Synthesis, Characterization, and Properties of Few-Layer MoO<sub>3</sub> *Chem. Asian J.* **8** 2430
- [74] Song Y.X. and Bhushan B. 2006 Atomic-Scale Topographic and Friction Force Imaging and Cantilever Dynamics in Friction Force Microscopy *Phys. Rev. B* **74** 165401
- [75] Lee C., Li Q., Kalb W., Liu X.Z., Berger H., Carpick R.W. and Hone J. 2010 Frictional Characteristics of Atomically Thin Sheets *Science* **328** 76
- [76] Enachescu M., Schleef D., Ogletree D.F. and Salmeron M. 1999 Integration of Point-Contact Microscopy and Atomic-Force Microscopy: Application to Characterization of Graphite/Pt(111) *Phys. Rev. B* **60** 16913
- [77] Simchi H., McCandless B.E., Meng T., Boyle J.H. and Shafarman W.N. 2013 Characterization of Reactively Sputtered Molybdenum Oxide Films for Solar Cell Application *J. Appl. Phys.* **114** 013503
- [78] Dieterle M., Weinberg G. and Mestl G. 2002 Raman Spectroscopy of

Molybdenum Oxides Part I. Structural Characterization of Oxygen Defects in  $\text{MoO}_{3-x}$  by Dr UV/Vis, Raman Spectroscopy and X-Ray Diffraction *Phys. Chem. Chem. Phys.* **4** 812

- [79] Wang D., Li J.-N., Zhou Y., Xu D.-H., Xiong X., Peng R.-W. and Wang M. 2016 van der Waals Epitaxy of Ultrathin  $\alpha$ - $\text{MoO}_3$  Sheets on Mica Substrate with Single-Unit-Cell Thickness *Appl. Phys. Lett.* **108** 053107
- [80] Kalantar-zadeh K., Ou J.Z., Daeneke T., Mitchell A., Sasaki T. and Fuhrer M.S. 2016 Two Dimensional and Layered Transition Metal Oxides *Appl. Mater. Today* **5** 73
- [81] Deng X., Quek S.Y., Biener M.M., Biener J., Kang D.H., Schalek R., Kaxiras E. and Friend C.M. 2008 Selective Thermal Reduction of Single-Layer  $\text{MoO}_3$  Nanostructures on Au(111) *Surf. Sci.* **602** 1166
- [82] Guimond S., Gobke D., Sturm J.M., Romanyszyn Y., Kühlenbeck H., Cavalleri M. and Freund H.J. 2013 Well-Ordered Molybdenum Oxide Layers on Au(111): Preparation and Properties *J. Phys. Chem. C* **117** 8746
- [83] Brocawik E. 1981 Scf-Sw- $X\alpha$  Calculations of the Removal of Oxygen from Oxide Surfaces by Vacancy Formation and Crystallographic Shear Mechanisms *J. Catal.* **72** 379
- [84] Sian T.S. and Reddy G.B. 2004 Optical, Structural and Photoelectron Spectroscopic Studies on Amorphous and Crystalline Molybdenum Oxide Thin Films *Sol. Energy Mater. Sol. Cells* **82** 375
- [85] Py M.A., Schmid P.E. and Vallin J.T. 2007 Raman Scattering and Structural Properties of  $\text{MoO}_3$  *Il Nuovo Cimento B* **38** 27
- [86] Lee C., Yan H., Brus L.E., Heinz T.F., Hone J. and Ryu S. 2010 Anomalous Lattice Vibrations of Single- and Few-Layer  $\text{MoS}_2$  *ACS Nano* **4** 2695
- [87] Ganduglia-Pirovano M.V., Hofmann A. and Sauer J. 2007 Oxygen Vacancies in Transition Metal and Rare Earth Oxides: Current State of Understanding and Remaining Challenges *Surf. Sci. Rep.* **62** 219
- [88] Inzani K., Grande T., Vullum-Bruer F. and Selbach S.M. 2016 A van der

Waals Density Functional Study of MoO<sub>3</sub> and Its Oxygen Vacancies *J. Phys. Chem. C* **120** 8959

- [89] Greiner M.T., Chai L., Helander M.G., Tang W.M. and Lu Z.H. 2013 Metal/Metal-Oxide Interfaces: How Metal Contacts Affect the Work Function and Band Structure of MoO<sub>3</sub> *Adv. Funct. Mater.* **23** 215
- [90] Greiner M.T., Chai L., Helander M.G., Tang W.M. and Lu Z.H. 2012 Transition Metal Oxide Work Functions: The Influence of Cation Oxidation State and Oxygen Vacancies *Adv. Funct. Mater.* **22** 4557
- [91] Zhao Y., Liu J., Zhou Y., Zhang Z., Xu Y., Naramoto H. and Yamamoto S. 2003 Preparation of MoO<sub>3</sub> Nanostructures and Their Optical Properties *J. Phys. Condens. Matter* **15** L547
- [92] Koike K., Wada R., Yagi S., Harada Y., Sasa S. and Yano M. 2014 Characteristics of MoO<sub>3</sub> Films Grown by Molecular Beam Epitaxy *Jpn. J. Appl. Phys.* **53**
- [93] Xiang D., Han C., Zhang J. and Chen W. 2014 Gap States Assisted MoO<sub>3</sub> Nanobelt Photodetector with Wide Spectrum Response *Sci. Rep.* **4** 4891
- [94] Firment L.E. and Ferretti A. 1983 Stoichiometric and Oxygen Deficient MoO<sub>3</sub> (010) Surfaces *Surf. Sci.* **129** 155
- [95] Irfan I., Turinske A.J., Bao Z.N. and Gao Y.L. 2012 Work Function Recovery of Air Exposed Molybdenum Oxide Thin Films *Appl. Phys. Lett.* **101** 093305
- [96] Irfan, Ding H.J., Gao Y.L., Small C., Kim D.Y., Subbiah J. and So F. 2010 Energy Level Evolution of Air and Oxygen Exposed Molybdenum Trioxide Films *Appl. Phys. Lett.* **96** 243307
- [97] Deb S. and Chopoorian J. 1966 Optical Properties and Color-Center Formation in Thin Films of Molybdenum Trioxide *J. Appl. Phys.* **37** 4818
- [98] Lajaunie L., Boucher F., Dessapt R. and Moreau P. 2013 Strong Anisotropic Influence of Local-Field Effects on the Dielectric Response of  $\alpha$ -MoO<sub>3</sub> *Phys. Rev. B* **88** 115141



- [99] Deb S. 1968 Physical Properties of a Transition Metal Oxide: Optical and Photoelectric Properties of Single Crystal and Thin Film Molybdenum Trioxide *Proc. R. Soc. Lond. A* **304** 211
- [100] Li F. and Chen Z. 2013 Tuning Electronic and Magnetic Properties of MoO<sub>3</sub> Sheets by Cutting, Hydrogenation, and External Strain: A Computational Investigation *Nanoscale* **5** 5321
- [101] Lou S.N., Yap N., Scott J., Amal R. and Ng Y.H. 2014 Influence of MoO<sub>3</sub> (110) Crystalline Plane on Its Self-Charging Photoelectrochemical Properties *Sci. Rep.* **4** 7428
- [102] Cleveland J.P., Manne S., Bocek D. and Hansma P.K. 1993 A Nondestructive Method for Determining the Spring Constant of Cantilevers for Scanning Force Microscopy *Rev. Sci. Instrum.* **64** 403
- [103] Tocha E., Song J., Schonherr H. and Vancso G.J. 2007 Calibration of Friction Force Signals in Atomic Force Microscopy in Liquid Media *Langmuir* **23** 7078
- [104] Cheon J.Y., Kim J.H., Kim J.H., Goddeti K.C., Park J.Y. and Joo S.H. 2014 Intrinsic Relationship between Enhanced Oxygen Reduction Reaction Activity and Nanoscale Work Function of Doped Carbons *J. Am. Chem. Soc.* **136** 8875
- [105] Kim J.H., Hyun C., Kim H., Dash J.K., Ihm K. and Lee G.-H. 2019 Thickness-Insensitive Properties of  $\alpha$ -MoO<sub>3</sub> Nanosheets by Weak Interlayer Coupling *Nano Lett.* **19** 8868
- [106] Mate C.M., McClelland G.M., Erlandsson R. and Chiang S. 1987 *Scanning Tunneling Microscopy*: Springer) pp 226
- [107] Kim J.H., Fu D., Kwon S., Liu K., Wu J. and Park J.Y. 2016 Crossing Thermal Lubricity and Electronic Effects in Friction: Vanadium Dioxide under the Metal–Insulator Transition *Adv. Mater. Interfaces* **3** 1500388
- [108] Riedo E. and Brune H. 2003 Young Modulus Dependence of Nanoscopic Friction Coefficient in Hard Coatings *Appl. Phys. Lett.* **83** 1986

- [109] Mate C.M., McClelland G.M., Erlandsson R. and Chiang S. 1987 Atomic-Scale Friction of a Tungsten Tip on a Graphite Surface *Phys. Rev. Lett.* **59** 1942
- [110] Xu L., Ma T.-B., Hu Y.-Z. and Wang H. 2011 Vanishing Stick–Slip Friction in Few-Layer Graphenes: The Thickness Effect *Nanotechnology* **22** 285708
- [111] Reguzzoni M., Fasolino A., Molinari E. and Righi M.C. 2012 Friction by Shear Deformations in Multilayer Graphene *J. Phys. Chem. C* **116** 21104
- [112] Liang T., Sawyer W.G., Perry S.S., Sinnott S.B. and Phillpot S.R. 2008 First-Principles Determination of Static Potential Energy Surfaces for Atomic Friction in MoS<sub>2</sub> and MoO<sub>3</sub> *Phys. Rev. B* **77** 104105
- [113] Korhonen T. and Koskinen P. 2015 Peeling of Multilayer Graphene Creates Complex Interlayer Sliding Patterns *Phys. Rev. B* **92** 115427
- [114] Wang W., Lee T. and Reed M.A. 2003 Mechanism of Electron Conduction in Self-Assembled Alkanethiol Monolayer Devices *Phys. Rev. B* **68** 035416
- [115] Mandelli D., Leven I., Hod O. and Urbakh M. 2017 Sliding Friction of Graphene/Hexagonal–Boron Nitride Heterojunctions: A Route to Robust Superlubricity *Sci. Rep.* **7** 10851
- [116] Reshak A.H. 2015 Specific Features of Electronic Structures and Optical Susceptibilities of Molybdenum Oxide *RSC Adv.* **5** 22044
- [117] Lee G.-H., Yu Y.-J., Lee C., Dean C., Shepard K.L., Kim P. and Hone J. 2011 Electron Tunneling through Atomically Flat and Ultrathin Hexagonal Boron Nitride *Appl. Phys. Lett.* **99** 243114
- [118] Hattori Y., Taniguchi T., Watanabe K. and Nagashio K. 2015 Layer-by-Layer Dielectric Breakdown of Hexagonal Boron Nitride *ACS Nano* **9** 916
- [119] Kant K.P. and Srivastava R. 1975 Dielectric Permittivity and Breakdown Strength of Molybdenum Trioxide Films *J. Phys. Soc. Japan* **39** 1316
- [120] Sacha G., Verdaguer A., Martinez J., Sáenz J., Ogletree D. and Salmeron M. 2005 Effective Tip Radius in Electrostatic Force Microscopy *Appl. Phys. Lett.* **86** 123101

- [121] Dhanapala H.Y. 2012 Dielectric Constant Measurements Using Atomic Force Microscopy System. Wright State University)
- [122] Fumagalli L., Ferrari G., Sampietro M. and Gomila G. 2007 Dielectric-Constant Measurement of Thin Insulating Films at Low Frequency by Nanoscale Capacitance Microscopy *Appl. Phys. Lett.* **91** 243110
- [123] Yu Y.-J., Zhao Y., Ryu S., Brus L.E., Kim K.S. and Kim P. 2009 Tuning the Graphene Work Function by Electric Field Effect *Nano Lett.* **9** 3430
- [124] Robinson B.J., Giusca C.E., Gonzalez Y.T., Kay N.D., Kazakova O. and Kolosov O.V. 2015 Structural, Optical and Electrostatic Properties of Single and Few-Layers MoS<sub>2</sub>: Effect of Substrate *2D Mater.* **2** 015005
- [125] Koma A. 1992 van der Waals Epitaxy—a New Epitaxial Growth Method for a Highly Lattice-Mismatched System *Thin Solid Films* **216** 72
- [126] Ueno K., Saiki K., Shimada T. and Koma A. 1990 Epitaxial Growth of Transition Metal Dichalcogenides on Cleaved Faces of Mica *J. Vac. Sci. Technol. A* **8** 68
- [127] Lin Z., Yin A., Mao J., Xia Y., Kempf N., He Q., Wang Y., Chen C.-Y., Zhang Y. and Ozolins V. 2016 Scalable Solution-Phase Epitaxial Growth of Symmetry-Mismatched Heterostructures on Two-Dimensional Crystal Soft Template *Sci. Adv.* **2** e1600993
- [128] Tang G., You P., Tai Q., Yang A., Cao J., Zheng F., Zhou Z., Zhao J., Chan P.K.L. and Yan F. 2019 Solution-Phase Epitaxial Growth of Perovskite Films on 2D Material Flakes for High-Performance Solar Cells *Adv. Mater.* **31** 1807689
- [129] Wu Z., Lyu Y., Zhang Y., Ding R., Zheng B., Yang Z., Lau S.P., Chen X.H. and Hao J. 2021 Large-Scale Growth of Few-Layer Two-Dimensional Black Phosphorus *Nat. Mater.* **20** 1
- [130] Liu Y., Rodrigues J., Luo Y.Z., Li L., Carvalho A., Yang M., Laksono E., Lu J., Bao Y. and Xu H. 2018 Tailoring Sample-Wide Pseudo-Magnetic Fields on a Graphene–Black Phosphorus Heterostructure *Nat. Nanotechnol.*

- [131] Akamatsu T., Ideue T., Zhou L., Dong Y., Kitamura S., Yoshii M., Yang D., Onga M., Nakagawa Y. and Watanabe K. 2021 A van der Waals Interface That Creates In-Plane Polarization and a Spontaneous Photovoltaic Effect *Science* **372** 68
- [132] Ahn G.H., Amani M., Rasool H., Lien D.-H., Mastandrea J.P., Ager Iii J.W., Dubey M., Chrzan D.C., Minor A.M. and Javey A. 2017 Strain-Engineered Growth of Two-Dimensional Materials *Nat. Commun.* **8** 1
- [133] Hohenberg P. and Kohn W. 1964 Inhomogeneous Electron Gas *Phys. Rev.* **136** B864
- [134] Kohn W. and Sham L.J. 1965 Self-Consistent Equations Including Exchange and Correlation Effects *Phys. Rev.* **140** A1133
- [135] Kresse G. and Furthmuller J. 1996 Efficient Iterative Schemes for Ab Initio Total-Energy Calculations Using a Plane-Wave Basis Set *Phys. Rev. B* **54** 11169
- [136] Kresse G. and Hafner J. 1993 Ab Initio Molecular Dynamics for Liquid Metals *Phys. Rev. B* **47** 558
- [137] Blochl P.E. 1994 Projector Augmented-Wave Method *Phys. Rev. B* **50** 17953
- [138] Kresse G. and Joubert D. 1999 From Ultrasoft Pseudopotentials to the Projector Augmented-Wave Method *Phys. Rev. B* **59** 1758
- [139] Hamada I. 2014 van der Waals Density Functional Made Accurate *Phys. Rev. B* **89**
- [140] Zheng B., Wang Z., Chen Y., Zhang W. and Li X. 2018 Centimeter-Sized 2D  $\alpha$ -MoO<sub>3</sub> Single Crystal: Growth, Raman Anisotropy, and Optoelectronic Properties *2D Mater.* **5** 045011
- [141] Ferrari A.C. and Basko D.M. 2013 Raman Spectroscopy as a Versatile Tool for Studying the Properties of Graphene *Nat. Nanotechnol.* **8** 235
- [142] Malard L., Pimenta M.A., Dresselhaus G. and Dresselhaus M. 2009 Raman

- [143] Andersson G., Magneli A., Sillén L. and Rottenberg M. 1950 On the Crystal Structure of Molybdenum Trioxide *Acta Chem. Scand.* **4** 793
- [144] Ding H., Ray K.G., Ozolins V. and Asta M. 2012 Structural and Vibrational Properties of  $\alpha$ -MoO<sub>3</sub> from van der Waals Corrected Density Functional Theory Calculations *Phys. Rev. B* **85** 012104
- [145] Kim H., Kim J.H., Kim J., Park J., Park K., Baek J.H., Shin J.C., Lee H., Son J., Ryu S., Son Y.W., Cheong H. and Lee G.H. 2023 In-plane Anisotropy of Graphene by Strong Interlayer Interactions with van der Waals Epitaxially Grown MoO<sub>3</sub> *Sci. Adv.* **9** eadg6696
- [146] Meyer J.C., Geim A.K., Katsnelson M.I., Novoselov K.S., Booth T.J. and Roth S. 2007 The Structure of Suspended Graphene Sheets *Nature* **446** 60
- [147] Yu Q., Jauregui L.A., Wu W., Colby R., Tian J., Su Z., Cao H., Liu Z., Pandey D. and Wei D. 2011 Control and Characterization of Individual Grains and Grain Boundaries in Graphene Grown by Chemical Vapour Deposition *Nat. Mater.* **10** 443
- [148] Lee J.E., Ahn G., Shim J., Lee Y.S. and Ryu S. 2012 Optical Separation of Mechanical Strain from Charge Doping in Graphene *Nat. Commun.* **3** 1024
- [149] Ryu S., Liu L., Berciaud S., Yu Y.-J., Liu H., Kim P., Flynn G.W. and Brus L.E. 2010 Atmospheric Oxygen Binding and Hole Doping in Deformed Graphene on a SiO<sub>2</sub> Substrate *Nano Lett.* **10** 4944
- [150] Son J., Choi M., Hong J. and Yang I.S. 2018 Raman Study on the Effects of Annealing Atmosphere of Patterned Graphene *J. Raman Spectrosc.* **49** 183
- [151] Ji E., Kim M.J., Lee J.-Y., Sung D., Kim N., Park J.-W., Hong S. and Lee G.-H. 2021 Substrate Effect on Doping and Degradation of Graphene *Carbon* **184** 651
- [152] Cauduro A.L., Dos Reis R., Chen G., Schmid A.K., Rubahn H.-G. and Madsen M. 2017 Work Function Mapping of MoO<sub>x</sub> Thin-Films for Application in Electronic Devices *Ultramicroscopy* **183** 99

- [153] Kowalczyk D.A., Rogala M., Szalowski K., Kozłowski W., Lutsyk I., Piskorski M., Krukowski P., Dabrowski P., Belić D. and Cichomski M. 2020 Local Electronic Structure of Stable Monolayers of  $\alpha$ -MoO<sub>3-x</sub> Grown on Graphite Substrate *2D Mater.* **8** 025005
- [154] Hu Y., Liu X., Xu S., Wei W., Zeng G., Yuan H., Gao Q., Guo J., Chao M. and Liang E. 2021 Improving the Thermal Expansion and Capacitance Properties of MoO<sub>3</sub> by Introducing Oxygen Vacancies *J. Phys. Chem. C* **125** 10817
- [155] Yoon D., Son Y.-W. and Cheong H. 2011 Negative Thermal Expansion Coefficient of Graphene Measured by Raman Spectroscopy *Nano Lett.* **11** 3227
- [156] Huang M., Yan H., Chen C., Song D., Heinz T.F. and Hone J. 2009 Phonon Softening and Crystallographic Orientation of Strained Graphene Studied by Raman Spectroscopy *Proc. Natl. Acad. Sci. USA* **106** 7304
- [157] Mohiuddin T., Lombardo A., Nair R., Bonetti A., Savini G., Jalil R., Bonini N., Basko D., Galiotis C. and Marzari N. 2009 Uniaxial Strain in Graphene by Raman Spectroscopy: G Peak Splitting, Grüneisen Parameters, and Sample Orientation *Phys. Rev. B* **79** 205433
- [158] Frank O., Tsoukleri G., Parthenios J., Papagelis K., Riaz I., Jalil R., Novoselov K.S. and Galiotis C. 2010 Compression Behavior of Single-Layer Graphenes *ACS Nano* **4** 3131
- [159] Liu H., Neal A.T., Zhu Z., Luo Z., Xu X., Tománek D. and Ye P.D. 2014 Phosphorene: An Unexplored 2D Semiconductor with a High Hole Mobility *ACS Nano* **8** 4033
- [160] Xia F., Wang H. and Jia Y. 2014 Rediscovering Black Phosphorus as an Anisotropic Layered Material for Optoelectronics and Electronics *Nat. Commun.* **5** 1
- [161] Park C.-H., Yang L., Son Y.-W., Cohen M.L. and Louie S.G. 2008 Anisotropic Behaviours of Massless Dirac Fermions in Graphene under

Periodic Potentials *Nat. Phys.* **4** 213

- [162] Li Y., Dietrich S., Forsythe C., Taniguchi T., Watanabe K., Moon P. and Dean C.R. 2021 Anisotropic Band Flattening in Graphene with One-Dimensional Superlattices *Nat. Nanotechnol.* **16** 525
- [163] Medeiros P.V., Stafström S. and Björk J. 2014 Effects of Extrinsic and Intrinsic Perturbations on the Electronic Structure of Graphene: Retaining an Effective Primitive Cell Band Structure by Band Unfolding *Phys. Rev. B* **89** 041407
- [164] Medeiros P.V., Tsirkin S.S., Stafström S. and Björk J. 2015 Unfolding Spinor Wave Functions and Expectation Values of General Operators: Introducing the Unfolding-Density Operator *Phys. Rev. B* **91** 041116
- [165] Kim S., Ihm J., Choi H.J. and Son Y.-W. 2008 Origin of Anomalous Electronic Structures of Epitaxial Graphene on Silicon Carbide *Phys. Rev. Lett.* **100** 176802
- [166] Madsen G.K., Carrete J. and Verstraete M.J. 2018 BoltzTraP2, a Program for Interpolating Band Structures and Calculating Semi-Classical Transport Coefficients *Comput. Phys. Commun.* **231** 140
- [167] Choi M.S., Nipane A., Kim B.S., Ziffer M.E., Datta I., Borah A., Jung Y., Kim B., Rhodes D. and Jindal A. 2021 High Carrier Mobility in Graphene Doped Using a Monolayer of Tungsten Oxyselenide *Nat. Electron.* **4** 731
- [168] Kwon S.-J., Han T.-H., Ko T.Y., Li N., Kim Y., Kim D.J., Bae S.-H., Yang Y., Hong B.H. and Kim K.S. 2018 Extremely Stable Graphene Electrodes Doped with Macromolecular Acid *Nat. Commun.* **9** 1

## Abstract

면내 이방성 이차원 물질 (in-plane anisotropic two-dimensional materials)로 구성된 모아레 초격자 (moiré superlattice)는 기존 모아레 초격자에서 얻을 수 없는 독특한 물리적 특성을 나타낼 것으로 기대된다. 하지만 면내 이방성 이차원 물질의 불안정성으로 인해, 이들로 구성된 모아레 초격자의 실험적 구현은 크게 제한되어 왔다. 이에 따라 면내 이방성 이차원 물질을 기반으로 한 모아레 초격자를 실현하기 위해 대기중 안정한 초박 및 고품질의 면내 이방성 이차원 물질을 제조가 필수적이다.

본 논문에서는 사방정계 (orthorhombic) 몰리브덴 삼산화물 ( $\alpha$ - $\text{MoO}_3$ )을 대기중 안정한 면내 이방성 구성요소로 활용한다. 이러한 목표를 달성하기 위해, 필자는 연구를 다음과 같이 세 단계로 세분화 및 구체화하였다.

첫 번째 단계에서 다양한 이차원 물질 위에  $\alpha$ - $\text{MoO}_3$  나노시트 (nanosheet)를 에피택시 (epitaxy)로 성장시키는 방법을 개발하였다. 비정질  $\alpha$ - $\text{MoO}_3$ 을 대기중에서 승화시켜, 단층부터 다층의  $\alpha$ - $\text{MoO}_3$  나노시트를 성공적으로 합성하였다. 상당한 격자 불일치에도 불구하고, 결정질  $\alpha$ - $\text{MoO}_3$  나노시트는 결정립계를 보이지 않으며 형성되었다. 또한,  $\alpha$ - $\text{MoO}_3$ 의 밴드갭 (band gap), 일함수, 및 전하 유형과 같은 전기적 특성을 조사하였으며, 본 연구를 통해 이차물질 기반 전자소자의 구성요소로써 초박  $\alpha$ - $\text{MoO}_3$ 의 가능성을 확인하였다.

두 번째 단계에서 흑연 위에 에피택시로 성장시킨  $\alpha$ - $\text{MoO}_3$  나노시트의 전기 및 마찰 특성을 체계적으로 확인하였다. 원자 힘 현미경 (atomic force microscopy)을 사용하여 마찰계수, 접착력, 일함수, 터널 전류 (tunnel current), 및 유전 상수와 같은 다양한 특성을 분석하였다.  $\alpha$ - $\text{MoO}_3$ 의 약한 층간 상호작용 (interlayer interaction)으로 인해 마찰계수, 일함수, 유전 함수 등 대부분 특성이 수 층 내에서 빠르게 포화되는 것을 확인하였다.

마지막으로, 에피택시로 성장한  $\alpha$ - $\text{MoO}_3$ 를 기반으로 한 이중구조를 형성하고, 이의 특성을 분석하였다.  $\alpha$ - $\text{MoO}_3$ 를 단층 그래핀에 에피택시로 성장시 이중 구조를 형성하였으며, 이러한 이중 구조는 결정 방향에 따라



매우 상이한 초격자 주기를 가진다. 앞서 조사한  $\alpha\text{-MoO}_3$ 의 전기적·기계적 특성과 이방성으로 인해,  $\alpha\text{-MoO}_3$ 가 성장한 그래핀에 정공 도핑 (hole doping), 압축 응력 (compressive strain), 면내 이방성이 유발되는 것을 확인하였다. 이 연구를 통해, 에피택시로 성장한 2D 층을 사용하여, 비대칭 초격자 형성하고 면내 등방성 이차원물질에서 이방성을 유발하는 새로운 대칭 공학 방법 (symmetry engineering)을 제시한다.